CHALMERS

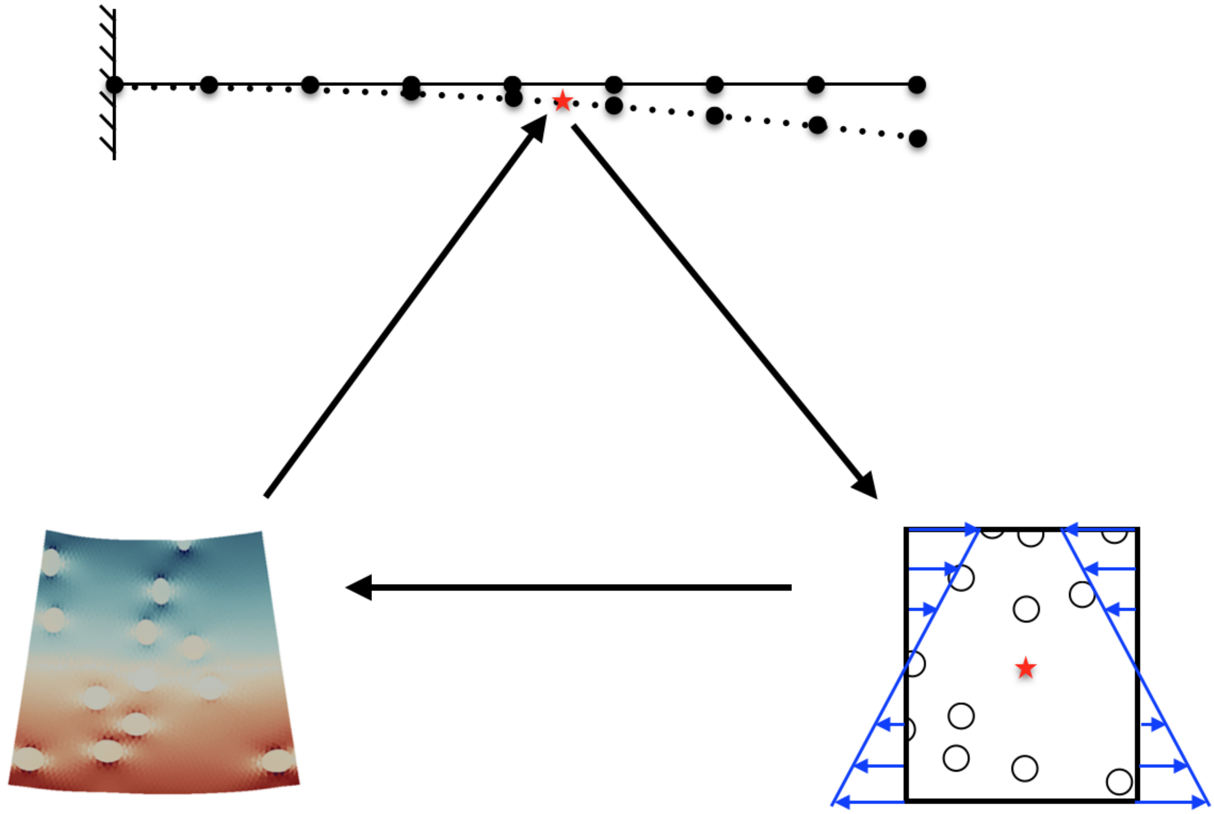

Multiscale Modelling of Heterogeneous Beams

Master's thesis in Applied Mechanics

ROELAND BISSCHOP
CAROLYN ODDY

Department of Applied Mechanics
CHALMERS UNIVERSITY OF TECHNOLOGY
Göteborg, Sweden 2017

MASTER'S THESIS IN APPLIED MECHANICS

Multiscale Modelling of Heterogeneous Beams

ROELAND BISSCHOP
CAROLYN ODDY

Department of Applied Mechanics
Division of Material and Computational Mechanics
CHALMERS UNIVERSITY OF TECHNOLOGY

Göteborg, Sweden 2017

Multiscale Modelling of Heterogeneous Beams
ROELAND BISSCHOP
CAROLYN ODDY

Master's thesis 2017:46
ISSN 1652-8557
Department of Applied Mechanics
Division of Material and Computational Mechanics
Chalmers University of Technology
SE-412 96 Göteborg
Sweden

Cover:
Illustration of the nested finite element procedure used to couple at least two different geometric scales.

Chalmers Reproservice
Göteborg, Sweden 2017

Multiscale Modelling of Heterogeneous Beams
Master's thesis in Applied Mechanics
ROELAND BISSCHOP
CAROLYN ODDY
Department of Applied Mechanics
Division of Material and Computational Mechanics
Chalmers University of Technology

Abstract

Material heterogeneities, such as pores, inclusion or manufacturing defects can have a detrimental impact on the performance of structural components, such as beams, plates and shells. These heterogeneities are typically defined on a much finer scale than that of the structural component, meaning that fully resolving the substructure in numerical analyses is computationally expensive. A method known as FE^2 is therefore considered. As the name suggests, it links at least two finite element (FE) analyses, one defining the macroscale, the other the subscale, in a nested solution procedure. Of particular interest however, are the prolongation (macro-subscale) and homogenisation (subscale-macroscale) techniques used to link a macroscale beam to a statistical volume element (SVE), used to characterise the subscale.

Multiple prolongation and homogenisation methods are presented. Although capturing an accurate elongation and bending response is straightforward, the same cannot be said for the shear response. The standard use of Dirichlet, Neumann, and periodic boundary conditions is insufficient. As the length of a statistical volume element (SVE) increases, there is a deterioration in geometric behaviour. More specifically, the SVE begins to bend in an unphysically manner, leading to overly soft results.

Variationally Consistent Homogenisation (VCH), provides a systematic way to formulate the macroscale and subscale problem, as well as the link between them. Through the introduction of VCH, an additional volumetric constraints, which imposes an internal rotation, is formulated. The additional constraint provides a drastic improvement. The degradation in shear behaviour is no longer apparent and an accurate shear response is captured. It is important to note however, that this is not an ideal solution, as adding the volumetric constraint perturbs the physicality of the subscale problem.

Keywords: Beams, heterogeneities, homogenisation, prolongation

Preface

This thesis, has been completed as part of the Applied Mechanics masters programme at Chalmers University of Technology, under the supervision of Martin Fagerström, Fredrik Larsson, Erik Svenning and Johannes Främby. It has been carried out at the division of Material and Computational Mechanics during the spring semester of 2017, which was a part of the department of Applied Mechanics during the majority of the work.

Acknowledgements

Many thanks to our extremely supportive supervisors, Martin Fagerström, Fredrik Larsson, Erik Svenning and Johannes Främby. In particular, we would like to acknowledge Erik Svenning, who was invaluable in assisting us with OOFEM and helping us understand the finer details of periodic boundary conditions and variationally consistent homogenisation (VCH).

Contents

1 Introduction

Material heterogeneities such as pores, cracks and manufacturing defects, can have a crucial influence on a component's performance. However, efficiently incorporating the presence of heterogeneities in the analysis of structural components such as beams, plates and shells is not always straightforward. The material variations are typically defined on a much finer scale than that of the structural component, meaning that fully resolving the substructure in numerical analyses is computationally expensive.

Approximating the behaviour of beams, plates and shells using the finite element (FE) method, allows for the introduction of multiple assumptions and simplifications that reduce the complexity of the problem formulation. For example, a beam that physically occupies a three-dimensional space with varying and complex cross sections can be modeled using one-dimensional elements. This drastically decreases computational cost. However, it does not directly allow for detailed consideration of material heterogeneities and their structural influence. Determining a procedure that allows the macroscale beam to be considered as a homogeneous structure with effective properties defined through a homogenisation process is therefore preferable, as it allows the computational efficiency of the one-dimensional FE problem to be exploited. Although many different homogenisation techniques exist, perhaps one of the most commonly adopted methods is known as FE^2 [1].

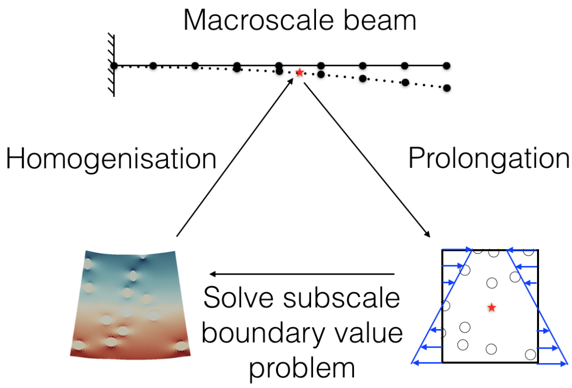

Figure 1.1: Nested finite element procedure.

The FE^2 method, briefly illustrated in Figure 1.1, involves implementing a nested solution procedure used to couple at least two different geometric scales. In this case, a macroscopic beam problem is coupled to a subscale problem, defined by a representative volume element (RVE), that is able to characterise the material heterogeneities in greater detail. The FE^2 method involves formulating an approach with which the macroscale deformation behaviour can be expressed on an RVE using a set of boundary conditions. This is known as prolongation. A standard boundary value problem is then solved on the subscale, the results of which are homogenised in order to determine effective material properties that are re-incorporated into the macroscale problem.

Several authors have previously contributed to this field, presenting a number of prolongation and homogenisation techniques, e.g. those in [2], [3], [4] and [5], that are capable of linking structural elements to subscale RVEs. However, within the available literature, there is a noticeable lack of consideration and discussion given to accurately capturing the shear response of an RVE. As discussed by Främby et al. [6], the standard use of Dirichlet, Neumann and Periodic boundary conditions is not sufficient. For increasingly long RVEs, there is a severe degradation in geometric behaviour. More specifically the RVE begins to bend in an unphysical manner as its length increases, leading to overly soft results. This is illustrated in Figure 1.2. For that reason, an increased emphasis must be given to establishing a prolongation and homogenisation method, that is able to accurately capture the subscale out-of-plane shear behaviour.

In the following work, the considered macroscale structural element is restricted to a beam. Two introductory prolongation and homogenisation methods are considered, in both cases the macro-to-subscale transition primarily takes place using Dirichlet boundary conditions formulated through elementary beam theory. This not only acts as a general introduction to the necessary fundamental concepts, but also illustrates the inherent difficulties in capturing the shear response. A computational homogenisation method formulated for structured

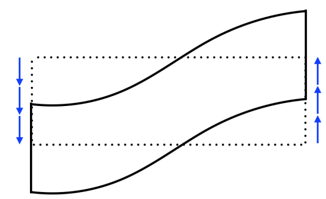

Figure 1.2: A prescribed macroscale shear deformation results in local bending for sufficiently long RVEs.

thin sheets by Geers et al.[7], is also adopted. The publication by Geers et al. gives some consideration to handling the shear response and in their preliminary analyses is able to accurately capture the bending behaviour of a beam. All three of the aforementioned methods however, are unable to accurately capture shear behaviour and require predefined kinematic assumptions on the macroscale problem. In order to circumvent this, Variationally Consistent Homogenisation (VCH) [8], is introduced. VCH is used to formulate two additional prolongation and homogenisation techniques, in which an added volumetric constraint with a prescribed internal rotation is considered. The addition of the volumetric constraints proves positive in initial results, and allows the shear response to be accurately captured.

2 Introductory Beam Theory

As previously stated, the macroscale problem is defined using beam kinematics. In principle beams occupy three dimensional space. However as a beam is dominated by it's axial behaviour, it becomes possible to introduce simplifications and assumptions on the deformation field that significantly reduce the complexity of the problem. Two standard sets of assumptions, that differ in the way in which the internal rotation is prescribed, give what is usually referred to as Euler-Bernoulli and Timoshenko beam theory. Both are briefly summarised in Section 2.2 and 2.4 respectively. One should however be aware that introducing these assumptions can lead to the violation of field equations. Note that from this point forward, all measures associated to the macroscale beam model, i.e. those that are strictly a function of beam length, are denoted using an overline, $\bar{\bullet}$.

2.1 Equilibrium Equations

The equilibrium equations for a beam are determined by considering the cut section, with length Δx, illustrated in Figure 2.1, where internal body forces are neglected. The axial force, shear force, bending moment and distributed load are denoted by $\bar{N}$, $\bar{V}$, $\bar{M}$ and $\bar{q}$ respectively.

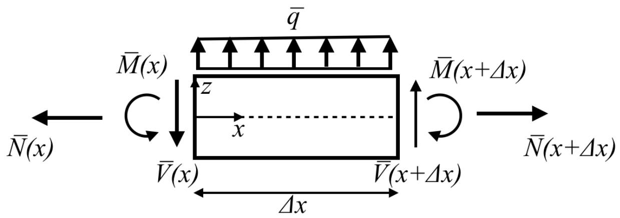

Figure 2.1: Force and moment equilibrium for a beam section

When considering the horizontal force equilibrium, it is found that

$$\bar{N}(x + \Delta x) - \bar{N}(x) = 0.$$

Dividing by Δx and letting $\Delta x \to 0$ gives

$$\lim_{\Delta x \to 0} \frac{\bar{N}(x + \Delta x) - \bar{N}(x)}{\Delta x} = 0.$$

This is the definition of a derivative, and therefore,

$$\frac{\partial \bar{N}(x)}{\partial x} = 0. \tag{2.1}$$

Similarly, from the vertical force equilibrium, it is found that

$$\bar{V}(x + \Delta x) - \bar{V}(x) + \bar{q}(x)\Delta x = 0,$$

which, by again dividing by Δx and letting $\Delta x \to 0$, gives

$$\frac{\partial \bar{V}(x)}{\partial x} = -\bar{q}(x). \tag{2.2}$$

The final equilibrium equation is found by considering the moment equilibrium. In this case, when taken at the centre point

$$-\bar{M}(x + \Delta x) + \bar{M}(x) + \bar{V}(x + \Delta x)\frac{\Delta x}{2} + \bar{V}(x)\frac{\Delta x}{2} = 0,$$

from which

$$\frac{\partial \bar{M}(x)}{\partial x} = \bar{V}(x) \tag{2.3}$$

is obtained.

2.2 Euler-Bernoulli Beam Kinematics

Euler-Bernoulli beam theory is formulated based on the assumption that any vertical straight lines running perpendicular to the beam direction, remain straight and perpendicular to the mid-section after deformation. This is illustrated in Figure 2.2. With the assumption of small strains and that any stretching of the normal in the vertical direction is negligible, the deformation vector is formulated as

$$\boldsymbol{u} = \begin{bmatrix} u & v & w \end{bmatrix} = \begin{bmatrix} \bar{u}_0(x) - z\bar{\phi}(x) & 0 & \bar{w}(x) \end{bmatrix}.$$

where

$$\bar{\phi}(x) = \frac{\partial \bar{w}(x)}{\partial x}.$$

As such, the only non-zero strain component is

$$\begin{aligned}
\varepsilon_{xx}(x, z) &= \frac{\partial \bar{u}(x, z)}{\partial x} \\
&= \frac{\partial \bar{u}_0(x)}{\partial x} - z\frac{\partial \bar{\phi}(x)}{\partial x} \\
&= \bar{\varepsilon}^0(x) - z\bar{\kappa}(\bar{x}),
\end{aligned}$$

where the mean elongation strain and curvature have been introduced as

$$\bar{\epsilon}^0 = \frac{\partial \bar{u}_0(\bar{x})}{\partial x} \text{ and } \bar{\kappa} = \frac{\partial \bar{\phi}(\bar{x})}{\partial x},$$

respectively.

Assuming a linear elastic material behaviour, uniaxial stress, and a constant cross-sectional area, $A = h \cdot t$, the the bending moment $\bar{M}(x)$ is expressed as

$$\begin{aligned}
\bar{M}(x) &= \int_A \sigma_{xx}(x, z) z \, \mathrm{d}A \\
&= \int_{-t/2}^{t/2} \int_{-h/2}^{h/2} E\varepsilon_{xx}(x, z) z \, \mathrm{d}z\mathrm{d}x \\
&= \int_{-t/2}^{t/2} \int_{-h/2}^{h/2} E(x, z)\bar{\varepsilon}^0(x) z \, \mathrm{d}z\mathrm{d}x - \int_{-t/2}^{t/2} \int_{-h/2}^{h/2} E(x, z)\bar{\kappa}(x) z^2 \, \mathrm{d}z\mathrm{d}x \\
&= \overline{ES}\bar{\varepsilon}^0(x) - \overline{EI}\bar{\kappa}(x),
\end{aligned}$$

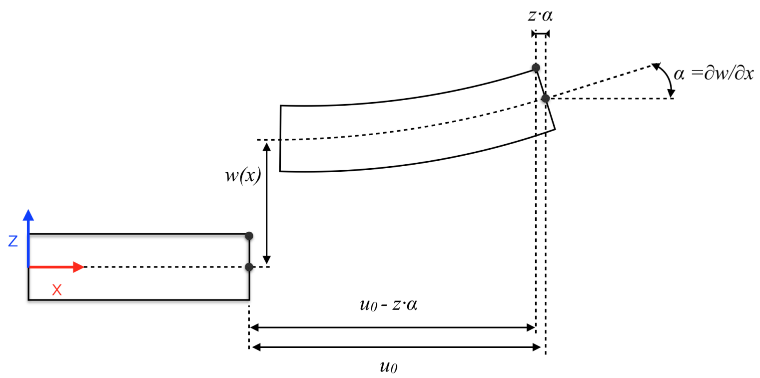

Figure 2.2: Deformation of an Euler-Bernoulli beam in the xz-plane.

where the effective elongation and bending stiffness are defined as

$$\overline{ES} = \int_{-t/2}^{t/2}\int_{-h/2}^{h/2} E(x,z)z \, \mathrm{d}z\mathrm{d}x \text{ and } \overline{EI} = \int_{-t/2}^{t/2}\int_{-h/2}^{h/2} E(x,z)z^2 \, \mathrm{d}z\mathrm{d}x$$

respectively. With the assumption of a constant Young's modulus $E(x,z)$, and the appropriate choice of the coordinate system placement, $\overline{ES} = 0$. Therefore

$$\bar{M}(x) = -\overline{EI}\bar{\kappa}(x). \tag{2.4}$$

The term relating $\bar{M}$ and $\bar{\kappa}$, i.e $\overline{EI}$ is what is referred to as the macroscale effective bending stiffness. Similarly, the relationship between the normal force $\bar{N}$ and the midplane strain $\bar{\varepsilon}^0$ is given by

$$\bar{N}(x) = \int_{-t/2}^{t/2}\int_{-h/2}^{-h/2} \sigma_{xx}(x,z)\mathrm{d}z \tag{2.5}$$

$$= \overline{EA}\bar{\varepsilon}^0(x) - \overline{ES}\bar{\kappa}(x) \tag{2.6}$$

$$= \overline{EA}\bar{\varepsilon}^0(x). \tag{2.7}$$

The macroscale effective stiffness under axial elongation is therefore given by

$$\overline{EA} = \int_{-t/2}^{t/2}\int_{-h/2}^{h/2} E(x,z) \, \mathrm{d}z\mathrm{d}x.$$

.

2.3 Analytical Results Using Euler-Bernoulli Beam Theory

In order to validate the accuracy of future results, three standard load cases applied to a cantilever beam are analysed. In all examples, the beam is assumed to have a thickness of 1 mm. As such it is possible to determine an analytical solution that describes either the axial or vertical deformation of the beam as a function of the macroscale effective bending or axial stiffness.

2.3.1 First Load Case

The first considered load case, illustrated in Figure 2.3, involves the application of an axial load at the beam tip. By combining Equations (2.1) and (2.7)

$$\frac{\partial}{\partial x}\left(\overline{EA}\frac{\partial \bar{u}(x)}{\partial x}\right) = 0$$

is obtained. By integrating twice, and taking into account that for the chosen case $\bar{u}^0(x=0) = 0$ and $N_x(x=50) = 10$ kN, it is found that

$$\bar{u}(x) = \frac{1}{\overline{EA}}\left(C_1 x + C_2\right), \tag{2.8}$$

where $C_1 = N(x = 50) = 10$ kN and $C_2 = 0$.

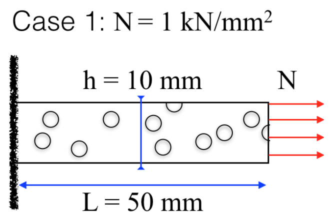

Figure 2.3: First load case

2.3.2 Second Load Case

The second considered load case is shown in Figure 2.4. Here, a distributed shear force is applied at the beam extremity.

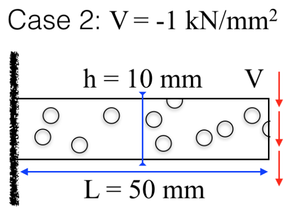

Figure 2.4: Second Load Case

Combining Equations (2.2), (2.3) and (2.4) gives

$$\frac{\partial^2}{\partial x^2}\left(\overline{EI}\frac{\partial^2 \bar{w}(x)}{\partial x^2}\right) = 0.$$

Integrating four times, results in

$$\bar{w}(x) = \frac{1}{\overline{EI}}\left(\frac{C_1 x^3}{6} + \frac{C_2 x^2}{2} + C_3 x + C_4\right), \tag{2.9}$$

where $C_1 = -V(x = 50) = 10$ kN, $C_2 = V(x = 50) \cdot L = -500$ kNmm, $C_3 = 0$ and $C_4 = 0$ since

$$\begin{aligned} \bar{V}(x = 50) &= -10 \text{ kN} \\ \bar{w}(x = 0) &= 0 \\ \bar{M}(x = 50) &= 0 \\ \frac{\partial \bar{w}(x = 0)}{\partial x} &= 0. \end{aligned}$$

2.3.3 Third Load Case

The third case, where a distributed load is applied across the beam, is illustrated in Figure 2.5. It gives an analytic solution of

$$\bar{w}(x) = \frac{1}{\overline{EI}}\left(\frac{q_0 x^4}{24} + \frac{C_1 x^3}{6} + \frac{C_2 x^2}{2} + C_3 x + C_4\right), \tag{2.10}$$

where the considered distributed load $q(x) = q_0 = -200$ N/mm.

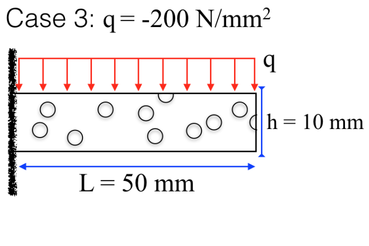

Figure 2.5: Third load case

With consideration to the boundary conditions

$$
\begin{aligned}
\bar{V}(x=50) &= 0, \\
\bar{w}(x=0) &= 0, \\
\frac{\partial \bar{w}(x=0)}{\partial x} &= 0,
\end{aligned}
$$

and

$$\bar{M}(x=50) = 0,$$

it is found that $C_1 = -q_0 \cdot L = 10$ kN, $C_2 = q_0 \cdot L^2/2 = -250$ kNmm, $C_3 = 0$ and $C_4 = 0$.

2.4 Timoshenko Beam Kinematics

The one substantial drawback to Euler-Bernoulli beam theory is that it does not account for any possible out-of-plane shear behaviour of the beam as $\gamma_{xz} = 0$ is enforced. This means, that for relatively stocky beams, Euler-Bernoulli beam theory is not sufficient as it gives an overly stiff response. Timoshenko beam theory however, relaxes the requirement that lines perpendicular to the mid-surface must remain perpendicular after deformation, as illustrated in Figure 2.6.

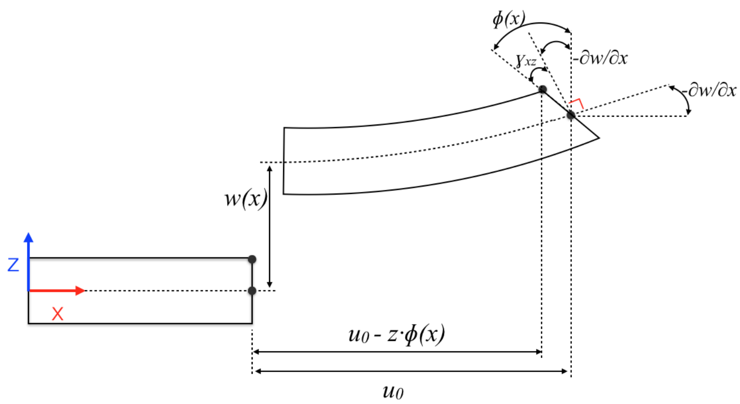

Figure 2.6: Deformation of a Timoshenko beam in the xz-plane.

The displacement vector is then formulated as

$$
\begin{aligned}
\boldsymbol{u} &= \begin{bmatrix} u & v & w \end{bmatrix} \\
&= \begin{bmatrix} \bar{u}^0(x) - z\bar{\phi}(x) & 0 & \bar{w}(x) \end{bmatrix},
\end{aligned}
$$

a where the axial and out of plane strains are given by

$$\begin{aligned}\varepsilon_{xx} &= \frac{\partial \bar{u}^0}{\partial x} - z\frac{\partial \bar{\phi}(x)}{\partial x} \\ &= \bar{\varepsilon}^0 - z\bar{\phi}'(x) \\ &= \bar{\varepsilon}^0 - z\bar{\kappa}(x)\end{aligned}$$

and

$$\begin{aligned}\gamma_{xz} &= \frac{\partial \bar{u}}{\partial z} + \frac{\partial \bar{w}}{\partial x} \\ &= -\bar{\phi}(x) + \frac{\partial \bar{w}(x)}{\partial x}\end{aligned}$$

respectively. Note, that in Timoshenko beam theory, the internal rotation $\bar{\phi}$, is treated as an additional degree of freedom.

Again, assuming a linear elastic material behaviour and a constant cross sectional area $A = t \cdot h$, the relationship between the bending moment and curvature, as well as the normal force and axial strain, are expressed as

$$\bar{M}(x) = \int_{-t/2}^{t/2} \int_{-h/2}^{h/2} \sigma_{xx}(x,z)z \, \mathrm{d}z \tag{2.11}$$

$$= \overline{ES}\bar{\varepsilon}^0 - \overline{EI}\bar{\kappa}(x), \tag{2.12}$$

and

$$\bar{N}(x) = \int_{-t/2}^{t/2} \int_{-h/2}^{h/2} \sigma_{xx}(x,z) \, \mathrm{d}z \tag{2.13}$$

$$= \overline{EA}\bar{\varepsilon}^0(x) + \overline{ES}\bar{\kappa}(x) \tag{2.14}$$

respectively. With the assumption of a constant Young's modulus, and the appropriate positioning of the coordinate system, this may again be reduced to

$$\begin{aligned}\bar{M}(x) &= -\overline{EI}\bar{\kappa}(x) \\ \bar{N}(x) &= \overline{EA}\bar{\varepsilon}^0(x).\end{aligned}$$

As previously eluded to, Timoshenko beam theory allows for the formulation of a relationship between shear force and shear strain. Namely,

$$\bar{V}(x) = \int_{-t/2}^{t/2} \int_{-h/2}^{h/2} \tau_{xz}(x,z) \mathrm{d}z \tag{2.15}$$

$$= \int_{-t/2}^{t/2} \int_{-h/2}^{h/2} G(x,z)\gamma_{xz}(x,z) \mathrm{d}z \tag{2.16}$$

$$= \bar{K}_s\overline{GA}\left(-\bar{\phi}(x) + \frac{\partial \bar{w}(x)}{\partial x}\right) \tag{2.17}$$

$$= \overline{K_s GA}\bar{\gamma}, \tag{2.18}$$

where, it is again assumed that the shear stiffness $G(x,z)$ is constant over the domain. The shear correction factor, denoted $\bar{K}_s$ and the shear stiffness, $\overline{K_s GA}$ are also defined. The shear correction factor is introduced in order to account for the fact that the shear stress and shear strain are not uniformly distributed over the cross-section. Efforts have been made by many authors, e.g Stephen [9] and Cowper [10], to find precise representations for the shear correction factor, which is dependant on the shape of the cross-section as well as Poisson's ratio. The shear correction factor typically given for rectangular sections $\bar{K}_s = 5/6$, is considered in the current work.

2.5 Analytical Results using Timoshenko Beam Theory

Again, for the possibility to validate future results, Timoshenko beam theory is used to determine the analytical solutions of the displacement fields for the three load cases presented in Section 2.3.

2.5.1 First Load Case

The first load case, in which an axial load is applied, gives the same analitical solution as previously, namely

$$\bar{u}(x) = \frac{1}{\overline{EA}}\left(C_1 x + C_2\right), \tag{2.19}$$

where $C_1 = 10$ kN and $C_2 = 0$. The axial deformation of the beam is still purely a function of the axial stiffness.

2.5.2 Second Load Case

Using Timoshenko beam theory, it is now possible to express the analitical solution for the vertical deformation as a function of the bending and shear stiffness. Combining Equations (2.2), (2.3), (2.12) and (2.17) gives

$$\overline{K_s GA}\left(\phi(x) - \frac{\partial \bar{w}(x)}{\partial x}\right) - \frac{1}{\overline{EI}}\frac{\partial^2 \bar{\phi}(x)}{\partial x^2} = 0$$

and

$$\overline{K_s GA}\left(-\frac{\partial \bar{\phi}(x)}{\partial x} + \frac{\partial^2 \bar{w}(x)}{\partial x^2}\right) + \bar{q}(x) = 0.$$

Taking into account the boundary conditions:

$$\begin{aligned} \bar{V}(x=50) &= -10\text{kN} \\ \bar{M}(x=50) &= 0 \\ \bar{w}(x=0) &= 0 \\ \bar{\phi}(x=0) &= 0 \end{aligned}$$

it is found that

$$\bar{w}(x) = -\frac{C_1 x}{\overline{K_s GA}} + \frac{1}{\overline{EI}}\left(\frac{C_1 x^3}{6} + \frac{C_2 x^2}{2} + C_3 x + C_4\right). \tag{2.20}$$

In this case, the integration constants are $C_1 = 10$ kN, $C_2 = -500$ kNmm, $C_3 = 0$ and $C_4 = 0$.

2.5.3 Third Load Case

By again combining Equations (2.2), (2.3), (2.12) and (2.17) with consideration to the boundary conditions given by

$$\begin{aligned} \bar{V}(x=50) &= 0 \\ \bar{M}(x=50) &= 0 \\ \bar{w}(x=0) &= 0 \\ \bar{\phi}(x=0) &= 0, \end{aligned}$$

the analitical expression for the displacement field of the third load case is expressed as

$$\bar{w}(x) = -\frac{1}{\overline{K_s GA}}\left(\frac{q_0 x^2}{2} + C_1 x\right) + \frac{1}{\overline{EI}}\left(\frac{q_0 x^4}{24} + \frac{C_1 x^3}{6} + \frac{C_2 x^2}{2} + C_3 x + C_4\right), \tag{2.21}$$

where $C_1 = 10$ kN, $C_2 = -250$ kNmm, $C_3 = 0$ and $C_4 = 0$.

3 Macroscale Finite Element Problem Formulation

As previously eluded to, the FE macroscale beam problem may be implemented using one-dimensional structural beam elements resulting in low computational costs. Although beams with complex and varying cross-sections may still be considered, it is important to note that formulating the macroscale beam problem in this way, does not directly allow for the detailed inclusion of material heterogeneities and their influence. Instead it is necessary to use some effective/ homogenised value for the axial, bending and shear stiffness, i.e. for $\overline{EA}$, $\overline{EI}$ and $\overline{K_sGA}$. The following acts as a brief overview, and only serves to illustrate the way in which the effective stiffness is incorporated into the considered problem. Further details can be found in [11] and [12].

3.1 Finite Element Problem Formulation of an Euler-Bernoulli Beam

3.1.1 Strong Form

For some arbitrary beam, defined from $x = 0$ to $x = L$, the strong form is given by

$$\frac{\partial \bar{N}(x)}{\partial x} = 0 \text{ in } 0 \leq x \leq L \tag{3.1}$$

$$\frac{\partial^2 \bar{M}(x)}{\partial x^2} = -q(x) \text{ in } 0 \leq x \leq L, \tag{3.2}$$

where the Dirichlet boundary conditions are determined by prescribing given values of $\bar{u}$ and $\bar{w}$ such that

$$\bar{u} = \bar{u}_p \text{ on } x = 0 \text{ and/or } x = L$$
$$\bar{w} = \bar{w}_p \text{ on } x = 0 \text{ and/or } x = L.$$

Similarly the possible Neumann boundary conditions are given by

$$\bar{V} = \bar{V}_p \text{ on } x = 0 \text{ and/or } x = L$$
$$\bar{M} = \bar{M}_p \text{ at } x = 0 \text{ and/or } x = L$$

and

$$\bar{N} = \bar{N}_p \text{ at } x = 0 \text{ and/or } x = L.$$

3.1.2 Weak Form

The weak formulation is determined by first multiplying Equations (3.1) and (3.2) by arbitrary test functions $\delta\bar{u}$ and $\delta\bar{w}$, then integrating over the domain $0 \leq x \leq L$. The final weak form is stated as finding $(\bar{u}, \bar{w}) \in \mathbb{U}$ such that

$$\int_0^L \frac{\partial \delta\bar{u}}{\partial x}\left(\overline{EA}\frac{\partial \bar{u}}{\partial x}\right) \mathrm{d}x = \left[\delta\bar{u} \cdot \bar{N}_p\right]_0^L \tag{3.3}$$

$$\int_0^L \frac{\partial^2 \delta\bar{w}}{\partial x^2}\left(\overline{EI}\frac{\partial^2 \bar{w}}{\partial x^2}\right) \mathrm{d}x = \int_0^L \delta\bar{w} \cdot \bar{q}(x)\mathrm{d}x - \left[\delta\bar{w}\bar{V}_p\right]_0^L + \left[\frac{\partial \delta\bar{w}}{\partial x}\bar{M}_p\right]_0^L \tag{3.4}$$

where Equations (3.3) and (3.4) hold for all $(\delta\bar{u}, \delta\bar{w}) \in \mathbb{U}^0$ and the spaces are defined as follows:

$$\mathbb{U} = \{\bar{u}, \bar{w} : \text{sufficiently regular}, \bar{u} = \bar{u}_p \text{ on } x = 0 \text{ and/ or } x = L, \bar{w} = \bar{w}_p \text{ on } x = 0 \text{ and/or } x = L\}$$
$$\mathbb{U}^0 = \{\delta\bar{u}, \delta\bar{w} : \text{sufficiently regular}, \delta\bar{u} = 0 \text{ where } \bar{u} = \bar{u}_p, \delta\bar{w} = 0 \text{ where } \bar{w} = \bar{w}_p\}.$$

It is important to note that the solution space and test space for the vertical deformation must be twice differentiable, or in other words C^1-continuous.

3.1.3 FE Form

The displacement may approximated as

$$\bar{u} \approx \bar{u}_h = \bar{\underline{\boldsymbol{N}}}_{\bar{u}} \bar{\underline{\boldsymbol{a}}}_{\bar{u}},$$

and

$$\bar{w} \approx \bar{w}_h = \bar{\underline{\boldsymbol{N}}}_{\bar{w}} \bar{\underline{\boldsymbol{a}}}_{\bar{w}},$$

where the nodal displacement and shape function vectors are given by

$$\begin{aligned}
\bar{\underline{\boldsymbol{a}}}_{\bar{u}} &= \begin{bmatrix} \bar{u}_1 & \bar{u}_2 & \dots & \bar{u}_{n,nodes} \end{bmatrix}^T \\
\bar{\underline{\boldsymbol{N}}}_{\bar{u}} &= \begin{bmatrix} \bar{N}_{u,1} & \bar{N}_{u,2} & \dots & \bar{N}_{u,nnodes} \end{bmatrix} \\
\bar{\underline{\boldsymbol{a}}}_{\bar{w}} &= \begin{bmatrix} \bar{w}_1 & \bar{w}_2 & \dots & \bar{w}_{n,nodes} \end{bmatrix}^T
\end{aligned}$$

and

$$\bar{\underline{\boldsymbol{N}}}_{\bar{w}} = \begin{bmatrix} \bar{N}_{w,1} & \bar{N}_{w,2} & \dots & \bar{N}_{u,nnodes} \end{bmatrix}.$$

Note that the underline denotes the use of matrix notation. This in turn gives

$$\begin{aligned}
\frac{\partial u}{\partial x} &= \frac{\partial}{\partial x}\left(\bar{\underline{\boldsymbol{N}}}_{\bar{u}} \bar{\underline{\boldsymbol{a}}}_{\bar{u}}\right) = \bar{\underline{\boldsymbol{B}}}_{\bar{u}} \bar{\underline{\boldsymbol{a}}}_{\bar{u}} \\
\frac{\partial w}{\partial x} &= \frac{\partial}{\partial x}\left(\bar{\underline{\boldsymbol{N}}}_{\bar{w}} \bar{\underline{\boldsymbol{a}}}_{\bar{w}}\right) = \bar{\underline{\boldsymbol{B}}}_{\bar{w}} \bar{\underline{\boldsymbol{a}}}_{\bar{w}},
\end{aligned}$$

and

$$\frac{\partial^2 w}{\partial x^2} = \frac{\partial}{\partial x}\left(\bar{\underline{\boldsymbol{B}}}_{\bar{w}} \bar{\underline{\boldsymbol{a}}}_{\bar{w}}\right) = \bar{\underline{\boldsymbol{C}}}_{\bar{w}} \bar{\underline{\boldsymbol{a}}}_{\bar{w}}.$$

It is important to again note, that the choice of shape functions with which the vertical deformation is approximated must also be C^1-continuous.

Introducing the approximations into Equations (3.3) and (3.4) yields the following system of equations:

$$\begin{bmatrix} \bar{\underline{\boldsymbol{K}}}_{\bar{u}} & \underline{\boldsymbol{0}} \\ \underline{\boldsymbol{0}} & \bar{\underline{\boldsymbol{K}}}_{\bar{w}} \end{bmatrix} \begin{bmatrix} \bar{\underline{\boldsymbol{a}}}_{\bar{u}} \\ \bar{\underline{\boldsymbol{a}}}_{\bar{w}} \end{bmatrix} = \begin{bmatrix} \bar{\underline{\boldsymbol{f}}}_{\bar{u}} \\ \bar{\underline{\boldsymbol{f}}}_{\bar{w}} \end{bmatrix}, \tag{3.5}$$

where

$$\bar{\underline{\boldsymbol{K}}}_{\bar{u}} = \int_0^L \bar{\underline{\boldsymbol{B}}}_{\bar{u}}^T \overline{EA} \bar{\underline{\boldsymbol{B}}}_{\bar{u}} \, \mathrm{d}x, \tag{3.6}$$

$$\bar{\underline{\boldsymbol{f}}}_{\bar{u}} = \left[\bar{\underline{\boldsymbol{N}}}_{\bar{u}}^T \bar{N}_p\right]_0^L, \tag{3.7}$$

$$\bar{\underline{\boldsymbol{K}}}_{\bar{w}} = \int_0^L \bar{\underline{\boldsymbol{C}}}_{\bar{w}}^T \overline{EI} \bar{\underline{\boldsymbol{C}}}_{\bar{w}} \, \mathrm{d}x \tag{3.8}$$

$$\tag{3.9}$$

and

$$\bar{\underline{\boldsymbol{f}}}_{\bar{w}} = \int_0^L \bar{\underline{\boldsymbol{N}}}_{\bar{w}}^T \bar{q}(x) \, \mathrm{d}x + \left[\bar{\underline{\boldsymbol{N}}}_{\bar{w}}^T \bar{V}_p\right]_0^L - \left[\bar{\underline{\boldsymbol{B}}}_{\bar{w}}^T \bar{M}_p\right]_0^L. \tag{3.10}$$

3.2 Finite Element Problem Formulation for a Timoshenko Beam

3.2.1 Strong Form

For an arbitrary beam defined in the domain given by $0 \leq x \leq L$, the strong form is given by

$$-\frac{\partial \bar{N}(x)}{\partial x} = 0 \text{ in } 0 \leq x \leq L \tag{3.11}$$

$$\frac{\partial \bar{V}(x)}{\partial x} = -q(x) \text{ in } 0 \leq x \leq L, \tag{3.12}$$

and

$$\frac{\partial \bar{M}(x)}{\partial x} = V(x) \text{ in } 0 \leq x \leq L \tag{3.13}$$

where the Dirichlet and Neumann boundary conditions may be formulated as

$$\begin{aligned} \bar{u} &= \bar{u}_p \text{ on } x = 0 \text{ and/or } x = L \\ \bar{w} &= \bar{w}_p \text{ on } x = 0 \text{ and/or } x = L \\ \bar{\phi} &= \bar{\phi}_p \text{ on } x = 0 \text{ and/or } x = L. \end{aligned}$$

and

$$\begin{aligned} \bar{V} &= \bar{V}_p \text{ on } x = 0 \text{ and/or } x = L \\ \bar{M} &= \bar{M}_p \text{ at } x = 0 \text{ and/or } x = L \\ \bar{N} &= \bar{N}_p \text{ at } x = 0 \text{ and/or } x = L. \end{aligned}$$

respectively. Note that using Timoshenko beam theory, a new degree of freedom is introduced for the internal rotations.

3.2.2 Weak Form

Multiplying Equations (3.11), (3.12) and (3.13) by arbitrary test functions $\delta\bar{u}$, $\delta\bar{w}$ and $\delta\bar{\phi}$ respectively, and integrating over the domain, allows the weak form to be stated as finding $(\bar{u}, \bar{w}, \bar{\phi}) \in \mathbb{U}$ such that

$$\int_0^L \frac{\partial \delta\bar{u}}{\partial x}\left(\overline{EA}\frac{\partial \bar{u}}{\partial x}\right)\mathrm{d}x = \left[\delta\bar{u}\cdot\bar{N}_p\right]_0^L \tag{3.14}$$

$$\int_0^L \frac{\partial \delta\bar{w}}{\partial x}\left[\overline{K_sGA}\left(-\bar{\phi}+\frac{\partial \bar{w}}{\partial x}\right)\right]\mathrm{d}x = \int_0^L \delta\bar{w}\cdot q(x)\mathrm{d}x + \left[\delta\bar{w}\cdot\bar{V}_p\right]_0^L \tag{3.15}$$

$$\int_0^L \frac{\partial \delta\bar{\phi}}{\partial x}\left(\overline{EI}\frac{\partial \bar{\phi}}{\partial x}\right)\mathrm{d}x + \int_0^L \delta\bar{\phi}\cdot\bar{V}(x)\mathrm{d}x = -\left[\delta\bar{\phi}\cdot\bar{M}_p\right]_0^L, \tag{3.16}$$

where Equations (3.14), (3.15), and (3.16) hold for all $(\delta\bar{u}, \delta\bar{w}, \delta\bar{\phi}) \in \mathbb{U}^0$. The pertinent solution and test spaces are given by

$$\begin{aligned} \mathbb{U} &= \left\{\bar{u}, \bar{w}, \bar{\phi} : \text{ sufficiently regular, } \bar{u} = \bar{u}_p,\ \bar{w} = \bar{w}_p,\ \bar{\phi} = \bar{\phi}_p \text{ on } x = 0 \text{ and/or } x = L\right\} \\ \mathbb{U}^0 &= \left\{\delta\bar{w}, \delta\bar{\phi}, \delta\bar{u} : \text{sufficiently regular, } \delta\bar{w} = 0 \text{ where } \bar{w} = \bar{w}_p,\ \delta\bar{u} = 0 \text{ where } \bar{\phi} = \bar{\phi}_p,\ \delta\bar{u} = 0 \text{ where } \bar{u} = \bar{u}_p\right\} \end{aligned}$$

3.2.3 FE Form

The FE formulation is found by introducing the approximations defined by

$$\begin{aligned} \bar{u} &\approx \bar{u}_h = \bar{\underline{\boldsymbol{N}}}_u \bar{\underline{\boldsymbol{a}}}_u \\ \bar{w} &\approx w_h = \bar{\underline{\boldsymbol{N}}}_w \bar{\underline{\boldsymbol{a}}}_w \end{aligned}$$

and

$$\bar{\phi} \approx \bar{\phi}_h = \bar{\underline{\boldsymbol{N}}}_\phi \bar{\underline{\boldsymbol{a}}}_\phi \tag{3.17}$$

into Equations (3.16), (3.14) and (3.15). This gives

$$\begin{bmatrix} \bar{\underline{\boldsymbol{K}}}_{uu} & \underline{\boldsymbol{0}} & \underline{\boldsymbol{0}} \\ \underline{\boldsymbol{0}} & \bar{\underline{\boldsymbol{K}}}_{ww} & -\bar{\underline{\boldsymbol{K}}}_{w\phi} \\ \underline{\boldsymbol{0}} & -\bar{\underline{\boldsymbol{K}}}_{\phi w} & \bar{\underline{\boldsymbol{K}}}_{\phi\phi} \end{bmatrix} \begin{bmatrix} \bar{\underline{\boldsymbol{a}}}_u \\ \bar{\underline{\boldsymbol{a}}}_w \\ \bar{\underline{\boldsymbol{a}}}_\phi \end{bmatrix} = \begin{bmatrix} \bar{\underline{\boldsymbol{f}}}_u \\ \bar{\underline{\boldsymbol{f}}}_w \\ \bar{\underline{\boldsymbol{f}}}_\phi \end{bmatrix} \tag{3.18}$$

where

$$\bar{\underline{\boldsymbol{K}}}_{uu} = \int_0^L \bar{\underline{\boldsymbol{B}}}_u^T \overline{EA} \bar{\underline{\boldsymbol{B}}}_u \mathrm{d}x \tag{3.19}$$

$$\bar{\underline{\boldsymbol{K}}}_{ww} = \int_0^L \bar{\underline{\boldsymbol{B}}}_w^T \overline{K_s GA} \bar{\underline{\boldsymbol{B}}}_w \mathrm{d}x \tag{3.20}$$

$$\bar{\underline{\boldsymbol{K}}}_{w\phi} = \int_0^L \left[\bar{\underline{\boldsymbol{B}}}_\phi^T \overline{EI} \bar{\underline{\boldsymbol{B}}}_\phi + \bar{\underline{\boldsymbol{N}}}_\phi^T \overline{K_s GA} \bar{\underline{\boldsymbol{N}}}_\phi \right] \mathrm{d}x \tag{3.21}$$

$$\bar{\underline{\boldsymbol{f}}}_u = \left[\bar{\underline{\boldsymbol{B}}}_u^T \bar{N}_p \right]_0^L \tag{3.22}$$

$$\bar{\underline{\boldsymbol{f}}}_w = \left[\bar{\underline{\boldsymbol{N}}}_w^T \bar{V}_p \right]_0^L \tag{3.23}$$

$$\bar{\underline{\boldsymbol{f}}}_\phi = - \left[\bar{\underline{\boldsymbol{N}}}_\phi^T \bar{M}_p \right]_0^L . \tag{3.24}$$

4 A Two Scale Formulation - FE^2 Method

In order to integrate both the presence of material heterogenities and their influence on structural elements, in particular beams, a method known as FE^2 is considered. This method, as the name suggest, involves using a nested solution procedure that links at least two independent FE analyses representing different geometric scales. Presently, the macroscale problem is modelled using structural beam elements, while the subscale problem is modelled using two-dimensional continuum elements. By linking the scales, it is possible to exploit the computational efficiency of the macroscale beam model while incorporating the microstructural effects.

4.1 Nested Finite Element Procedure

The general nested FE procedure can be implemented as shown in Figure 4.1. Note that for simplicity the figure only considers Euler-Bernoulli kinematics. The macroscale beam must first be discretised by finite elements and have an independent RVE assigned to each macroscale integration point.

Generally, for non-linear problems, the external load is then applied in an incremental procedure. Inside each macroscale integration point, the respective values of the macroscale measures $\bar{\epsilon}^0$, $\bar{\kappa}$, and/or $\bar{\gamma}$ are determined based on the choice of beam model. Recall that an overline signifies a macroscale value. The macroscale measures are then used to formulate subscale boundary conditions that are applied to the RVE. This step is known as prolongation. Using the formulated boundary conditions, a classic boundary value problem on the RVE is solved. The resulting stress field is then homogenised to obtain the effective bending stiffness, axial stiffness and in the case of a Timoshenko beam, shear stiffness. This prolongation and homogenisation procedure must be carried out for each macroscale integration point.

Once the macroscale stiffness is computed it is possible to determine if the internal and external macroscopic forces are in balance. If this is the case, convergence of the equilibrium iterations has been achieved, and the process repeats for the next load increment. If equilibrium is not achieved, the macroscopic nodal displacement vector is updated using, e.g. the Newton method. It is important to note however, that when all material components are assumed to have a linear-elastic response, applying the load incrementally and carrying out equilibrium iterations is unnecessary.

Complete implementation of a nested FE procedure is not within the scope of this work. The main focus however, outlined in red in Figure 4.1, is to determine a prolongation and homogenisation method that effectively captures the material stiffness under bending, axial and in particular, shear loading. This is discussed in greater detail in the following section.

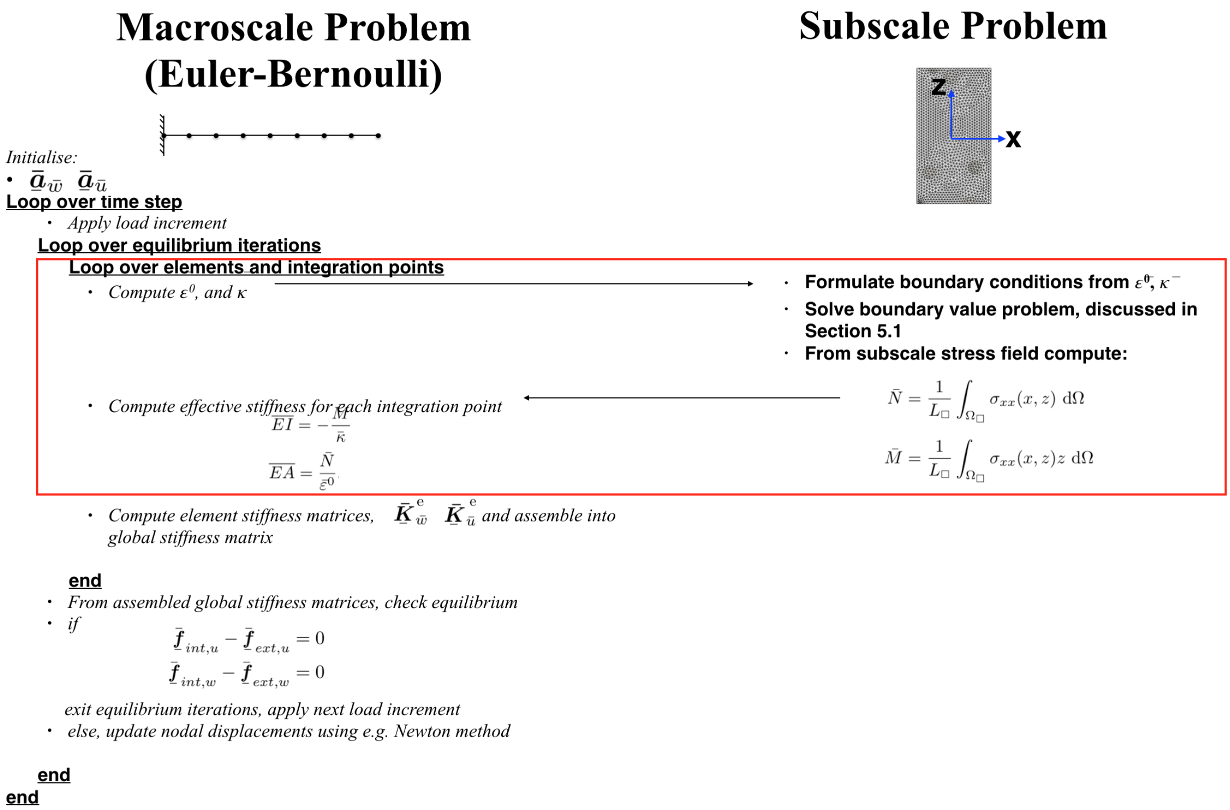

Figure 4.1: Nested FE procedure.

4.2 Two Scale Formulation for Beams

Figure 4.2 illustrates the main focus of the current work. The first goal is to determine how to prolong the macroscale deformation behaviour, taken at some macroscale integration point $x = \bar{x}$, to the subscale RVE. More specifically, this process can be described as making the RVE deform based on given values of $\bar{\epsilon}^0$, $\bar{\kappa}$ and/or $\bar{\gamma}$, depending on the choice of the macroscale kinematics.

With the assumption that the macroscale deformation varies at most linearly within the RVE, the deformation field of the RVE is decomposed such that

$$\boldsymbol{u} = \boldsymbol{u}^M + \boldsymbol{u}^S,$$

where $\boldsymbol{u}^M$ denotes the macroscale deformation field and $\boldsymbol{u}^S$ denotes the subscale fluctuations. Expressing the macroscale deformation on the subscale RVE is done using first order Taylor expansions of the macroscale kinematic quantities around $\bar{x}$, and gives u_x^M and u_z^M as follows:

$$\boldsymbol{u}^M = \begin{bmatrix} u_x^M \\ u_z^M \end{bmatrix}$$

where

$$\begin{aligned} u_x^M &= \bar{u}^0(\bar{x}) - z\bar{\phi}(\bar{x}) + \frac{\partial \bar{u}^0(\bar{x})}{\partial x}\left[x - \bar{x}\right] - z\frac{\partial \bar{\phi}(\bar{x})}{\partial x}\left[x - \bar{x}\right] \\ u_z^M &= \bar{w}(\bar{x}) + \frac{\partial \bar{w}(\bar{x})}{\partial x}\left[x - \bar{x}\right]. \end{aligned}$$

In a physical sense, this means that the macroscale deformation is decomposed into terms that cause rigid body motion of the RVE, i.e. $\bar{u}(\bar{x})$ and $\bar{w}(\bar{x})$, and terms that induce stress. Perhaps the most direct way in which to enforce the transition from the macroscale to subscale, is by prescribing $\boldsymbol{u} = \boldsymbol{u}^M$ on the boundaries, through Dirichlet boundary conditions. Dirichlet boundary conditions are however not the only possibility.

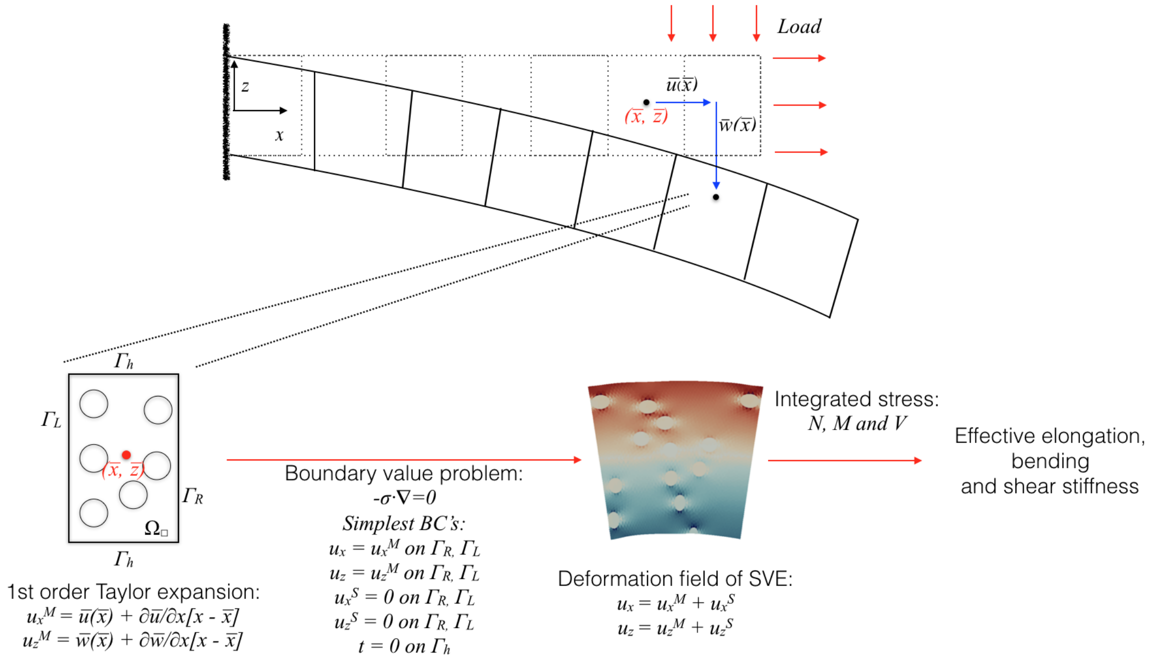

Figure 4.2: Two scale formulation for beams.

Given values for $\bar{\epsilon}^0$, $\bar{\kappa}$, and $\bar{\gamma}$ can be prolonged onto the RVE using either Neumann or periodic boundary conditions. This is discussed further in later sections.

Once the prolongation method is determined, it is possible to solve the boundary value problem on the RVE. From the obtained solution of the boundary value problem, it is necessary to determine a method with which the subscale stress field can be related to macroscale values. This is known as homogenisation, and is carried out by averaging the subscale stress field over the RVE. Through the relationships between axial strain and normal force, curvature and bending moment, as well as shear strain and shear force, the effective stiffness of the heterogeneous material can be found. This is again discussed in more detail in the coming sections.

5 Subscale Problem Formulation

As discussed in Section 4, the subscale problem is defined on a representative sample of the substructure, referred to as an RVE. The size of the RVE must be sufficiently large, such that it is capable of characterising the material heterogeneities and capturing the subscale fluctuations. It must also however, be small enough such that it is possible to accurately resolve the subscale details and such that the considered Taylor expansion is accurate. Finding an RVE is an extensive and delicate task, as it must give a perfect representation of the subscale characteristics. It is here that the distinction between a statistical volume element (SVE) and an RVE is made. An SVE may be considered as a random sample taken from the material substructure. As a result, there is no guarantee that the size of the SVE, or the consistency of its small scale material components, reflects the substructure as a whole. In order to obtain a representative result, multiple SVEs must be considered, and their results averaged. From this point forward, all samples of the subscale material are referred to as SVEs.

5.1 General 2D Boundary Value Problem Formulation

Through prolongation of macroscale deformations, a boundary value problem is constructed and solved on an SVE, the general formulation of which is introduced below. The SVE is assumed to be thin in nature, thus allowing an assumption of plane stress to be adopted.

5.1.1 Strong Form

The strong form for the SVE shown in Figure 5.1 is given by

$$-\boldsymbol{\sigma} \cdot \boldsymbol{\nabla} = \boldsymbol{b} \text{ in } \Omega_\square \tag{5.1}$$

$$\boldsymbol{t} = \boldsymbol{t}_p \text{ on } \Gamma_N \tag{5.2}$$

$$\boldsymbol{u} = \boldsymbol{u}_p \text{ on } \Gamma_D \tag{5.3}$$

where $\boldsymbol{\sigma}$ is Cauchy's stress tensor, ∇ is defined as the gradient operator, $\boldsymbol{f}$ being the body force, $\boldsymbol{t}$ denotes the traction and $\boldsymbol{u}$ the displacement vector.

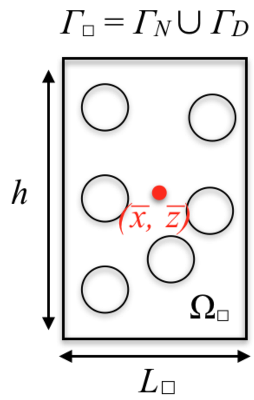

Figure 5.1: The considered subscale domain, an SVE.

5.1.2 Weak Form

In order to derive the weak formulation, Equation (5.1) must first be multiplied by the arbitrary test function $\delta\boldsymbol{u} \in \mathbb{U}^0_\square$ where

$$\mathbb{U}^0_\square = \left\{ \delta\boldsymbol{u} : \int_\Omega |\delta\boldsymbol{u}|^2 + |\delta\boldsymbol{u} \otimes \boldsymbol{\nabla}|^2 \ \mathrm{d}\Omega < \infty, \delta\boldsymbol{u} = \boldsymbol{0} \text{ on } \Gamma_D \right\},$$

and then integrated over the domain $\Omega_\square$. This gives

$$-\int_{\Omega_\square} \delta\boldsymbol{u} \cdot (\boldsymbol{\sigma} \cdot \boldsymbol{\nabla}) \ \mathrm{d}\Omega = \int_{\Omega_\square} \delta\boldsymbol{u} \cdot \boldsymbol{f} \ \mathrm{d}\Omega. \tag{5.4}$$

Considering that

$$(\delta\boldsymbol{u} \cdot \boldsymbol{\sigma}) \cdot \boldsymbol{\nabla} = (\delta\boldsymbol{u} \otimes \boldsymbol{\nabla}) : \boldsymbol{\sigma} + \delta\boldsymbol{u} \cdot (\boldsymbol{\sigma} \cdot \boldsymbol{\nabla})$$

Equation (5.4) can in turn be expressed as

$$\int_{\Omega_\square} (\delta\boldsymbol{u} \otimes \boldsymbol{\nabla}) : \boldsymbol{\sigma} \ \mathrm{d}\Omega = \int_{\Omega_\square} \delta\boldsymbol{u} \cdot \boldsymbol{b} \ \mathrm{d}\Omega + \int_{\Omega_\square} (\delta\boldsymbol{u} \cdot \boldsymbol{\sigma}) \cdot \boldsymbol{\nabla} \ \mathrm{d}\Omega \quad \forall \ \delta\boldsymbol{u} \in \mathbb{U}^0_\square.$$

Using the definition of the Cauchy stress tensor, namely $\boldsymbol{\sigma} \cdot \boldsymbol{n} = \boldsymbol{t}$ and Gauss' theorem, which states that

$$\int_{\Omega_\square} \bullet \cdot \boldsymbol{\nabla} \ \mathrm{d}\Omega = \int_\Gamma \bullet \cdot \boldsymbol{n} \ \mathrm{d}\Gamma \tag{5.5}$$

where $\boldsymbol{n}$ is the outward facing normal, the second term may be rewritten such that Equation (5.5) is given by

$$\int_{\Omega_\square} (\delta\boldsymbol{u} \otimes \boldsymbol{\nabla}) : \boldsymbol{\sigma} \ \mathrm{d}\Omega = \int_{\Omega_\square} \delta\boldsymbol{u} \cdot \boldsymbol{b} \ \mathrm{d}\Omega + \int_{\Gamma_\square} \delta\boldsymbol{u} \cdot \boldsymbol{t} \ \mathrm{d}\Gamma \quad \forall \ \delta\boldsymbol{u} \in \mathbb{U}^0_\square.$$

Given that $\delta\boldsymbol{u} = \boldsymbol{0}$ on Γ_D, and $\boldsymbol{t} = \boldsymbol{t}_p$ on Γ_N the problem reduces to finding $\boldsymbol{u} \in \mathbb{U}_\square$ that fulfills

$$\int_{\Omega_\square} (\delta\boldsymbol{u} \otimes \boldsymbol{\nabla}) : \boldsymbol{\sigma} \, \mathrm{d}\Omega = \int_{\Omega_\square} \delta\boldsymbol{u} \cdot \boldsymbol{b} \, \mathrm{d}\Omega + \int_{\Gamma_N} \delta\boldsymbol{u} \cdot \boldsymbol{t}_p \, \mathrm{d}\Gamma \quad \forall \, \delta\boldsymbol{u} \in \mathbb{U}^0_\square, \tag{5.6}$$

where

$$\mathbb{U}_\square = \left\{ \boldsymbol{u} : \int_\Omega |\boldsymbol{u}|^2 + |\boldsymbol{u} \otimes \boldsymbol{\nabla}|^2 \, \mathrm{d}\Omega < \infty, \boldsymbol{u} = \boldsymbol{u}_p \text{ on } \Gamma_D \right\}.$$

5.1.3 Finite Element Form

The finite element problem is formulated by first introducing the displacement approximation according to Galerkin's method:

$$\underline{\boldsymbol{u}} \approx \underline{\boldsymbol{u}}_h = \underline{\boldsymbol{N}}_u \underline{\boldsymbol{a}}_u,$$

where the underline indicated matrix notation. The shape function matrix and nodal value vector are given by

$$\underline{\boldsymbol{N}}_u = \begin{bmatrix} N_1 & 0 & N_2 & 0 & \dots & N_{nnodes,u} & 0 \\ 0 & N_1 & 0 & N_2 & \dots & 0 & N_{nnodes,u} \end{bmatrix} \text{ and } \underline{\boldsymbol{a}}_u = \begin{bmatrix} u_{x,1} \\ u_{z,1} \\ u_{x,2} \\ u_{z,2} \\ \dots \\ u_{x,nnodes,u} \\ u_{z,nnodess,u} \end{bmatrix}$$

respectively. Similarly, the test function $\delta\boldsymbol{u}$ may be approximated as

$$\delta\underline{\boldsymbol{u}} \approx \delta\underline{\boldsymbol{u}}_h = \underline{\boldsymbol{N}}_u \delta\underline{\boldsymbol{a}}_u.$$

It is then possible to express $(\delta\boldsymbol{u} \otimes \boldsymbol{\nabla}) : \boldsymbol{\sigma}$ in matrix notation as

$$\begin{aligned} (\delta\boldsymbol{u} \otimes \boldsymbol{\nabla}) : \boldsymbol{\sigma} &= (\underline{\boldsymbol{\nabla}}\delta\underline{\boldsymbol{u}})^T \underline{\boldsymbol{\sigma}} \\ &= (\underline{\boldsymbol{\nabla}}\delta\underline{\boldsymbol{u}})^T \underline{\boldsymbol{D}}\underline{\boldsymbol{\varepsilon}} \\ &= (\underline{\boldsymbol{\nabla}}\delta\underline{\boldsymbol{u}})^T \underline{\boldsymbol{D}}(\underline{\boldsymbol{\nabla}}\underline{\boldsymbol{u}}) \end{aligned}$$

where $\underline{\boldsymbol{D}}$ denotes Hooke's stiffness tensor and $\underline{\boldsymbol{\nabla}}$ denotes the gradient operator. Introducing the displacement approximations results in

$$\begin{aligned} (\underline{\boldsymbol{\nabla}}\delta\underline{\boldsymbol{u}})^T \underline{\boldsymbol{D}}(\underline{\boldsymbol{\nabla}}\underline{\boldsymbol{u}}) &\approx (\underline{\boldsymbol{\nabla}}\underline{\boldsymbol{N}}_u\delta\underline{\boldsymbol{a}}_u)^T \underline{\boldsymbol{D}}(\underline{\boldsymbol{\nabla}}\underline{\boldsymbol{N}}_u\underline{\boldsymbol{a}}_u) \\ &\approx (\underline{\boldsymbol{B}}_u\delta\underline{\boldsymbol{a}}_u)^T \underline{\boldsymbol{D}}(\underline{\boldsymbol{B}}_u\underline{\boldsymbol{a}}_u). \end{aligned}$$

Equation (5.6), may then be given in it's FE form as

$$\int_{\Omega_\square} \boldsymbol{\sigma} : [\delta\boldsymbol{u} \otimes \boldsymbol{\nabla}] \, \mathrm{d}\Omega \approx \delta\underline{\boldsymbol{a}}_u^T \int_{\Omega_\square} \underline{\boldsymbol{B}}_u^T \underline{\boldsymbol{D}}\underline{\boldsymbol{B}}_u \, \mathrm{d}\Omega \underline{\boldsymbol{a}}_u = \delta\underline{\boldsymbol{a}}_u^T \underline{\boldsymbol{K}}_{uu}\underline{\boldsymbol{a}}_u,$$

and

$$\int_{\Omega_\square} \delta\boldsymbol{u} \cdot \boldsymbol{b} \, \mathrm{d} + \int_{\Gamma_N} \delta\boldsymbol{u} \cdot \boldsymbol{t}_p \, \mathrm{d}\Gamma \approx \delta\underline{\boldsymbol{a}}_u^T \left[\int_{\Omega_\square} \underline{\boldsymbol{N}}_u^T \underline{\boldsymbol{b}} \, \mathrm{d}\Omega + \int_{\Gamma_N} \underline{\boldsymbol{N}}_u^T \underline{\boldsymbol{t}}_p \, \mathrm{d}\Gamma \right] = \delta\underline{\boldsymbol{a}}_u^T \underline{\boldsymbol{f}}_u$$

Finally, as the system of equations must hold for all arbitrary $\delta\underline{\boldsymbol{a}}_u$, it can be summarised by solving for the nodal displacements $\underline{\boldsymbol{a}}_u$ from

$$\underline{\boldsymbol{K}}_{uu}\underline{\boldsymbol{a}}_u = \underline{\boldsymbol{f}}_u.$$

5.2 Generating SVEs

The substructure considered in future analyses consists of soft inclusions surrounded by a hard matrix material. Figure 5.2 shows a 50×50 mm domain, from which SVEs of varying length, a constant height of 10 mm and a thickness of 1 mm are sampled. Note that the circles indicate the soft inclusions in the material. The sampling field has a 12 % volume fraction of soft inclusions, where each inclusion has a diameter of 1 mm. A Young's modulus of 210 GPa is assigned to the hard matrix, whereas the soft inclusions are given a value of 10 GPa. Both materials are assumed to behave linear elastically.

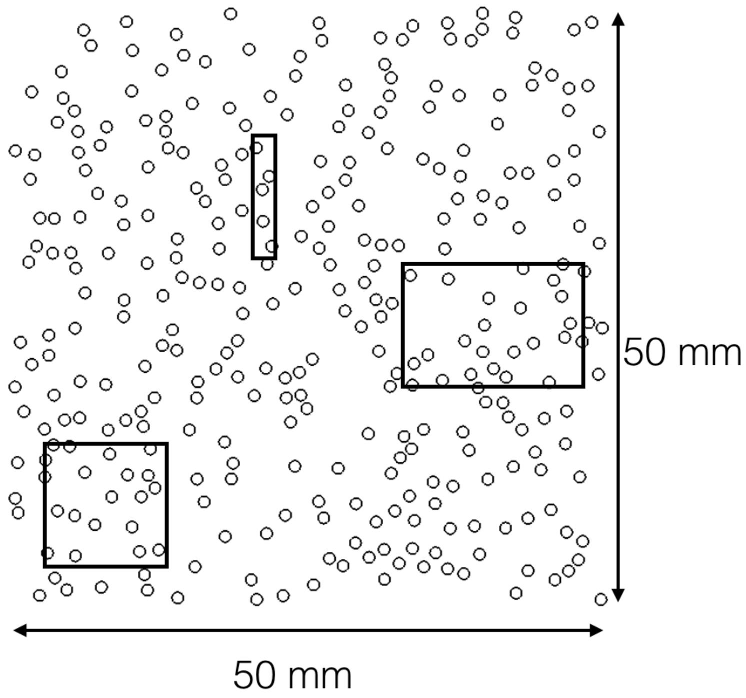

Figure 5.2: Domain from which SVEs of varying length are sampled, some examples of which are shown.

6 Computational Homogenisation Based on Euler-Bernoulli Beam Theory

The first considered prolongation and homogenisation technique is perhaps the most straight forward. The macroscale behaviour, in this case, is described by Euler-Bernoulli beam kinematics and the macroscale to subscale transition takes place using Dirichlet boundary conditions, shown in Section 6.1. The pertinent boundary value problem is presented in Section 6.2, while the subscale to macroscale transition is discussed in Section 6.3.

6.1 Macroscale - Subscale Transition

Using Euler-Bernoulli beam theory it is possible to impose the macroscale measures of axial elongation and bending onto the SVE. As previously discussed, the macroscale deformation is expressed on the subscale using a first order Taylor expansion. As such, the kinematics of Euler-Bernoulli beam theory gives that

$$u_x^M = \bar{u}^0(\bar{x}) - z\frac{\partial \bar{w}(\bar{x})}{\partial x} + \frac{\partial \bar{u}^0(\bar{x})}{\partial x}\left[x - \bar{x}\right] - z\frac{\partial^2 \bar{w}(\bar{x})}{\partial x^2}\left[x - \bar{x}\right]$$

and

$$u_z^M = \bar{w}(\bar{x}) + \frac{\bar{w}(\bar{x})}{\partial x}\left[x - \bar{x}\right].$$

It is assumed that the stress response will be invariant to rigid body motion. When considering u_x^M and u_z^M, the first terms, $\bar{u}^0(\bar{x})$ and $\bar{w}(\bar{x})$, simply cause a translation. They may, for that reason be disregarded. Similarly, the combination of the second terms in both u_x^M and u_z^M, given by

$$-z\frac{\partial \bar{w}(\bar{x})}{\partial x} \text{ and } \frac{\partial \bar{w}(\bar{x})}{\partial x}[x - \bar{x}]$$

respectively, causes a rigid body rotation. They may also be disregarded. This allows the Taylor expansions to be simplified to

$$u_x^M = \bar{\varepsilon}^0\left[x - \bar{x}\right] - z\bar{\kappa}\left[x - \bar{x}\right],$$

and

$$u_z^M = 0.$$

Dirichlet boundary conditions represent the strongest way in which the macroscale measures may be imposed on the SVE. Imposing pure elongation, $\bar{\varepsilon}^0$ on an SVE of length $L_\square$ using Dirichlet boundary conditions gives

$$u_x = u_x^M = \begin{cases} \frac{\bar{\varepsilon}^0 \cdot L_\square}{2} & \text{on } \Gamma_R \\ -\frac{\bar{\varepsilon}^0 \cdot L_\square}{2} & \text{on } \Gamma_L, \end{cases}$$

where Γ_L and Γ_R are defined in Figure 6.1. Similarly, pure curvature, $\bar{\kappa}$, is imposed through

$$u_x = u_x^M = \begin{cases} -\frac{z\bar{\kappa}L_\square}{2} & \text{on } \Gamma_R \\ \frac{z\bar{\kappa} \cdot L_\square}{2} & \text{on } \Gamma_L. \end{cases}$$

Finally, applying a combination of both gives the equivalent Dirichlet boundary conditions

$$u_x^M = \begin{cases} \frac{\bar{\varepsilon}^0 \cdot L_\square}{2} - \frac{z\bar{\kappa}L_\square}{2} & \text{on } \Gamma_R \\ -\frac{\bar{\varepsilon}^0 \cdot L_\square}{2} + \frac{z\bar{\kappa}L_\square}{2} & \text{on } \Gamma_L. \end{cases}$$

All are illustrated in Figure 6.1.

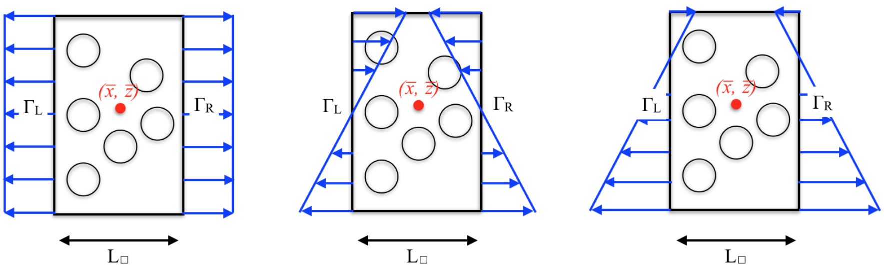

Figure 6.1: Imposed boundary conditions on the SVE for pure elongation (left), pure curvature (middle) and a combination (right).

It is important to note that the way in which the boundary conditions constraining vertical displacement are prescribed, namely u_z^M on Γ_L and Γ_R, is a point of discussion. For example, prescribing $u_z^M = 0$ as a Dirichlet boundary condition will yield a deformation shown in Figure 6.2. This is unphysical. Currently, in order to circumvent this, boundary conditions constraining vertical displacement are not prescribed. However in order to prevent rigid body motion, the centre of the SVE is fixed, i.e $u_z(\bar{x}, \bar{z}) = 0$.

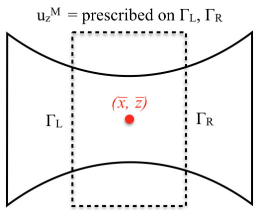

Figure 6.2: Unphysical deformation field of the SVE due to constrained vertical displacement on Γ_L and Γ_R.

6.2 Boundary Value Problem Formulation

The boundary conditions formulated in the previous section are used to prolong the macroscale values of elongation and curvature to the SVE. For specific chosen values of $\bar{\varepsilon}^0$ and $\bar{\kappa}$, a traditional boundary value problem is then solved, giving rise to the associated stress distribution of the SVE. The SVE is assumed to be thin in nature, which allows the plane stress assumption to be adopted.

6.2.1 Strong Formulation

Considering the SVE illustrated in Figure 6.3 and neglecting the body force, the standard strong form of the equilibrium equations are given by

$$-\boldsymbol{\sigma} \cdot \boldsymbol{\nabla} = \mathbf{0} \text{ in } \Omega_\square \tag{6.1}$$
$$\boldsymbol{t} = \mathbf{0} \text{ on } \Gamma_h \tag{6.2}$$
$$u_x = u_x^M = \bar{\varepsilon}^0 \left[x - \bar{x}\right] - z\bar{\kappa}\left[x - \bar{x}\right] \text{ on } \Gamma_L \text{ and } \Gamma_R \tag{6.3}$$
$$u_z = 0 \text{ on } (x, z) = (\bar{x}, \bar{z}). \tag{6.4}$$

Note that, in order to remain consistent to the macroscale beam model, $\boldsymbol{t} = 0$ on Γ_h.

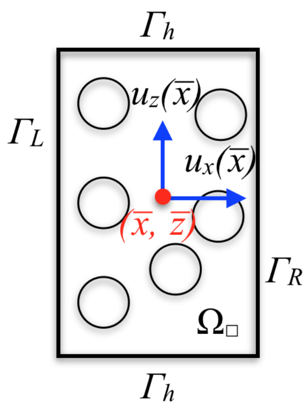

Figure 6.3: Statistical volume element.

6.2.2 Weak Formulation

In order to derive the weak formulation, Equation (6.1) must first be multiplied by the arbitrary test function $\delta\boldsymbol{u} \in \mathbb{U}_\square^0$ where

$$\mathbb{U}_\square^0 = \{\delta\boldsymbol{u} : \int_\Omega |\delta\boldsymbol{u}|^2 + |\delta\boldsymbol{u} \otimes \boldsymbol{\nabla}|^2 \, \mathrm{d}\Omega < \infty, \delta u_x = 0 \text{ on } \Gamma_R \text{ and } \Gamma_L, \delta u_z = 0 \text{ on } (x, z) = (\bar{x}, \bar{z})\},$$

and then integrated over the domain $\Omega_\square$. Referring to the steps taken in Section 5.1.2, this eventually results in

$$\int_{\Omega_\square} (\delta\boldsymbol{u} \otimes \boldsymbol{\nabla}) : \boldsymbol{\sigma} \, \mathrm{d}\Omega = \int_{\Gamma_\square} \delta\boldsymbol{u} \cdot \boldsymbol{t} \, \mathrm{d}\Gamma \quad \forall \, \delta\boldsymbol{u} \in \mathbb{U}_\square^0.$$

Given that $\boldsymbol{t} = 0$ on Γ_h, the problem reduces to finding $\boldsymbol{u} \in \mathbb{U}_\square$ that fulfills

$$\int_{\Omega_\square} (\delta \boldsymbol{u} \otimes \boldsymbol{\nabla}) : \boldsymbol{\sigma} \; \mathrm{d}\Omega = \int_{\Gamma_R \cup \Gamma_L} \delta \boldsymbol{u} \cdot \boldsymbol{t} \; \mathrm{d}\Gamma \quad \forall \; \delta \boldsymbol{u} \in \mathbb{U}_\square^0, \tag{6.5}$$

where

$$\mathbb{U}_\square = \{\boldsymbol{u} : \int_\Omega |\boldsymbol{u}|^2 + |\boldsymbol{u} \otimes \boldsymbol{\nabla}|^2 \; \mathrm{d}\Omega < \infty, u_x = u_x^M \text{ on } \Gamma_R \text{ and } \Gamma_L, u_z(\bar{x}, \bar{z}) = 0\}.$$

Note that, formally, the point-wise constraint in Equation (6.4) has to be replaced by an integrated measure for the continuous spaces. However, since the constraint is merely controlling rigid body translations, and thus not generating a corresponding reaction force, it is of no practical interest.

6.2.3 Finite Element Formulation

Introducing the displacement approximations

$$\underline{\boldsymbol{u}} \approx \underline{\boldsymbol{u}}_h = \underline{\boldsymbol{N}}_u \underline{\boldsymbol{a}}_u \text{ and } \delta \underline{\boldsymbol{u}} \approx \delta \underline{\boldsymbol{u}}_h = \underline{\boldsymbol{N}}_u \delta \underline{\boldsymbol{a}}_u,$$

into the weak formulation shown in Equation (6.5) yields

$$\int_{\Omega_\square} \boldsymbol{\sigma} : [\delta \boldsymbol{u} \otimes \boldsymbol{\nabla}] \; \mathrm{d}\Omega \approx \delta \underline{\boldsymbol{a}}_u^T \int_{\Omega_\square} \underline{\boldsymbol{B}}_u^T \underline{\boldsymbol{D}} \underline{\boldsymbol{B}}_u \; \mathrm{d}\Omega \underline{\boldsymbol{a}}_u = \delta \underline{\boldsymbol{a}}_u^T \underline{\boldsymbol{K}}_{uu} \underline{\boldsymbol{a}}_u$$

and

$$\int_{\Gamma_L \cup \Gamma_R} \delta \boldsymbol{u} \cdot \boldsymbol{t}_p \; \mathrm{d}\Gamma \approx \delta \underline{\boldsymbol{a}}_u^T \int_{\Gamma_L \cup \Gamma_R} \underline{\boldsymbol{N}}_u^T \underline{\boldsymbol{t}}_p \; \mathrm{d}\Gamma = \delta \underline{\boldsymbol{a}}_u^T \underline{\boldsymbol{f}}_u.$$

Finally, this system of equations can be summarised by finding $\underline{\boldsymbol{a}}_u$ such that

$$\underline{\boldsymbol{K}}_{uu} \underline{\boldsymbol{a}}_u = \underline{\boldsymbol{f}}_u.$$

6.3 Subscale - Macroscale Transition

After obtaining the solution to the boundary value problem on the SVE, it is possible to determine the homogenised bending and axial stiffness for the heterogeneous material. The resulting axial stress field for a number of SVE's of varying length under either pure axial elongation or bending are shown in Figure 6.4.

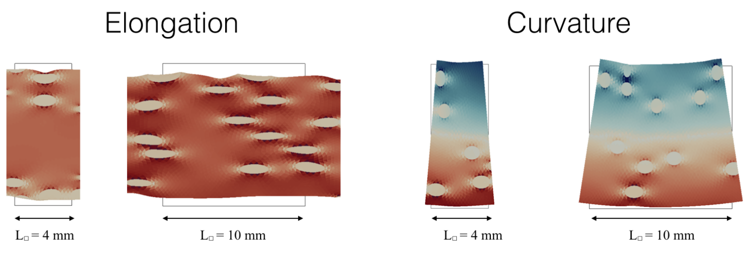

Figure 6.4: Axial stress distribution for an SVE that is elongated (left) and one with curvature prescribed (right).

Due to linearity, the two load cases may be considered independently. First pure elongation is applied, then pure curvature. The average values of the axial force and bending moment over the SVE are computed as

$$\bar{N} = \frac{1}{L_\square} \int_{\Omega_\square} \sigma_{xx}(x, z) \; \mathrm{d}\Omega$$

and

$$\bar{M} = \frac{1}{L_\square} \int_{\Omega_\square} \sigma_{xx}(x, z) z \; \mathrm{d}\Omega.$$

For the given vale of $\bar{\varepsilon}^0$, the elongation stiffness is then computed as

$$\overline{EA} = \frac{\bar{N}}{\bar{\varepsilon}^0} \text{ for } \bar{\kappa} = 0.$$

Similarly, for the given value of $\bar{\kappa}$

$$\overline{EI} = -\frac{\bar{M}}{\bar{\kappa}} \text{ for } \bar{\varepsilon}^0 = 0$$

6.4 Bounding The Effective Stiffness as $L_\square \to 0$

In order to verify the reliability of the homogenised material properties, a modified Voigt assumption is considered, namely

$$\bar{E}_V = \frac{|\Omega_\square^{hard}|E_{hard} + |\Omega_\square^{soft}|E_{soft}}{|\Omega_\square|}.$$

The Voigt assumption is formulated by assuming that the strain field over an SVE is constant. Note that the domain $\Omega_\square$ may be decomposed into hard and soft constituents.

As the length $L_\square \to 0$, it can be shown that the effective Young's modulus obtained through the prolongation and homogenisation scheme will approach the modified Voigt assumption, given by

$$\bar{E}_V = 186 \text{ GPa}.$$

According to this limit case, the homogenised bending and axial stiffness for SVE's with a height of 10 mm and thickness of 1 mm should approach

$$\overline{E_V I} = 1.55 \cdot 10^7 \text{ Nmm}^2 \text{ and } \overline{E_V A} = 1.86 \cdot 10^6 \text{ N}$$

as $L_\square \to 0$.

6.4.1 Under the Application of Pure Axial Elongation

Considering the case of pure axial elongation on an SVE, it is possible to show that the effective Young's Modulus E approaches the Voigt bound $\bar{E}_V$ as the length $L_\square \to 0$. This involves first showing that a sufficiently small SVE has a uniaxial stress state under pure elongation. Given this simplified problem it is then shown that the obtained strain field is constant and therefore equivalent to what is assumed by Voigt.

Due to the applied boundary conditions, namely $u_x = u_x^M$ on Γ_L and Γ_R, the horizontal displacement of the SVE as $L_\square \to 0$ is well defined. Namely,

$$u_x(x,z) = \bar{\varepsilon}^0 \cdot [x - \bar{x}].$$

This however is not the case for the vertical displacement. The assumption is made that due to the dimension of the SVE, specifically that $L_\square \to 0$, it is sufficient to only consider the first term of the Taylor expansion. As such

$$u_z(x,z) = \bar{w}(\bar{x}).$$

In order to satisfy equilibrium, it is required that

$$-\boldsymbol{\sigma} \cdot \boldsymbol{\nabla} = \boldsymbol{0} \text{ in } \Omega_\square$$

when body forces are disregarded. In other words

$$\frac{\partial \sigma_{xx}}{\partial x} + \frac{\partial \sigma_{xz}}{\partial z} = 0$$

and

$$\frac{\partial \sigma_{xz}}{\partial x} + \frac{\partial \sigma_{zz}}{\partial z} = 0. \tag{6.6}$$

Given the restrictions on the displacement, it is clear that shear deformation is not present. This implies that $\sigma_{xz} = 0$. Considering (6.6) this in turn requires that σ_{zz} be constant across the height of the SVE. As the tractions are prescribed as $\boldsymbol{t} = \boldsymbol{0}$ on Γ_h, $\sigma_{zz} = 0$ must also be satisfied on Γ_h. This in turn implies that $\sigma_{zz} = 0$ on $\Omega_\Box$. Therefore a state a of uniaxial stress is obtained for pure axial elongation as $L_\Box \to 0$.

As a state of uniaxial stress is obtained, the usual stress-strain relationship for plane stress given by

$$\begin{bmatrix} \varepsilon_{xx} \\ \varepsilon_{zz} \\ \varepsilon_{xz} \end{bmatrix} = \begin{bmatrix} 1/E & -\nu/E & 0 \\ -\nu/E & 1/E & 0 \\ 0 & 0 & 1/2G \end{bmatrix} \begin{bmatrix} \sigma_{xx} \\ \sigma_{zz} \\ \sigma_{xz} \end{bmatrix}$$

can be reduced to simply $\sigma_{xx} = E\varepsilon_{xx}$. This allows for the direct comparison of the Voigt bound and the effective modulus. As previously eluded to, the Voigt bound is formulated assuming the subscale strain field, denoted ε_{xx}, across the SVE is uniform, i.e that the effective strain

$$\bar{\varepsilon}_{xx} = \frac{1}{\Omega_\Box} \int_{\Omega_\Box} \varepsilon_{xx} \ \mathrm{d}\Omega = \bar{\varepsilon}^0.$$

Given the assumption that is made for the deformation field, as $L_\Box \to 0$, $\varepsilon_{xx} = \bar{\varepsilon}^0$, i.e that the subscale strain field is uniform across the SVE. This is equivalent to the assumptions made by Voigt, and therefore the equivalent modulus $\bar{E} = \bar{E}_V$ as $L_\Box \to 0$.

6.4.2 Under the Application of Pure Curvature

Using a similar process, it is also possible to show that for the limit case as $L_\Box \to 0$, that the effective bending stiffness will approach the modified Voigt assumption. Due to the applied boundary conditions, namely $u_x = u_x^M$ on Γ_L and Γ_R the horizontal displacement of the SVE as $L_\Box \to 0$ is well defined. Namely,

$$u_x(x,z) = -z\bar{\kappa}\left[x - \bar{x}\right].$$

Making use of the same assumptions introduced in Section 6.4.1, a state of uniaxial stress is obtained.

For an SVE with length approaching zero, the macroscale moment is computed as

$$\begin{aligned} \bar{M}(x) &= \int_{-h/2}^{h/2} \sigma_{xx}(x,z) z \ \mathrm{d}z \\ &= \int_{-h/2}^{h/2} -E(x,z)\bar{\kappa}(x) z^2 \ \mathrm{d}z. \end{aligned}$$

Due to the statistical nature of the problem, with a sufficiently large number of samples, the Young's modulus will be on average invariant with height. It will also, on average be given by the Modified Voigt assumption. Therefore

$$\bar{M}(x) = \overline{E_V I}\bar{\kappa}(x).$$

Given the limiting case as $\mathrm{L}_\Box \to 0$, the bending stiffness will approach the modified Voigt assumption $\overline{E_V I}$

6.5 Results

In order to verify the accuracy of the proposed prolongation and homogenisation methods, both homogeneous and heterogeneous SVEs are considered.

6.5.1 Homogeneous SVE

Figure 6.5 shows the resulting bending and axial stiffness when homogenous SVEs with a Young's modulus $E = 210$ GPa are analysed using the prolongation and homogenisation methods discussed in Sections 6.1 through 6.3. The expected values for the bending and axial stiffness are therefore

$$\overline{EI} = 175 \times 10^5 \ \text{Nmm}^2 \text{ and } \overline{EA} = 210 \times 10^4 \ \text{N}.$$

Figure 6.5 not only shows that the correct material stiffness is achieved, but also that the modeling choices cause no inherent dependence on the length of the SVE. Any dependence on SVE length seen in the heterogeneous case, is therefore strictly due to the distribution of soft inclusions.

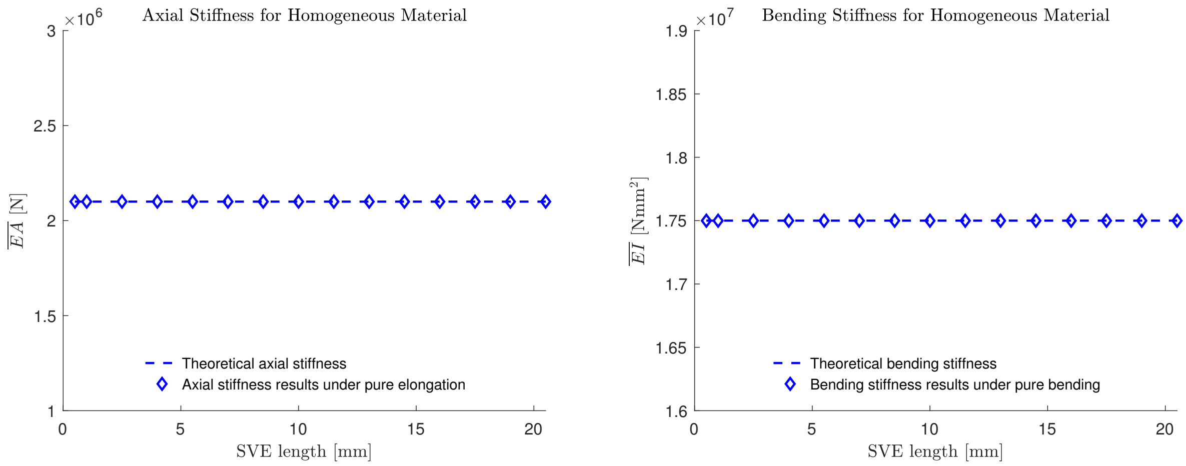

Figure 6.5: Resulting effective axial (left) and bending (right) stiffness for homogeneous SVEs of varying length. Prolongation and Homogenisation method formulated using Euler-Bernoulli beam theory.

6.5.2 Heterogeneous SVE

As discussed in Section 5.2, SVEs with varying length and a height of 10 mm are sampled from a 50 × 50 mm field with a 12% volume fraction of soft inclusions. Due to an increased statistical scatter a total of 100 SVEs are sampled for a length of $L_\square = 0.5$. Twenty-five SVEs are sampled for each remaining length increment.

Figure 6.6 (left) shows the resulting axial stiffness for each SVE, as well as the average for each length under a state of pure elongation. The results are normalised with respect to the elongation stiffness of a homogeneous material, namely $\overline{EA} = 210 \times 10^4$ N. It is important to draw attention to the fact that as $L_\square \to 0$, the axial stiffness does in fact approach the Voigt bound as proven in Section 6.4.

The normalised bending stiffness for each SVE, under a state of pure bending is shown in Figure 6.6 (right). The results have again been normalised using the homogeneous bending stiffness, $\overline{EI} = 175 \times 10^5$ Nmm^2. Again, the results approach the Voigt bound proven in Section 6.4.2, as $L_\square \to 0$. In both of the cases, as the length of the SVE increases, the statistical scatter decreases, and results converge.

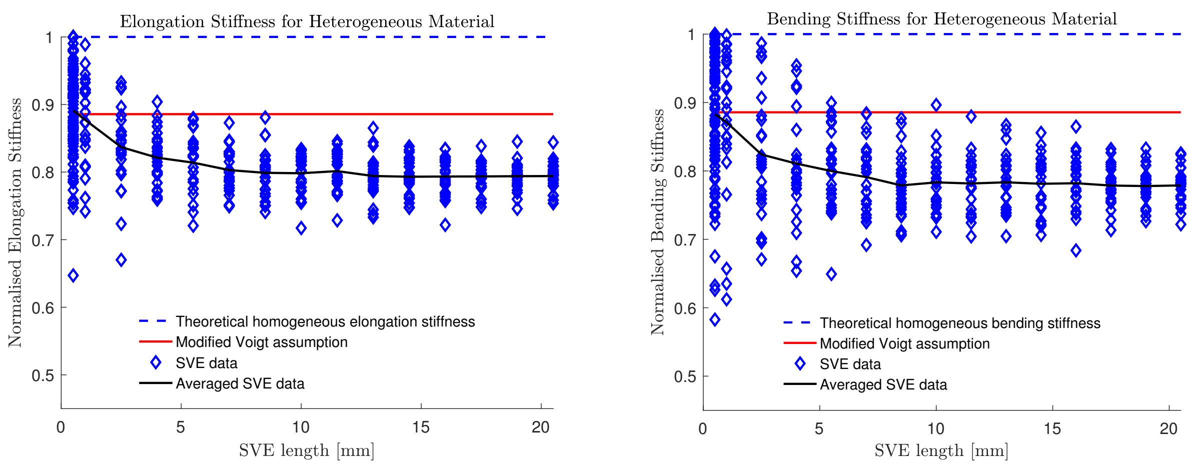

Figure 6.6: Normalised axial stiffness (left) and normalised bending stiffness (right) for SVEs of varying length. Prolongation and homogenisation method formulated using Euler-Bernoulli beam theory.

6.6 Validation

In order to verify the accuracy of the homogenised stiffness, three unique load cases are analysed, namely those introduced in Section 2.3. A total of 10 distinct beams, with a length of 50 mm, a height of 10 mm and a thickness of 1 mm are sampled from the field described in Section 5.2. An overkill finite element analysis is carried out on each. The resulting deformation field is averaged over the height at each longitudinal point. This results in Figure 6.7. It is clear that the deformation field varies significantly for each sample. Considering that the number of soft inclusions and their distribution is different for each specimen, this reaffirms that the variation in material substructure plays a large role in its response. In order to capture this diversity, the results of the ten beam specimens are averaged. This average, which is referred to as the overkill FEA average in Figure 6.7, is regarded as the true solution from this point forward.

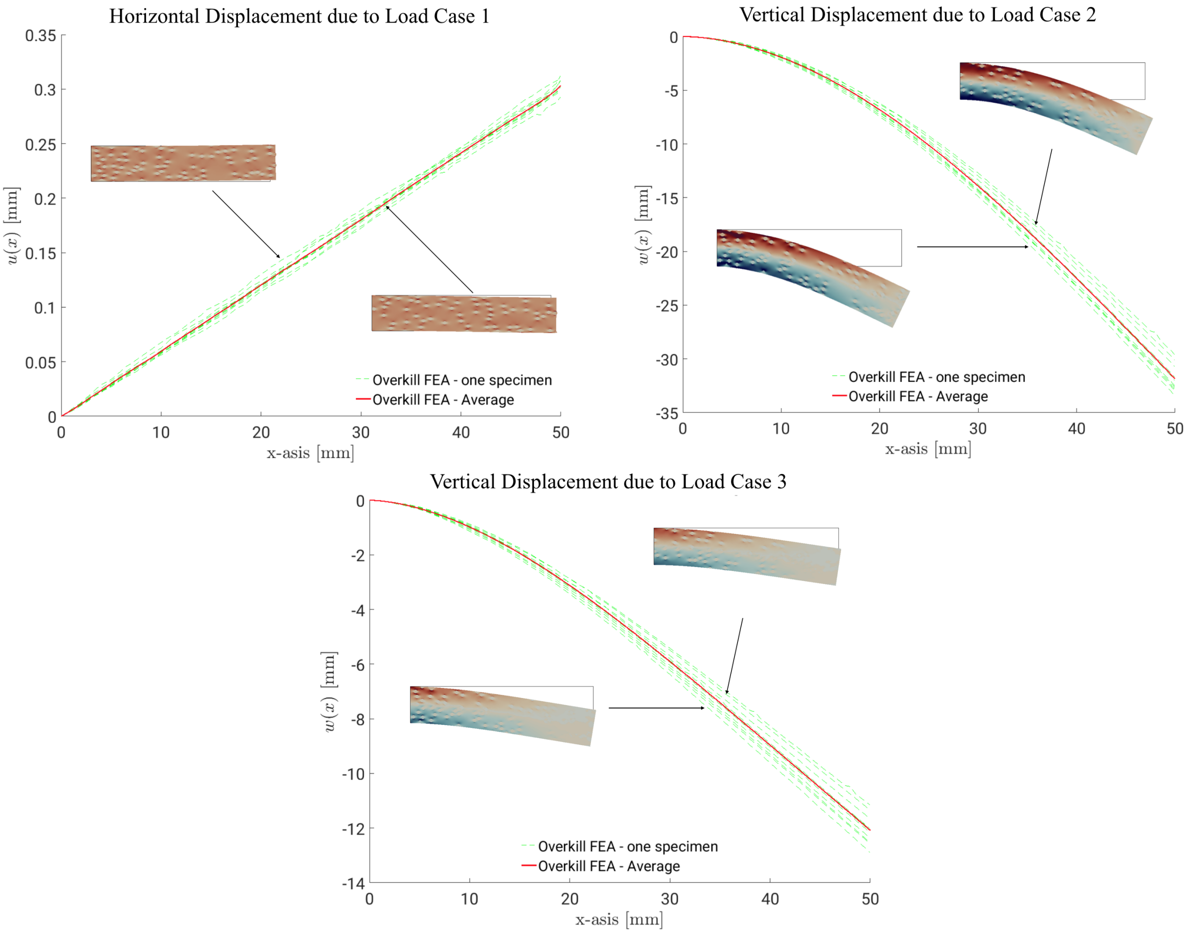

Figure 6.7: Resulting displacements and their average for elongation (top left), shearing (top right), and distributed loading (bottom). The deformations in the contour plots are magnified with a factor of 5 for elongation and 0.5 for the second and third load cases. The colour distribution of the contour plots indicates the axial stress magnitude.

The effective elongation and bending stiffness given by Figure 6.6, are used in the analytic Euler-Bernoulli beam expressions derived in Section 2.3. Recall that

$$\bar{u}(x) = \frac{1}{\overline{EA}}\left(10000 \cdot x\right) \text{ mm}$$
$$\bar{w}(x) = \frac{1}{\overline{EI}}\left(\frac{10000}{6}x^3 - \frac{500000}{2}x^2\right) \text{ mm}$$
$$\bar{w}(x) = \frac{1}{\overline{EI}}\left(-\frac{200}{24}x^4 + \frac{10000}{6}x^3 - \frac{250000}{2}x^2\right) \text{ mm}$$

for load cases one, two and three, respectively. Considering the above, the maximum tip displacement at $x =$ 50 mm, is computed. These results are normalised by, and compared to, the true solution for each load case. This is shown in Figure 6.8. The results confirm that the elongation and bending stiffness have converged as the SVE size increases. However, the response of the heterogeneous beam is underestimated when bending dominates its behaviour.

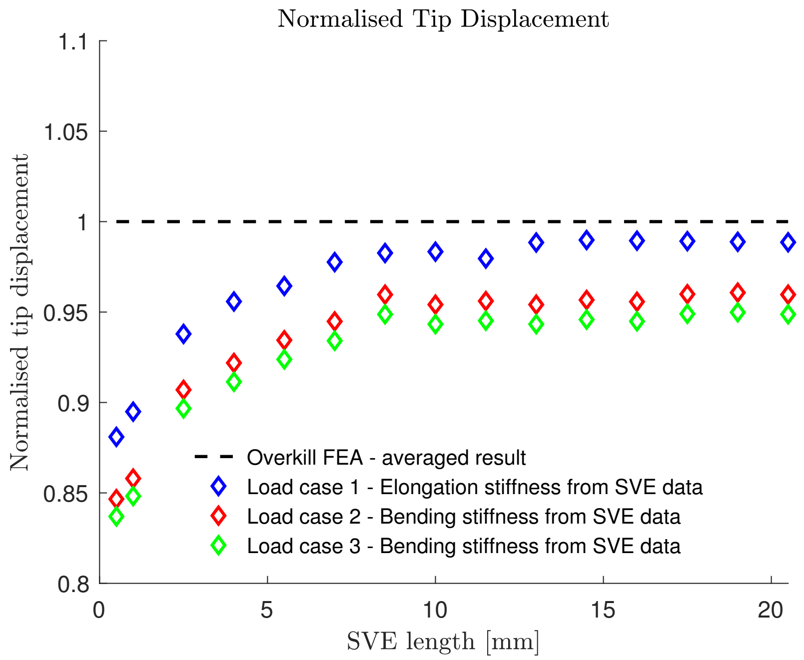

Figure 6.8: Normalised tip displacement for different SVE sizes and load cases. Prolongation and homogenisation method formulated using Euler-Bernoulli beam theory.

In order to further analyse the effectiveness of the proposed method, the full deformation behaviour of the beam is considered for stiffness values obtained for two individual SVE lengths. In the available literature, a square or cubic element is most commonly considered, although a justification as to why is not always apparent. For that reason, closer consideration is given to the stiffness values obtained for an SVE with a length of 10 mm, as well as for one with a length of 20.5 mm as it represents a converged solution. The entire deformation field for both lengths, is shown in Figure 6.9 for all three load cases. Again, it is clear that elongation is captured well while bending is not. The analytic results for the second and third load cases are simply too stiff. As previously discussed, Euler-Bernoulli beam theory is not capable of capturing shearing of the beam, which for stocky beams, can yield an overly stiff response. In fact, [11] states that Euler-Bernoulli beam theory is only satisfactory for beams that are more than five to ten times longer than they are high, since the shear strain is generally small in those cases. The considered beam in this analysis does not satisfy this requirement. It is clear that in order to obtain accurate results, incorporating shear behaviour, using Timoshenko beam theory is necessary.

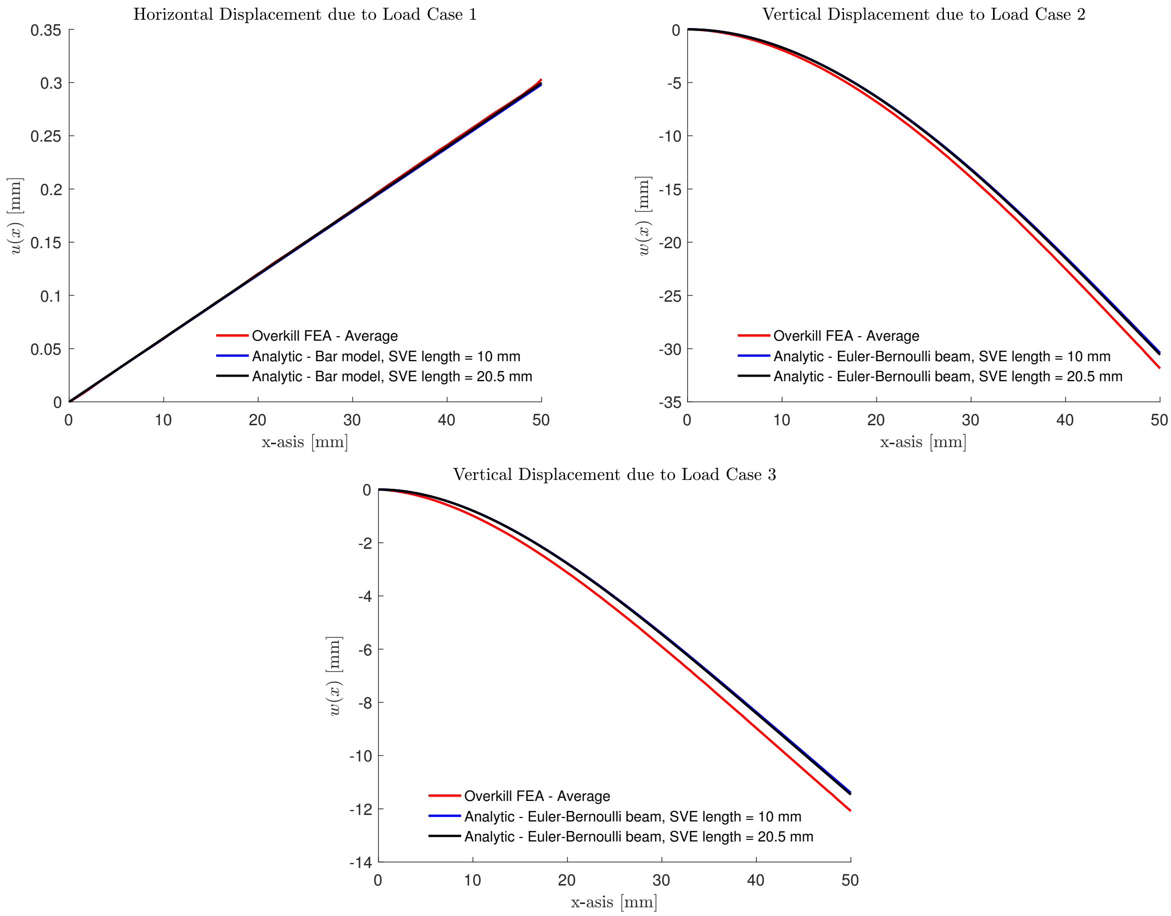

Figure 6.9: Comparison of beam deformation for considered load cases. The first load case (top left) is that of elongation wheres the second (top right) and third (bottom) are shear and distributed loading, respectively.

7 Computational Homogenisation Based on Timoshenko Beam Theory

7.1 Macroscale - Subscale Transition

In a similar manner to that done in Section 6, it is possible to prolong the macroscale elongation and curvature values to the subscale SVE using Dirichlet boundary conditions derived through the consideration of Timoshenko beam theory. However, in addition, it is now possible to prescribe shearing through $\bar{\gamma} = -\bar{\phi} + \frac{\partial \bar{w}}{\partial x}$.

The macroscale deformations are expressed on the SVE by considering first order Taylor expansions around $\bar{x}$, namely

$$u_x^M = \bar{u}^0(\bar{x}) - z\bar{\phi}(\bar{x}) + \frac{\partial \bar{u}^0(\bar{x})}{\partial x}\left[x - \bar{x}\right] - z\frac{\partial \bar{\phi}(\bar{x})}{\partial x}\left[x - \bar{x}\right] \tag{7.1}$$

and

$$u_z^M = \bar{w}(\bar{x}) + \frac{\partial \bar{w}(\bar{x})}{\partial x}\left[x - \bar{x}\right]. \tag{7.2}$$

By considering Equation (7.1) it is clear that the first term be may be disregarded as it will only yield a translation of the SVE. Equation (7.1 can therefore be simplified to

$$u_x^M = -z\bar{\phi}(\bar{x}) + \bar{\varepsilon}^0(\bar{x})\left[x - \bar{x}\right] - z\bar{\phi}'(\bar{x})\left[x - \bar{x}\right].$$

It is possible to prescribe both pure axial elongation, through $\bar{\varepsilon}^0$ and pure curvature through $\bar{\phi}'$. It is also possible to prescribe a combination of the two. This corresponds respectively to the Dirichlet boundary conditions given by

$$u_x^M = \begin{cases} \frac{\bar{\varepsilon}^0 L_\square}{2} & \text{on } \Gamma_R \\ -\frac{\bar{\varepsilon}^0 L_\square}{2} & \text{on } \Gamma_L \end{cases},$$

$$u_x^M = \begin{cases} -\frac{z\bar{\phi}' L_\square}{2} & \text{on } \Gamma_R \\ \frac{z\bar{\phi}' L_\square}{2} & \text{on } \Gamma_L \end{cases}$$

and

$$u_x^M = \begin{cases} \frac{\bar{\varepsilon}^0 L_\square}{2} - \frac{z\bar{\phi}' L_\square}{2} & \text{on } \Gamma_R \\ -\frac{\bar{\varepsilon}^0 L_\square}{2} + \frac{z\bar{\phi}' L_\square}{2} & \text{on } \Gamma_L \end{cases}.$$

All are identical to the boundary conditions prescribed using Euler-Bernoulli beam kinematics.

It is important to observe that in order to fully prescribe the shearing behaviour, namely $\bar{\gamma} = -\bar{\phi} + \frac{\partial \bar{w}}{\partial x}$, on the SVE, terms in both u_x^M and u_z^M are required. Horizontal shearing, illustrated in Figure 7.1, is prescribed using the Dirichlet boundary conditions given by

$$u_x^M = \begin{cases} -z\bar{\phi} & \text{on } \Gamma_R \\ -z\bar{\phi} & \text{on } \Gamma_L. \end{cases}$$

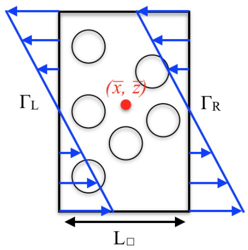

Figure 7.1: Horizontal shearing of the SVE.

The method in which the vertical displacement u_z^M is prescribed as a boundary condition, is again a point of discussion. Unlike the previous case, it is not sufficient to solely constrain the displacements in the centre of the SVE as it is necessary to consider $\frac{\partial \bar{w}}{\partial x}$. However, as discussed in Section 6.1, prescribing u_z^M as a strong Dirichlet boundary condition gives unphysical behaviour. Vertical shearing, illustrated in Figure 7.2, is therefore imposed using periodic boundary conditions, which express the variation of a specific value from one boundary to the other.

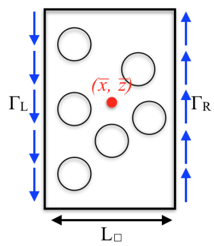

Figure 7.2: Vertical shearing of the SVE.

It is here, that the jump function $[\![\bullet]\!]$ is introduced. Namely,

$$[\![\bullet]\!] = \bullet\big|_{\Gamma_R} - \bullet\big|_{\Gamma_L}.$$

For simplicity this is denoted as

$$[\![\bullet]\!] = \bullet^+ - \bullet^-,$$

from this point forward. As an example, this means that the jump between two points shown in Figure 7.3, can be expressed as

$$
\begin{aligned}
[\![x]\!] &= x^+ - x^- \\
&= \frac{L_\square}{2} - \frac{-L_\square}{2} \\
&= L_\square .
\end{aligned}
$$

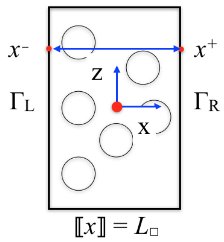

Figure 7.3: Example of the jump between two points on the left and right boundaries of an SVE.

Setting the variation $u_z^{S+} - u_z^{S-} = 0$, allows the aforementioned periodic boundary conditions to be expressed strongly as

$$u_z^+ - u_z^- = u_z^{M+} - u_z^{M-} = \left(\bar{w}(\bar{x}) + \bar{w}'(\bar{x})\frac{L_\square}{2}\right) - \left(\bar{w}(\bar{x}) + \bar{w}'(\bar{x})\frac{-L_\square}{2}\right) = \bar{w}'(\bar{x})L_\square .$$

Implementing the periodic boundary condition strongly however, proves difficult. In order to discretely relate each respective boundary point, a structured finite element mesh that is identical on both the right and left hand boundaries is required. This is not straightforward, especially in the case when inclusions exist on the boundaries. The vertical boundary condition is therefore considered in its weakest form

$$\int_{\Gamma_R} \delta\lambda [\![u_z]\!] \, \mathrm{d}\Gamma = \delta\lambda \bar{w}'(\bar{x}) Ł_\square h,$$

where $\delta\lambda \in \mathbb{R}$ is an arbitrary test function.

7.2 Boundary Value Problem Formulation

7.2.1 Strong Formulation

Considering an SVE occupying the domain $\Omega_\square$ with the boundaries Γ_L, Γ_R and Γ_h, as shown in Figure 6.3, the strong form is stated as

$$
\begin{aligned}
-\boldsymbol{\sigma} \cdot \boldsymbol{\nabla} &= \mathbf{0} \text{ in } \Omega_\square && (7.3)\\
\boldsymbol{t} &= \mathbf{0} \text{ on } \Gamma_h && (7.4)\\
u_x &= -z\bar{\phi}(\bar{x}) + \bar{\varepsilon}^0(\bar{x})\,[x - \bar{x}] - z\bar{\phi}'(\bar{x})\,[x - \bar{x}] \;\text{ on } \Gamma_L \text{ and } \Gamma_R && (7.5)\\
\int_{\Gamma_R} \delta\lambda [\![u_z]\!] \, \mathrm{d}\Gamma &= \delta\lambda \bar{w}'(\bar{x}) Ł_\square h && (7.6)\\
u_z &= 0 \text{ at } (x, z) = (\bar{x}, \bar{z}), && (7.7)
\end{aligned}
$$

neglecting the body force.

7.2.2 Weak Formulation

The weak formulation of Equation (7.3) is given by finding $\boldsymbol{u} \in \mathbb{U}_\square$ such that

$$\int_{\Omega_\square} \boldsymbol{\sigma} : [\delta\boldsymbol{u} \otimes \boldsymbol{\nabla}] \, \mathrm{d}\Omega - \int_{\Gamma_L \cup \Gamma_R} \boldsymbol{t} \cdot \delta\boldsymbol{u} \, \mathrm{d}\Gamma = 0 \quad \forall \, \delta\boldsymbol{u} \in \mathbb{U}_\square^0, \tag{7.8}$$

as shown in Section 5.1.2. In order to impose the weakly periodic constraint related to vertical shearing, i.e. Equation (7.6), a constant Lagrange multiplier, $\lambda \in \mathbb{R}$ is introduced such that

$$\underline{\boldsymbol{t}}\big|_{\Gamma_R} = \underline{\boldsymbol{t}}^+ = \boldsymbol{t}_\lambda^+ = \begin{bmatrix} 0 \\ \lambda \end{bmatrix}.$$

The second term in Equation (7.8) can then be expressed as

$$\begin{aligned}
\int_{\Gamma_L \cup \Gamma_R} \boldsymbol{t}_\lambda \cdot \delta \boldsymbol{u} \; \mathrm{d}\Gamma &= \int_{\Gamma_R} \boldsymbol{t}_\lambda^+ \cdot \delta \boldsymbol{u}^+ \; \mathrm{d}\Gamma + \int_{\Gamma_L} \boldsymbol{t}_\lambda^- \cdot \delta \boldsymbol{u}^- \; \mathrm{d}\Gamma \\
&= \int_{\Gamma_R} \boldsymbol{t}_\lambda^+ \cdot \delta \boldsymbol{u}^+ \; \mathrm{d}\Gamma + \int_{\Gamma_R} \boldsymbol{t}_\lambda^- \cdot \delta \boldsymbol{u}^- \; \mathrm{d}\Gamma.
\end{aligned}$$

When considering the behaviour of the SVE under prescribed vertical shearing it is noted that the deformation of the left and right hand boundaries is mirrored with respect to the $z-$axis. Anti-periodicity of the traction, i.e $\boldsymbol{t}_\lambda^+ = -\boldsymbol{t}_\lambda^-$ is therefore enforced. This gives

$$\begin{aligned}
\int_{\Gamma_R} \boldsymbol{t}_\lambda^+ \cdot \delta \boldsymbol{u}^+ \; \mathrm{d}\Gamma + \int_{\Gamma_R} \boldsymbol{t}_\lambda^- \cdot \delta \boldsymbol{u}^- \; \mathrm{d}\Gamma &= \int_{\Gamma_R} \boldsymbol{t}_\lambda^+ \cdot \delta \boldsymbol{u}^+ \; \mathrm{d}\Gamma - \int_{\Gamma_R} \boldsymbol{t}_\lambda^+ \cdot \delta \boldsymbol{u}^- \; \mathrm{d}\Gamma \\
&= \int_{\Gamma_R} \boldsymbol{t}_\lambda \cdot \left(\delta \boldsymbol{u}^+ - \delta \boldsymbol{u}^-\right) \; \mathrm{d}\Gamma \\
&= \int_{\Gamma_R} \boldsymbol{t}_\lambda \cdot [\![\delta \boldsymbol{u}]\!] \; \mathrm{d}\Gamma.
\end{aligned}$$

Introducing $\delta \underline{\boldsymbol{t}}^+ = \delta \underline{\boldsymbol{t}}_\lambda^+ = \begin{bmatrix} 0 & \delta\lambda \end{bmatrix}^T \in \mathbb{T}_\square^0$, allows Equation (7.6) to be expressed as

$$\int_{\Gamma_R} \delta \boldsymbol{t}_\lambda \cdot [\![\boldsymbol{u}]\!] \; \mathrm{d}\Gamma = \delta\lambda \frac{\partial \bar{w}}{\partial x} L_\square h \quad \forall \; \delta \boldsymbol{t}_\lambda \in \mathbb{T}_\square^0.$$

The boundary value problem may therefore be summarised in abstract form, as finding $\boldsymbol{u} \in \mathbb{U}_\square$ and $\boldsymbol{t}_\lambda \in \mathbb{T}_\square$ such that

$$a_\square(\boldsymbol{u}, \delta \boldsymbol{u}) - d_\square(\boldsymbol{t}_\lambda, \delta \boldsymbol{u}) = 0 \quad \forall \; \delta \boldsymbol{u} \in \mathbb{U}_\square^0 \tag{7.9}$$

$$-d_\square(\delta \boldsymbol{t}_\lambda, \boldsymbol{u}) = -\delta\lambda \frac{\partial \bar{w}}{\partial x} L_\square h \quad \forall \; \delta \boldsymbol{t}_\lambda \in \mathbb{T}_\square^0, \tag{7.10}$$

where

$$a_\square(\boldsymbol{u}, \delta \boldsymbol{u}) = \int_{\Omega_\square} \boldsymbol{\sigma} : [\delta \boldsymbol{u} \otimes \boldsymbol{\nabla}] \; \mathrm{d}\Omega, \tag{7.11}$$

$$d_\square(\boldsymbol{t}_\lambda, \delta \boldsymbol{u}) = \int_{\Gamma_R} \boldsymbol{t}_\lambda \cdot [\![\delta \boldsymbol{u}]\!] \; \mathrm{d}\Gamma, \tag{7.12}$$

$$d_\square(\delta \boldsymbol{t}_\lambda, \boldsymbol{u}) = \int_{\Gamma_R} \delta \boldsymbol{t}_\lambda \cdot [\![\boldsymbol{u}]\!] \; \mathrm{d}\Gamma \tag{7.13}$$

and

$$\begin{aligned}
\mathbb{U}_\square &= \left\{ \boldsymbol{u} : \int_\Omega |\boldsymbol{u}|^2 + |\boldsymbol{u} \otimes \boldsymbol{\nabla}|^2 \; \mathrm{d}\Omega < \infty, u_x = -z\bar{\phi} + \bar{\varepsilon}^0 \left[x - \bar{x}\right] - z\bar{\phi}' \left[x - \bar{x}\right] \text{ on } \Gamma_L \text{ and } \Gamma_R, \; u_z = 0 \text{ at } (\bar{x}, \bar{z}) \right\}, \\
\mathbb{U}_\square^0 &= \left\{ \delta \boldsymbol{u} : \int_\Omega |\delta \boldsymbol{u}|^2 + |\delta \boldsymbol{u} \otimes \boldsymbol{\nabla}|^2 \; \mathrm{d}\Omega < \infty, \delta u_x = 0 \text{ on } \Gamma_L \text{ and } \Gamma_R, \; \delta u_z = 0 \text{ at } (\bar{x}, \bar{z}) \right\}, \\
\mathbb{T}_\square &= \left\{ \boldsymbol{t} : t_x = 0 \text{ and } t_z = \lambda \in \mathbb{R} \right\}, \\
\mathbb{T}_\square^0 &= \left\{ \delta \boldsymbol{t} : \delta t_x = 0 \text{ and } \delta t_z = \delta\lambda \in \mathbb{R} \right\}.
\end{aligned}$$

7.2.3 Finite Element Formulation

In a similar fashion to Section 5.1.3, the displacements approximations $\underline{\boldsymbol{u}} \approx \underline{\boldsymbol{u}}_h = \underline{\boldsymbol{N}}_u \underline{\boldsymbol{a}}_u$, and $\delta\underline{\boldsymbol{u}} \approx \delta\underline{\boldsymbol{u}}_h = \underline{\boldsymbol{N}}_u \delta\underline{\boldsymbol{a}}_u$ are introduced into Equation (7.11) which results in

$$\int_{\Omega_\square} \boldsymbol{\sigma} : [\delta \boldsymbol{u} \otimes \boldsymbol{\nabla}] \, \mathrm{d}\Omega \approx \delta\underline{\boldsymbol{a}}_u^T \int_{\Omega_\square} \underline{\boldsymbol{B}}_u^T \underline{\boldsymbol{D}} \underline{\boldsymbol{B}}_u \, \mathrm{d}\Omega \underline{\boldsymbol{a}}_u = \delta\underline{\boldsymbol{a}}_u^T \underline{\boldsymbol{K}}_{uu} \underline{\boldsymbol{a}}_u.$$

Equation (7.12) can be decomposed such that

$$\begin{aligned} \int_{\Gamma_R} [\![\delta\underline{\boldsymbol{u}}]\!]^T \underline{\boldsymbol{t}}_\lambda^+ \, \mathrm{d}\Gamma &= \int_{\Gamma_R} \delta\underline{\boldsymbol{u}}^{T+} \underline{\boldsymbol{t}}_\lambda^+ \, \mathrm{d}\Gamma - \int_{\Gamma_R} \delta\underline{\boldsymbol{u}}^{T-} \underline{\boldsymbol{t}}_\lambda^+ \, \mathrm{d}\Gamma \\ &= \int_{\Gamma_R} \delta\underline{\boldsymbol{u}}^{T+} \underline{\boldsymbol{t}}_\lambda^+ \, \mathrm{d}\Gamma - \int_{\Gamma_L} \delta\underline{\boldsymbol{u}}^{T-} \underline{\boldsymbol{t}}_\lambda^+ \, \mathrm{d}\Gamma. \end{aligned}$$

Approximating the traction as

$$\underline{\boldsymbol{t}}_\lambda^+ = \underline{\boldsymbol{N}}_\lambda \underline{\boldsymbol{a}}_\lambda \quad \text{with} \quad \underline{\boldsymbol{N}}_\lambda = \begin{bmatrix} 0 & 1 \end{bmatrix} \text{ and } \underline{\boldsymbol{a}}_\lambda = \begin{bmatrix} 0 \\ \lambda \end{bmatrix},$$

results in the following finite element formulation

$$\int_{\Gamma_R} \delta\underline{\boldsymbol{u}}^{T+} \underline{\boldsymbol{t}}_\lambda^+ \, \mathrm{d}\Gamma - \int_{\Gamma_L} \delta\underline{\boldsymbol{u}}^{T-} \underline{\boldsymbol{t}}_\lambda^+ \, \mathrm{d}\Gamma \approx \delta\underline{\boldsymbol{a}}_u^T \left[\int_{\Gamma_R} \underline{\boldsymbol{N}}_u^T \underline{\boldsymbol{N}}_\lambda \, \mathrm{d}\Gamma - \int_{\Gamma_L} \underline{\boldsymbol{N}}_u^T \underline{\boldsymbol{N}}_\lambda \, \mathrm{d}\Gamma \right] \underline{\boldsymbol{a}}_\lambda = \delta\underline{\boldsymbol{a}}_u^T \underline{\boldsymbol{K}}_{u\lambda} \underline{\boldsymbol{a}}_\lambda.$$

Similarly, Equation (7.13) may be reformulated such that

$$\begin{aligned} \int_{\Gamma_R} \delta\underline{\boldsymbol{t}}_\lambda^T \cdot [\![\underline{\boldsymbol{u}}]\!] \, \mathrm{d}\Gamma &= \int_{\Gamma_R} \delta\underline{\boldsymbol{t}}_\lambda^{T+} \cdot \underline{\boldsymbol{u}}^+ \, \mathrm{d}\Gamma - \int_{\Gamma_R} \delta\underline{\boldsymbol{t}}_\lambda^{T+} \cdot \underline{\boldsymbol{u}}^- \, \mathrm{d}\Gamma \\ &= \int_{\Gamma_R} \delta\underline{\boldsymbol{t}}_\lambda^{T+} \cdot \underline{\boldsymbol{u}}^+ \, \mathrm{d}\Gamma - \int_{\Gamma_L} \delta\underline{\boldsymbol{t}}_\lambda^{T+} \cdot \underline{\boldsymbol{u}}^- \, \mathrm{d}\Gamma, \end{aligned}$$

which may be expressed as

$$\int_{\Gamma_R} \delta\underline{\boldsymbol{t}}_\lambda^{T+} \cdot \underline{\boldsymbol{u}}^+ \, \mathrm{d}\Gamma - \int_{\Gamma_L} \delta\underline{\boldsymbol{t}}_\lambda^{T+} \cdot \underline{\boldsymbol{u}}^- \, \mathrm{d}\Gamma \approx \delta\underline{\boldsymbol{a}}_\lambda^T \left[\int_{\Gamma_R} \underline{\boldsymbol{N}}_\lambda^T \underline{\boldsymbol{N}}_u \, \mathrm{d}\Gamma - \int_{\Gamma_L} \underline{\boldsymbol{N}}_\lambda^T \underline{\boldsymbol{N}}_u \, \mathrm{d}\Gamma \right] \underline{\boldsymbol{a}}_u = \delta\underline{\boldsymbol{a}}_\lambda^T \underline{\boldsymbol{K}}_{\lambda u} \underline{\boldsymbol{a}}_u$$

by introducing

$$\delta\underline{\boldsymbol{t}}_\lambda^+ = \underline{\boldsymbol{N}}_\lambda \delta\underline{\boldsymbol{a}}_\lambda = \begin{bmatrix} 0 & 1 \end{bmatrix} \begin{bmatrix} 0 \\ \delta\lambda \end{bmatrix}.$$

Finally, given that

$$-\delta\lambda \frac{\partial \bar{w}}{\partial x} L_\square h = \begin{bmatrix} 0 & \delta\lambda \end{bmatrix} \begin{bmatrix} 0 \\ -\frac{\partial \bar{w}}{\partial x} L_\square \cdot h \end{bmatrix} = \delta\underline{\boldsymbol{a}}_\lambda^T \underline{\boldsymbol{f}}_\lambda,$$

the weak formulation given in (7.9) and (7.10) is equivalent to the following symmetric system of equations:

$$\begin{bmatrix} \underline{\boldsymbol{K}}_{uu} & -\underline{\boldsymbol{K}}_{u\lambda} \\ -\underline{\boldsymbol{K}}_{\lambda u} & 0 \end{bmatrix} \begin{bmatrix} \underline{\boldsymbol{a}}_u \\ \underline{\boldsymbol{a}}_\lambda \end{bmatrix} = \begin{bmatrix} \underline{\boldsymbol{0}} \\ \underline{\boldsymbol{f}}_\lambda \end{bmatrix}.$$

7.3 Subscale - Macroscale Transition

From the solution of the boundary value problem, the stress field over an SVE is known, some examples of which are shown in Figure 7.4 under either pure elongation, curvature or shear. The effective stiffness may then be determined by first computing

$$\bar{M} = \frac{1}{L_\square} \int_{\Omega_\square} \sigma_{xx} \cdot z \, \mathrm{d}\Omega_\square$$

$$\bar{N} = \frac{1}{L_\square} \int_{\Omega_\square} \sigma_{xx} \, \mathrm{d}\Omega_\square$$

and

$$\bar{V} = \frac{1}{L_\square} \int_{\Omega_\square} \tau_{xz} \, \mathrm{d}\Omega_\square.$$

Based on linearity, it is then possible, for the given values of $\bar{\varepsilon}^0$, $\bar{\kappa}$ and $\bar{\gamma}$ to find the effective axial, bending and shear stiffness as

$$\overline{EA} = \frac{\bar{N}}{\bar{\varepsilon}^0} \text{ for } \bar{\kappa} = \bar{\gamma} = 0$$
$$\overline{EI} = -\frac{\bar{M}}{\bar{\kappa}} \text{ for } \bar{\varepsilon}^0 = \bar{\gamma} = 0$$
$$\overline{K_s GA} = \frac{\bar{V}}{\bar{\gamma}} \text{ for } \bar{\varepsilon}^0 = \bar{\kappa} = 0.$$

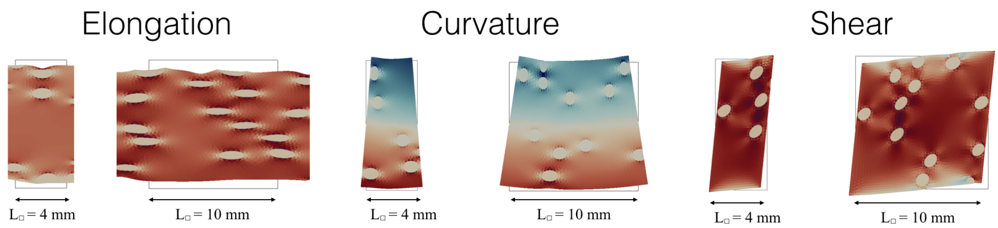

Figure 7.4: Axial stress field under pure elongation (left) and pure curvature (middle). Shear stress distribution under pure shearing (right).

7.4 Bounding Effective Stiffness as $L_\square \to 0$

In order to determine if the obtained stiffness results are reasonable for the considered heterogeneous material, a number of bounds are considered. The Voigt assumption, assumes that the strain field is constant within the studied domain. This assumption typically results in an upper estimation of the homogenised stiffness. In this particular case, axial elongation and curvature are both prescribed through strong Dirichlet boundary conditions. As is shown in Section 6.4, the axial and bending stiffness should therefore approach the Voigt bound as $L_\square$. However, determining a bound for the shear stiffness is not as straightforward. Recall that the macroscale shear strain is imposed onto an SVE through both Dirichlet and weakly periodic boundary conditions. The Voigt assumption, for an SVE with a height of 10 mm and thickness of 1 mm sampled from the domain introduced in Section 5.2, gives a homogenised shear stiffness of

$$\overline{K_s G_V A} = 59.52 \cdot 10^3 \text{ N}.$$

It is important to note that this value cannot truly be considered a bound, but simply a value with which to quantify the results.

7.5 Results

7.5.1 Homogeneous SVE

In order to determine the legitimacy of results predicted by the model developed in Sections 7.1 through 7.3, homogeneous SVEs with a height of 10 mm, a Young's modulus of $E = 210$ GPa, a shear modulus of $G = 80.8$ GPa and varying length are analysed. Figure 7.5, demonstrates that the methods proposed in Sections 7.1 through 7.3 are able to accurately capture the axial and bending stiffness of a homogeneous SVE without any inherent dependence on length. However the same cannot be said when capturing the shear response, which is compared to the theoretical uncorrected and corrected shear stiffness given by $\overline{GA} = 80.8 \times 10^4$ N and $\overline{K_s GA} = 67.3 \times 10^4$ N respectively. Figure 7.6 demonstrates a clear pathological size dependence. There is a continuous degradation in geometric behaviour, leading to increasingly unphysical and soft results.

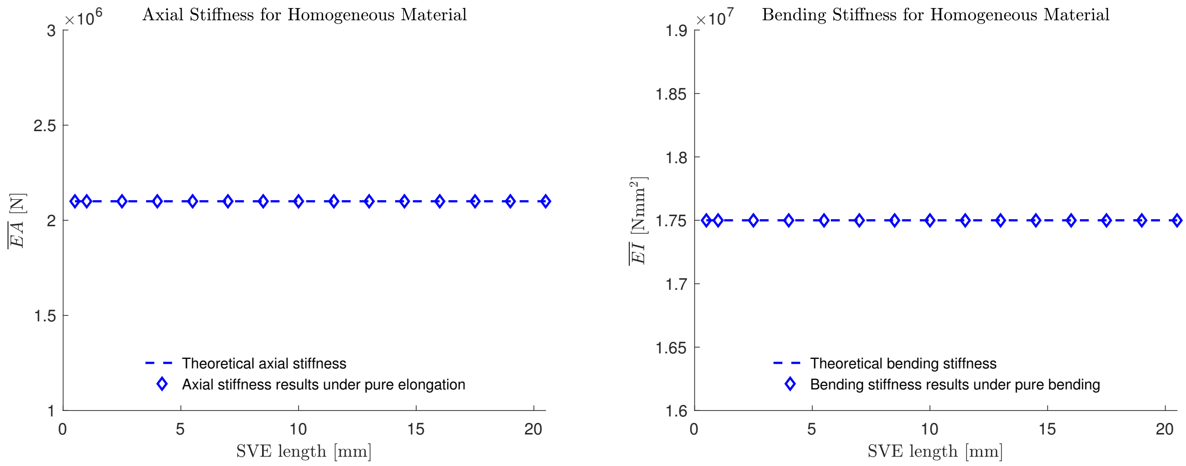

Figure 7.5: Resulting effective axial (left) and bending (right) stiffness considering homogeneous SVEs of varying length. Prolongation and homogenisation method formulated using Timoshenko beam theory.

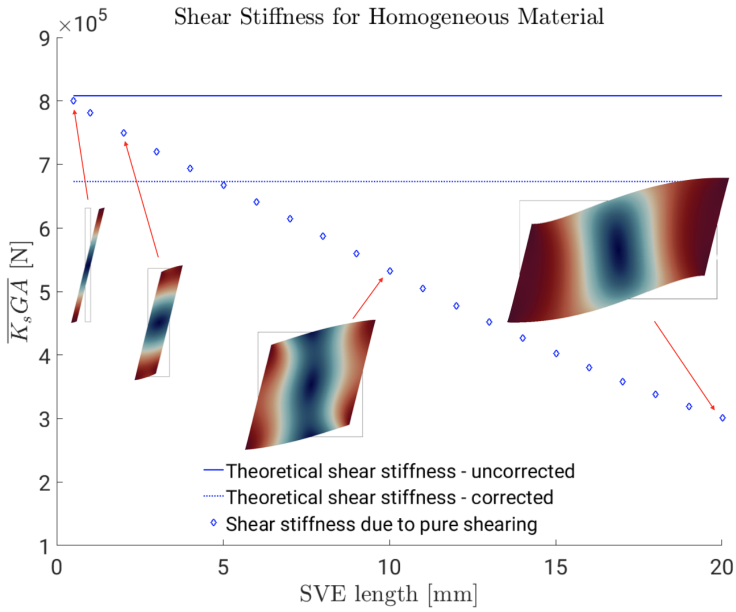

Figure 7.6: Shear stiffness for homogeneous SVEs of varying length The colour map indicates the deformation magnitude. Deformations magnified by factor of 5. Prolongation and homogenisation method formulated using Timoshenko beam theory.

7.5.2 Heterogeneous SVE

As previously discussed, the considered prolongation and homogenisation method is analysed by considering heterogeneous SVEs of varying length sampled from the domain introduced in Section 5.2. The resulting elongation stiffness for the heterogeneous SVEs are shown in Figure 7.7 (left), and are normalised with respect to the theoretical homogeneous elongation stiffness, namely $\overline{EA} = 210 \times 10^4$ N.

Initial results prove positive. For increasingly small SVEs, the stiffness approaches the Voigt bound as proven in Section 6.4. Furthermore, the results show a converged stiffness with increasing SVE size. It is possible to draw the same positive conclusions from Figure 7.7 (right), which illustrates the resulting bending stiffness, normalised by the theoretical homogeneous bending stiffness $\overline{EI} = 163 \times 10^4$ Nmm^2. However, see Figure 7.8, it is again clear that this method is not capable of accurately capturing the shear behaviour. As with the homogeneous case, the response continually softens for SVEs of increasing length.

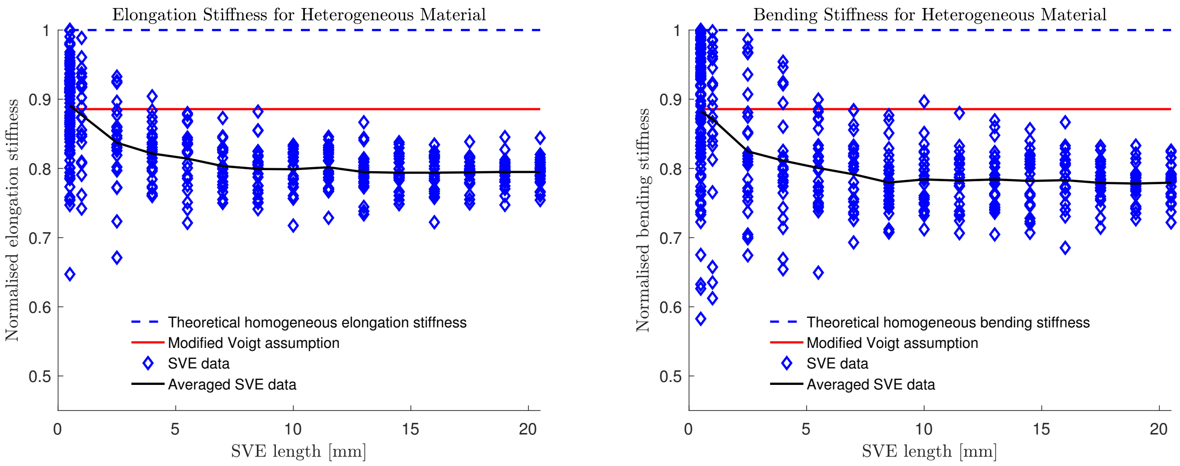

Figure 7.7: Normalised elongation stiffness (left) and normalised bending stiffness (right) for heterogeneous SVEs of varying length. Prolongation and homogenisation method formulated using Timoshenko beam theory.

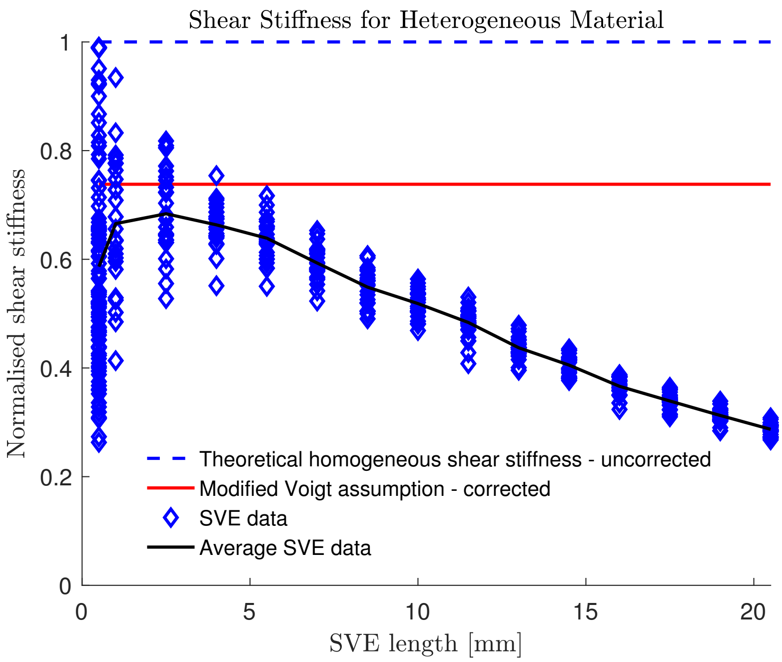

Figure 7.8: Normalised shear stiffness for heterogeneous SVEs of varying length. Prolongation and homogenisation method formulated using Timoshenko beam theory.

7.6 Validation

In order to validate the obtained axial, bending and shear stiffness, the maximum tip displacement for each load case, presented in Section 2.5 is considered. The analytic solutions found from

$$
\begin{aligned}
\bar{u}(x) &= \frac{1}{\overline{EA}}\left(10000 \cdot x\right) \ \text{mm} \\
\bar{w}(x) &= -\frac{10000}{\overline{K_s GA}}x + \frac{1}{\overline{EI}}\left(\frac{10000}{6}x^3 - \frac{500000}{2}x^2\right) \ \text{mm}
\end{aligned}
$$

and

$$\bar{w}(x) = -\frac{1}{\overline{K_s GA}}\left(\frac{-200}{2}x^2 + 10000x\right) + \frac{1}{\overline{EI}}\left(-\frac{200}{24}x^4 + \frac{10000}{6}x^3 - \frac{250000}{2}x^2\right) \text{ mm}$$

for the first, second and third load case respectively, are normalised by and plotted against the true solution found from the DNS analysis. This is shown in Figure 7.9. Again, it is clear that the considered method is capable of capturing the axial stiffness, and providing satisfactory analytic results. However, for the second and third load case, the accuracy of the analytic solution worsens as the shear response degrades for longer SVEs.

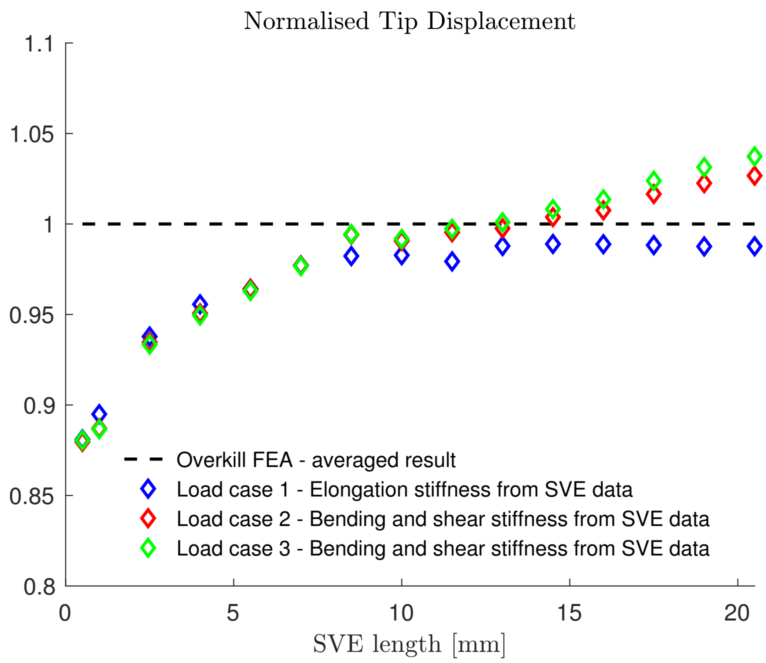

Figure 7.9: Normalised tip displacement for different SVE sizes and load cases. Prolongation and homogenisation method formulated using Timoshenko beam theory.

Figure 7.10 compares the full deformation behaviour of the analytic solution with that from the DNS analysis. Stiffness values are taken for both a square SVE as well as an SVE of length $L_\square = 20.5$ mm. The former appears extremely accurate in capturing the bending behaviour of the beam, but as one would expect, the results become overly soft for a long SVE.

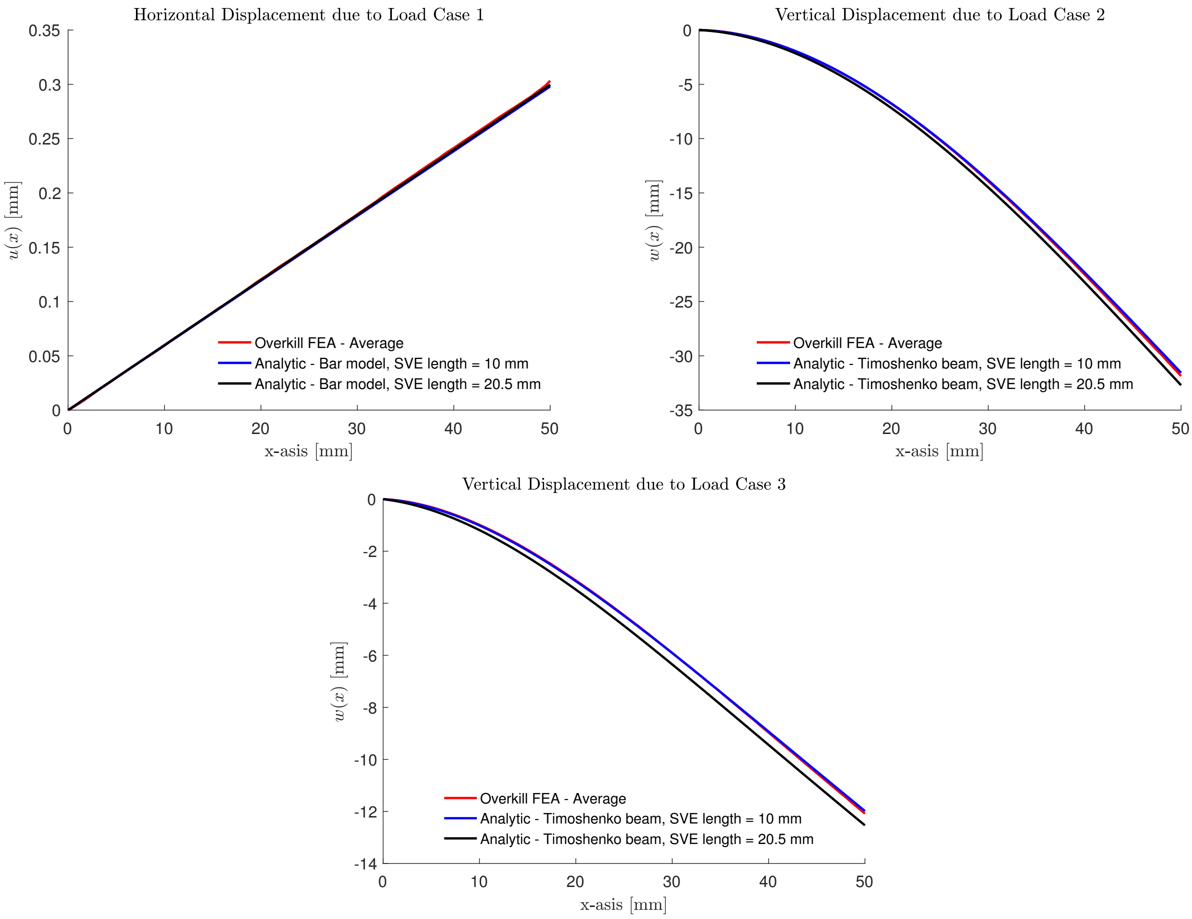

Figure 7.10: Deformation of the beam due to the first (top left), second (top right) and third (bottom) load cases. Prolongation and homogenisation method formulated using Timoshenko beam theory.

8 Computational Homogenisation Based on a Method Presented by Geers et al.

It is clear from Section 7, that capturing the appropriate shear response, for increasingly large SVEs, is not straightforward. Further consideration is therefore given to a computational homogenisation method for structured thin sheets, introduced by Geers et al. [7]. The method gives some discussion to the treatment of the shear response, and when used to model a bending beam, it provides what the authors describe as "remarkable results." The computational homogenisation method introduced in [7], is formulated assuming macroscale shell kinematics. Note however, that the constraints and assumptions introduced in this section have been reduced to reflect the considered macroscale beam problem.

8.1 Macroscale - Subscale Transition

As previously discussed, the displacement field on the SVE is composed of a macroscale deformation field $\boldsymbol{u}^M$ and a subscale fluctuation field $\boldsymbol{u}^S$ such that

$$\boldsymbol{u} = \boldsymbol{u}^M + \boldsymbol{u}^S = \begin{bmatrix} u_x^M \\ u_z^M \end{bmatrix} + \begin{bmatrix} u_x^S \\ u_z^S \end{bmatrix}.$$

This is used to impose boundary conditions on the SVE. The macroscale deformation field is formulated using Timoshenko beam theory, where

$$\boldsymbol{u}^M = \begin{bmatrix} u_x^M \\ u_z^M \end{bmatrix} = \begin{bmatrix} \bar{u}^0 - z\bar{\phi} + \bar{\varepsilon}^0[x - \bar{x}] - z\bar{\phi}'[x - \bar{x}] \\ \bar{w} + \bar{w}'[x - \bar{x}] \end{bmatrix}.$$

When the kinematic assumptions are reduced from that of a shell to a beam, the first constraints introduced by Geers et al, are given by

$$[\![u_x^S]\!] = 0, \tag{8.1}$$

i.e. strong periodicity of u_x^S, and

$$\int_{\Gamma_R} [\![u_z^S]\!] \, \mathrm{d}\Gamma = 0, \tag{8.2}$$

i.e. weak periodicity of u_z^S. This ensures that the macroscopic deformation gradient is equal to the volume average of the subscale deformation gradient.

As stated by Geers et al. and as previously shown, the boundary conditions relating to the out of plane shear are more delicate. In this case a weak constraint is enforced on the left and right hand boundaries such that the average subscale shear is equal to the macroscopic value. Namely,

$$\int_{\Gamma_R} z\cdot < u_x^S > \, \mathrm{d}\Gamma = 0 \text{ , where } < \bullet >= \frac{1}{2}\left(\bullet^+ + \bullet^-\right). \tag{8.3}$$

Implementing Equation (8.1) strongly however, proves difficult as it requires identical meshes on the left and right hand boundaries. This is not straightforward, especially in the case when inclusions exist on the boundaries. This boundary condition will therefore be considered in its weakest form in this work:

$$\int_{\Gamma_R} \delta\lambda_x [\![u_x^S]\!] \, \mathrm{d}\Gamma = 0. \tag{8.4}$$

The remaining two constraints, namely those in Equations (8.2) and (8.3) will also be considered in their weakest form:

$$\int_{\Gamma_R} \delta\lambda_z [\![u_z^S]\!] \, \mathrm{d}\Gamma = 0 \tag{8.5}$$

$$\int_{\Gamma_R} \delta\mu_x \cdot z\cdot < u_x^S > \, \mathrm{d}\Gamma = 0. \tag{8.6}$$

The Lagrange multipliers λ_z, and μ_x are both chosen as constants. Their test functions, $\delta\lambda_z$, and $\delta\mu_x$, therefore are as well. However, in order to allow for the consideration of all relevant macroscale measures, the Lagrange multiplier λ_x must be linear. It is composed of a constant term $\bar{\lambda}_x$ and a linear term $\hat{\lambda}_x \cdot z$ such that

$$\lambda_x = \bar{\lambda}_x + \hat{\lambda}_x \cdot z.$$

The related test function is therefore

$$\delta\lambda_x = \delta\bar{\lambda}_x + \delta\hat{\lambda}_x \cdot z.$$

It is also important to note that in [7], the kinematics are expressed in a co-rotational coordinate system. This allows $\epsilon_{zx} = \partial\bar{w}/\partial x = 0$, and as such it is possible to express the macroscale shear strictly in the horizontal direction. This is illustrated in Figure 8.1. In the current simplification to a beam model, a co-rotational coordinate system is not used. Shearing is applied to the SVE in both the vertical and horizontal directions.

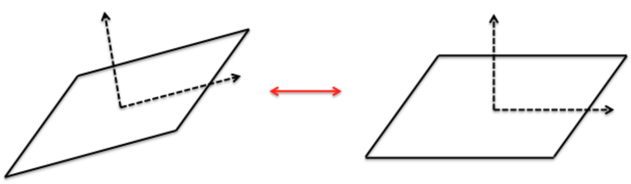

Figure 8.1: Illustration of shear behaviour.

With consideration to Equations (8.4), (8.5) and (8.6), the macroscale measures such as curvature, shearing and elongation are applied to the SVE taking into account that

$$\int_{\Gamma_R} \delta\lambda_x [\![u_x]\!] \, \mathrm{d}\Gamma = \int_{\Gamma_R} \delta\lambda_x [\![u_x^M]\!] \, \mathrm{d}\Gamma + \int_{\Gamma_R} \delta\lambda_x [\![u_x^S]\!] \, \mathrm{d}\Gamma = \int_{\Gamma_R} \delta\lambda_x [\![u_x^M]\!] \, \mathrm{d}\Gamma = \delta\bar{\lambda}_x \bar{\varepsilon}^0 L_\square h - \delta\hat{\lambda}_x \bar{\phi}' L_\square \frac{h^3}{12},$$
$$\int_{\Gamma_R} \delta\lambda_z [\![u_z]\!] \, \mathrm{d}\Gamma = \int_{\Gamma_R} \delta\lambda_x [\![u_z^M]\!] \, \mathrm{d}\Gamma + \int_{\Gamma_R} \delta\lambda_x [\![u_z^S]\!] \, \mathrm{d}\Gamma = \int_{\Gamma_R} \delta\lambda_x [\![u_z^M]\!] \, \mathrm{d}\Gamma = \delta\lambda_z \bar{w}' L_\square h$$

and

$$\int_{\Gamma_R} \delta\mu_x \cdot z \cdot < u_x > \; \mathrm{d}\Gamma = \int_{\Gamma_R} \delta\mu_x \cdot z \cdot < u_x^M > \; \mathrm{d}\Gamma + \int_{\Gamma_R} \delta\mu_x \cdot z \cdot < u_x^S > \; \mathrm{d}\Gamma = \int_{\Gamma_R} \delta\mu_x \cdot z \cdot < u_x^M > \; \mathrm{d}\Gamma = \delta\mu_x \bar{\phi} \frac{h^3}{12}.$$

8.2 Boundary Value Problem Formulation

8.2.1 Strong Formulation

The equivalent strong form of the boundary value problem presented in [7], in which the kinematics have been reduced from a shell to a beam, is given by

$$-\boldsymbol{\sigma} \cdot \boldsymbol{\nabla} = \mathbf{0} \text{ in } \Omega_\square \tag{8.7}$$
$$\boldsymbol{t} = \mathbf{0} \text{ on } \Gamma_h \tag{8.8}$$
$$u_z = 0 \text{ at } (x, z) = (\bar{x}, \bar{z}) \tag{8.9}$$
$$\int_{\Gamma_R} \delta\lambda_x [\![u_x]\!] \, \mathrm{d}\Gamma = \delta\bar{\lambda}_x \bar{\varepsilon}^0 L_\square h - \delta\hat{\lambda}_x \bar{\phi}' L_\square \frac{h^3}{12} \quad \forall \, \delta\bar{\lambda}_x, \delta\hat{\lambda}_x \in \mathbb{R} \tag{8.10}$$
$$\int_{\Gamma_R} \delta\lambda_z [\![u_z]\!] \, \mathrm{d}\Gamma = \delta\lambda_z \bar{w}' L_\square h \quad \forall \, \delta\lambda_z \in \mathbb{R} \tag{8.11}$$
$$\int_{\Gamma_R} \delta\mu_x \cdot z \cdot < u_x > \; \mathrm{d}\Gamma = -\delta\mu_x \bar{\phi} \frac{h^3}{12} \quad \forall \, \delta\mu_x \in \mathbb{R} \tag{8.12}$$

Note that the Lagrange multipliers λ_x and λ_z, and their respective test functions are responsible for prescribing the macroscale curvature, axial elongation, and vertical shearing to the SVE. In these cases, the behaviour on one side of the SVE is opposite to the behaviour on the other. However, the Lagrange multiplier μ_x and its respective test function, impose horizontal shearing on the SVE. The behaviour of which is the same on each side.

8.2.2 Weak Formulation

The weak form of the equilibrium equation given in Equation (8.7) can be expressed as

$$\int_{\Omega_\square} \boldsymbol{\sigma} : [\delta \boldsymbol{u} \otimes \boldsymbol{\nabla}] \; \mathrm{d}\Omega - \int_{\Gamma_L \cup \Gamma_R} \boldsymbol{t} \cdot \delta \boldsymbol{u} \; \mathrm{d}\Gamma = 0 \quad \forall \, \delta \boldsymbol{u} \in \mathbb{U}_\square^0. \tag{8.13}$$

In order to ensure that the stiffness matrix of the final FE problem formulation is symmetric, the traction vector must be divided into sections that correspond to the Lagrange multipliers $\bar{\lambda}_x, \hat{\lambda}_x, \lambda_z \in \mathbb{R}$ and $\mu_x \in \mathbb{R}$ respectively. Therefore

$$\mathbf{t}^+ = \boldsymbol{t}_\lambda^+ + \boldsymbol{t}_\mu^+ = \begin{bmatrix} \bar{\lambda}_x + \hat{\lambda}_x \cdot z \\ \lambda_z \end{bmatrix} + \begin{bmatrix} \mu_x \cdot z \\ 0 \end{bmatrix}.$$

The second term in Equation (8.13), may be formulated such that

$$\begin{aligned} \int_{\Gamma_R \cup \Gamma_L} \boldsymbol{t} \cdot \delta \boldsymbol{u} \; \mathrm{d}\Gamma &= \int_{\Gamma_R \cup \Gamma_L} \boldsymbol{t}_\lambda \cdot \delta \boldsymbol{u} \; \mathrm{d}\Gamma + \int_{\Gamma_R \cup \Gamma_L} \boldsymbol{t}_\mu \cdot \delta \boldsymbol{u} \; \mathrm{d}\Gamma \\ &= \int_{\Gamma_R} \boldsymbol{t}_\lambda^+ \cdot \delta \boldsymbol{u}^+ \; \mathrm{d}\Gamma + \int_{\Gamma_L} \boldsymbol{t}_\lambda^- \cdot \delta \boldsymbol{u}^- \; \mathrm{d}\Gamma + \int_{\Gamma_R} \boldsymbol{t}_\mu^+ \cdot \delta \boldsymbol{u}^+ \; \mathrm{d}\Gamma + \int_{\Gamma_L} \boldsymbol{t}_\mu^- \cdot \delta \boldsymbol{u}^- \; \mathrm{d}\Gamma. \end{aligned}$$

Enforcing anti-periodicity of $\boldsymbol{t}_\lambda$, i.e. $\boldsymbol{t}_\lambda^+ = -\boldsymbol{t}_\lambda^-$ and periodicity of $\boldsymbol{t}_\mu$, i.e. $\boldsymbol{t}_\mu^+ = \boldsymbol{t}_\mu^-$, in turn gives

$$= \int_{\Gamma_R} \boldsymbol{t}_\lambda \cdot \delta\boldsymbol{u}^+ \ \mathrm{d}\Gamma - \int_{\Gamma_R} \boldsymbol{t}_\lambda \cdot \delta\boldsymbol{u}^- \ \mathrm{d}\Gamma + \int_{\Gamma_R} \boldsymbol{t}_\mu \cdot \delta\boldsymbol{u}^+ \ \mathrm{d}\Gamma + \int_{\Gamma_R} \boldsymbol{t}_\mu \cdot \delta\boldsymbol{u}^- \ \mathrm{d}\Gamma \tag{8.14}$$

$$= \int_{\Gamma_R} \mathbf{t}_\lambda [\![\delta\boldsymbol{u}]\!] \ \mathrm{d}\Gamma + 2\int_{\Gamma_R} \mathbf{t}_\mu < \delta\boldsymbol{u} > \ \mathrm{d}\Gamma. \tag{8.15}$$

The boundary conditions given in Equations (8.10) and (8.11) may be combined in order to correspond to the first term in Equation (8.15). This gives that

$$\int_{\Gamma_R} \delta\underline{\boldsymbol{t}}_\lambda^T [\![\underline{\boldsymbol{u}}]\!] \ \mathrm{d}\Gamma = \begin{bmatrix} \delta\bar{\lambda}_x & \delta\hat{\lambda}_x & \delta\lambda_z \end{bmatrix} \begin{bmatrix} \bar{\epsilon}^0 L_\square h \\ -\bar{\phi}' L_\square \frac{h^3}{12} \\ \bar{w}' L_\square h \end{bmatrix},$$

where

$$\delta\underline{\boldsymbol{t}}_\lambda^+ = \begin{bmatrix} \delta\bar{\lambda}_x + \delta\hat{\lambda}_x \cdot z \\ \delta\lambda_z \end{bmatrix} \text{ and } \underline{\boldsymbol{u}} = \begin{bmatrix} u_x^M \\ u_z^M \end{bmatrix}.$$

Similarly

$$2\int_{\Gamma_R} \delta\underline{\boldsymbol{t}}_\mu^T < \underline{\boldsymbol{u}} > \ \mathrm{d}\Gamma = \begin{bmatrix} \delta\mu_x & 0 \end{bmatrix} \begin{bmatrix} -\bar{\phi}\frac{h^3}{6} \\ 0 \end{bmatrix}$$

where

$$\delta\underline{\boldsymbol{t}}_\mu^+ = \begin{bmatrix} \delta\mu_x \\ 0 \end{bmatrix}.$$

The weak formulation of the problem is then stated as finding $\boldsymbol{u} \in \mathbb{U}$, and $\bar{\lambda}_x, \hat{\lambda}_x, \lambda_z, \mu_x \in \mathbb{R}$ such that

$$a_\square(\boldsymbol{u}, \delta\boldsymbol{u}) - d_\square(\boldsymbol{t}_\lambda, \delta\boldsymbol{u}) - 2e_\square(\boldsymbol{t}_\mu, \delta\boldsymbol{u}) = 0 \quad \forall\ \delta\boldsymbol{u} \in \mathbb{U}_\square^0 \tag{8.16}$$

$$-d_\square(\delta\boldsymbol{t}_\lambda, \boldsymbol{u}) = \begin{bmatrix} \delta\bar{\lambda}_x & \delta\hat{\lambda}_x & \delta\lambda_z \end{bmatrix} \begin{bmatrix} -\bar{\epsilon}^0 L_\square h \\ \bar{\phi}' L_\square \frac{h^3}{12} \\ -\bar{w}' L_\square h \end{bmatrix} \quad \forall\ \delta\bar{\lambda}_x, \delta\hat{\lambda}_x, \delta\lambda_z \in \mathbb{R} \tag{8.17}$$

$$-2e_\square(\delta\boldsymbol{t}_\mu, \boldsymbol{u}) = \delta\mu_x \bar{\phi}\frac{h^3}{6} \quad \forall\ \delta\mu_x \in \mathbb{R}. \tag{8.18}$$

where

$$\begin{aligned}
a_\square(\boldsymbol{u}, \delta\boldsymbol{u}) &= \int_{\Omega_\square} \boldsymbol{\sigma} : [\delta\boldsymbol{u} \otimes \boldsymbol{\nabla}] \ \mathrm{d}\Omega \\
d_\square(\delta\boldsymbol{t}_\lambda, \mathbf{u}) &= \int_{\Gamma_R} \delta\boldsymbol{t}_\lambda \cdot [\![\boldsymbol{u}]\!] \ \mathrm{d}\Gamma \\
d_\square(\boldsymbol{t}_\lambda, \delta\boldsymbol{u}) &= \int_{\Gamma_R} \boldsymbol{t}_\lambda \cdot [\![\delta\boldsymbol{u}]\!] \ \mathrm{d}\Gamma \\
e_\square(\delta\boldsymbol{t}_\mu, \boldsymbol{u}) &= 2\int_{\Gamma_R} \delta\boldsymbol{t}_\mu < \boldsymbol{u} > \ \mathrm{d}\Gamma \\
e_\square(\boldsymbol{t}_\mu, \delta\boldsymbol{u}) &= 2\int_{\Gamma_R} \boldsymbol{t}_\mu < \delta\boldsymbol{u} > \ \mathrm{d}\Gamma
\end{aligned}$$

and

$$\begin{aligned}
\mathbb{U}_\square &= \left\{ \boldsymbol{u} : \int_\Omega |\boldsymbol{u}|^2 + |\boldsymbol{u} \otimes \boldsymbol{\nabla}|^2 \ \mathrm{d}\Omega < \infty,\ u_z = 0 \text{ at } (x,z) = (\bar{x}, \bar{z}) \right\} \\
\mathbb{U}_\square^0 &= \left\{ \delta\boldsymbol{u} : \int_\Omega |\delta\boldsymbol{u}|^2 + |\delta\boldsymbol{u} \otimes \boldsymbol{\nabla}|^2 \ \mathrm{d}\Omega < \infty \right\}
\end{aligned}$$

8.2.3 Finite Element Formulation

Introducing the finite element approximations

$$\underline{\boldsymbol{u}} \approx \underline{\boldsymbol{u}}_h = \underline{\boldsymbol{N}}_u \underline{\boldsymbol{a}}_u \text{ and } \delta\underline{\boldsymbol{u}} \approx \delta\underline{\boldsymbol{u}}_h = \underline{\boldsymbol{N}}_u \delta\underline{\boldsymbol{a}}_u$$

into the first term of Equation (8.16), gives

$$\int_{\Omega_\square} \boldsymbol{\sigma} : [\delta\boldsymbol{u} \otimes \boldsymbol{\nabla}] \ \mathrm{d}\Omega \approx \delta\underline{\boldsymbol{a}}_u^T \int_{\Omega_\square} \underline{\boldsymbol{B}}_u^T \underline{\boldsymbol{D}} \underline{\boldsymbol{B}}_u \ \mathrm{d}\Omega \ \underline{\boldsymbol{a}}_u = \delta\underline{\boldsymbol{a}}_u^T \underline{\boldsymbol{K}}_{uu} \underline{\boldsymbol{a}}_u.$$

In a similar fashion, introducing the finite element approximations given by

$$\underline{\boldsymbol{t}}_\lambda^+ = \begin{bmatrix} \bar{\lambda}_x + \hat{\lambda}_x \cdot z \\ \lambda_z \end{bmatrix} = \begin{bmatrix} 1 & z & 0 \\ 0 & 0 & 1 \end{bmatrix} \begin{bmatrix} \bar{\lambda}_x \\ \hat{\lambda}_x \\ \lambda_z \end{bmatrix} = \underline{\boldsymbol{N}}_\lambda \underline{\boldsymbol{a}}_\lambda \text{ and } \underline{\boldsymbol{t}}_\mu^+ = \begin{bmatrix} \mu_x \cdot z \\ 0 \end{bmatrix} = \begin{bmatrix} z & 0 \end{bmatrix} \begin{bmatrix} \mu \\ 0 \end{bmatrix} = \underline{\boldsymbol{N}}_\mu \underline{\boldsymbol{a}}_\mu$$

allows the remaining terms in Equation (8.16) to be expressed as

$$\begin{aligned}
\int_{\Gamma_R} [\![\delta\underline{\boldsymbol{u}}]\!]^T \underline{\boldsymbol{t}}_\lambda \ \mathrm{d}\Gamma &= \int_{\Gamma_R} \delta\underline{\boldsymbol{u}}^{T+} \underline{\boldsymbol{t}}_\lambda^+ \ \mathrm{d}\Gamma - \int_{\Gamma_R} \delta\underline{\boldsymbol{u}}^{T-} \underline{\boldsymbol{t}}_\lambda^+ \ \mathrm{d}\Gamma \\
&= \int_{\Gamma_R} \delta\underline{\boldsymbol{u}}^{T+} \underline{\boldsymbol{t}}_\lambda^+ \ \mathrm{d}\Gamma - \int_{\Gamma_L} \delta\underline{\boldsymbol{u}}^{T-} \underline{\boldsymbol{t}}_\lambda^+ \ \mathrm{d}\Gamma \\
&= \delta\underline{\boldsymbol{a}}_u^T \left(\int_{\Gamma_R} \underline{\boldsymbol{N}}_u^T \underline{\boldsymbol{N}}_\lambda \ \mathrm{d}\Gamma - \int_{\Gamma_L} \underline{\boldsymbol{N}}_u^T \underline{\boldsymbol{N}}_\lambda \ \mathrm{d}\Gamma \right) \underline{\boldsymbol{a}}_\lambda \\
&= \delta\underline{\boldsymbol{a}}_u^T \left(\underline{\boldsymbol{K}}_{u\lambda}^+ - \underline{\boldsymbol{K}}_{u\lambda}^- \right) \underline{\boldsymbol{a}}_\lambda \\
&= \delta\underline{\boldsymbol{a}}_u^T \underline{\boldsymbol{K}}_{u\lambda} \underline{\boldsymbol{a}}_\lambda
\end{aligned}$$

and

$$\begin{aligned}
2\int_{\Gamma_R} < \delta\boldsymbol{u} > \underline{\boldsymbol{t}}_\mu^T \ \mathrm{d}\Gamma &= 2\left(\frac{1}{2} \int_{\Gamma_R} \delta\underline{\boldsymbol{u}}^+ \underline{\boldsymbol{t}}_\mu^+ \ \mathrm{d}\Gamma + \frac{1}{2} \int_{\Gamma_R} \delta\underline{\boldsymbol{u}}^- \underline{\boldsymbol{t}}_\mu^+ \ \mathrm{d}\Gamma \right) \\
&= \int_{\Gamma_R} \delta\underline{\boldsymbol{u}}^+ \underline{\boldsymbol{t}}_\mu^+ \ \mathrm{d}\Gamma + \int_{\Gamma_L} \delta\underline{\boldsymbol{u}}^- \underline{\boldsymbol{t}}_\mu^+ \ \mathrm{d}\Gamma \\
&= \delta\underline{\boldsymbol{a}}_u^T \left(\int_{\Gamma_R} \underline{\boldsymbol{N}}_u^T \underline{\boldsymbol{N}}_\mu \ \mathrm{d}\Gamma + \int_{\Gamma_L} \underline{\boldsymbol{N}}_u^T \underline{\boldsymbol{N}}_\mu \ \mathrm{d}\Gamma \right) \underline{\boldsymbol{a}}_\mu \\
&= \delta\underline{\boldsymbol{a}}_u^T \left(\underline{\boldsymbol{K}}_{u\mu}^+ + \underline{\boldsymbol{K}}_{u\mu}^- \right) \underline{\boldsymbol{a}}_\mu \\
&= \delta\underline{\boldsymbol{a}}_u^T \underline{\boldsymbol{K}}_{u\mu} \underline{\boldsymbol{a}}_\mu
\end{aligned}$$

respectively.

The additional constraints given in Equations (8.17) and (8.18), may in turn be formulated as

$$\int_{\Gamma_R} \delta\underline{\boldsymbol{t}}_\lambda^T [\![\underline{\boldsymbol{u}}]\!] \ \mathrm{d}\Gamma = \delta\underline{\boldsymbol{a}}_\lambda \underline{\boldsymbol{K}}_{\lambda u} \underline{\boldsymbol{a}}_u$$

$$\int_{\Gamma_R} \delta\underline{\boldsymbol{t}}_\mu^T < \underline{\boldsymbol{u}} > \ \mathrm{d}\Gamma = \delta\underline{\boldsymbol{a}}_\lambda \underline{\boldsymbol{K}}_{\mu u} \underline{\boldsymbol{a}}_u$$

by introducing

$$\delta\underline{\boldsymbol{t}}_\lambda = \begin{bmatrix} 1 & z & 0 \\ 0 & 0 & 1 \end{bmatrix} \begin{bmatrix} \delta\bar{\lambda}_x \\ \delta\hat{\lambda}_x \\ \delta\lambda_z \end{bmatrix} = \underline{\boldsymbol{N}}_\lambda \delta\underline{\boldsymbol{a}}_\lambda \text{ and } \delta\underline{\boldsymbol{t}}_\mu = \begin{bmatrix} z & 0 \end{bmatrix} \begin{bmatrix} \delta\mu_x \\ 0 \end{bmatrix} = \underline{\boldsymbol{N}}_\mu \delta\underline{\boldsymbol{a}}_\mu.$$

The final set of equations, is therefore stated as

$$\begin{bmatrix} \underline{\boldsymbol{K}}_{uu} & -\underline{\boldsymbol{K}}_{u\lambda} & -\underline{\boldsymbol{K}}_{u\mu} \\ -\underline{\boldsymbol{K}}_{\lambda u} & 0 & 0 \\ -\underline{\boldsymbol{K}}_{\mu u} & 0 & 0 \end{bmatrix} \begin{bmatrix} \underline{\boldsymbol{a}}_u \\ \underline{\boldsymbol{a}}_\lambda \\ \underline{\boldsymbol{a}}_\mu \end{bmatrix} = \begin{bmatrix} \underline{\boldsymbol{0}} \\ \underline{\boldsymbol{f}}_\lambda \\ \underline{\boldsymbol{f}}_\mu \end{bmatrix}.$$

where

$$\underline{\boldsymbol{a}}_\lambda = \begin{bmatrix} \bar{\lambda}_x \\ \hat{\lambda}_x \\ \lambda_z \end{bmatrix}, \ \underline{\boldsymbol{a}}_\mu = \begin{bmatrix} \mu_x \\ 0 \end{bmatrix}, \ \underline{\boldsymbol{f}}_\lambda = \begin{bmatrix} -\bar{\varepsilon}^0 L_\square h \\ \bar{\phi}' L_\square \\ -\bar{w}' L_h \frac{h^3}{12} \end{bmatrix}, \ \underline{\boldsymbol{f}}_\mu = \begin{bmatrix} \bar{\phi}\frac{h^3}{6} \\ 0 \end{bmatrix}, \bar{\boldsymbol{K}}_{u\lambda} = \bar{\boldsymbol{K}}_{\lambda u}^T \text{ and } \bar{\boldsymbol{K}}_{\mu u} = \bar{\boldsymbol{K}}_{u\mu}^T.$$

8.3 Subscale - Macroscale Transition

From the solution to the subscale boundary value problem, the effective bending, axial and shear stiffness is computed by first determining

$$\bar{M} = \frac{1}{|L_\square|}\int_{\Omega_\square} (\sigma_{xx}\cdot z + \tau_{xz}\cdot x)\ \mathrm{d}\Omega$$
$$\bar{N} = \frac{1}{|L_\square|}\int_{\Omega_\square} \sigma_{xx}\ \mathrm{d}\Omega$$

and

$$\bar{V} = \frac{1}{|L_\square|}\int_{\Omega_\square} \tau_{xz}\ \mathrm{d}\Omega,$$

as stated in [7]. It is then possible, for given values of $\bar{\phi}'$, $\bar{\varepsilon}^0$ and $\bar{\gamma}$ to find

$$\overline{EA} = \frac{\bar{N}}{\bar{\varepsilon}^0} \text{ for } \bar{\kappa} = \bar{\gamma} = 0$$
$$\overline{EI} = -\frac{\bar{M}}{\bar{\kappa}} \text{ for } \bar{\varepsilon}^0 = \bar{\gamma} = 0$$
$$\overline{K_s GA} = \frac{\bar{V}}{\bar{\gamma}} \text{ for } \bar{\varepsilon}^0 = \bar{\kappa} = 0.$$

8.4 Results

8.4.1 Homogeneous SVE

It is again clear, see Figure 8.2, that the prolongation and homogenisation methods discussed in Sections 8.1 through 8.3 are able to accurately capture the axial and bending response for a homogeneous SVEs of varying size. The same however, can not be said when it comes to the behaviour under shearing. The obtained shear stiffness for heterogeneous SVEs of varying size is shown in Figure 8.3. The results still show a large dependence on SVE size, and as with the previous method, an overly soft response for increasing long SVEs.

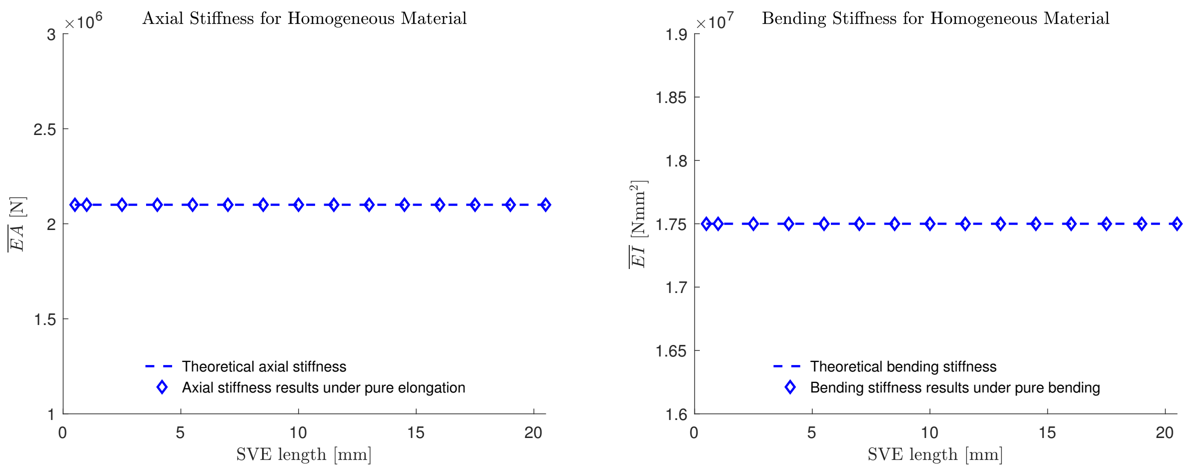

Figure 8.2: Resulting effective axial (left) and bending (right) stiffness considering homogeneous SVEs. Prolongation and homogenisation method formulated based on a method presented by Geers et al.

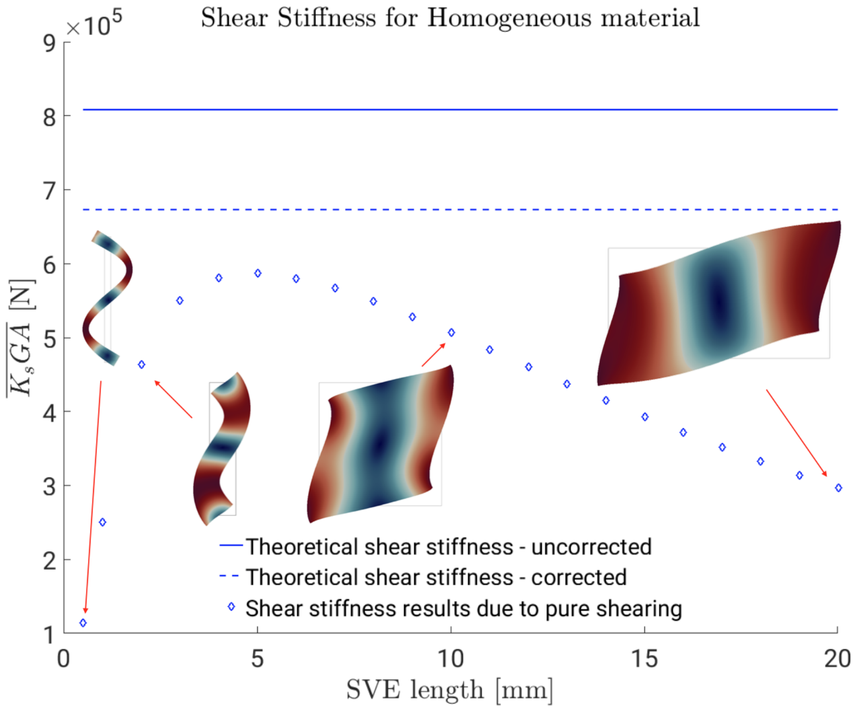

Figure 8.3: Shear stiffness for homogeneous SVEs of varying length. The colour map indicates the deformation magnitude. Deformations magnified by factor of 5. Prolongation and homogenisation method formulated based on a method presented by Geers et al.

8.4.2 Heterogeneous SVE

Given the choice of weak boundary constraints, it is expected that axial and bending stiffness results for heterogeneous SVEs should converge from below. This is confirmed in Figure 8.4, which shows the axial and bending stiffness results for heterogeneous SVEs of varying length. Again, the obtained axial and bending stiffness results are positive. In Figure 8.5 the shear stiffness for heterogeneous SVEs of varying length is plotted. It is clear that this method is not capable of capturing the shear response.

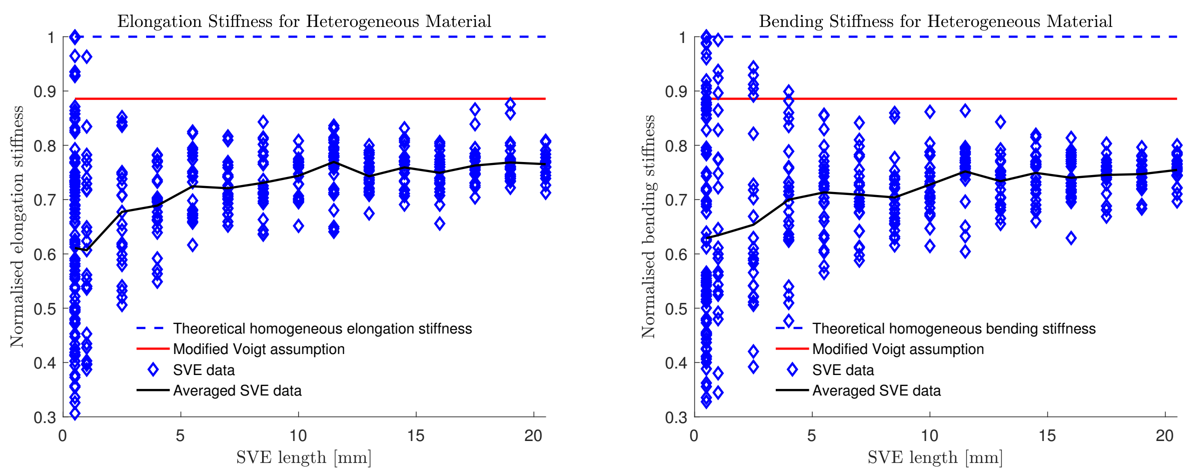

Figure 8.4: Normalised elongation (left) and bending stiffness (right) for heterogeneous SVE's of varying length. Prolongation and homogenisation method formulated based on a method presented by Geers et al.

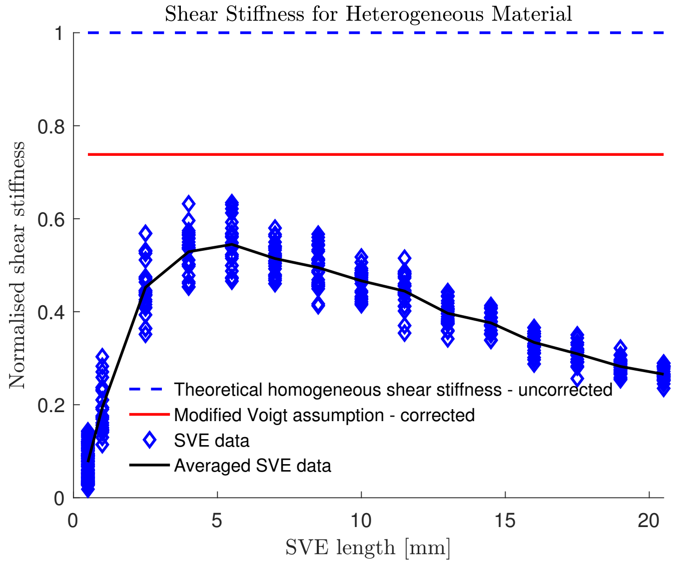

Figure 8.5: Normalised shear stiffness for heterogeneous SVE's of varying length. Prolongation and homogenisation method formulated based on a method presented by Geers et al.

8.5 Validation

Comparing the maximum tip displacement obtained analytically through Equations (2.19), (2.20) and (2.21), with the results found through DNS, gives Figure 8.6. The axial stiffness results are able to represent the true behaviour of the first load case in a satisfactory manner. In comparison however, it is still apparent that the degradation in shear stiffness makes capturing the bending behaviour of the beam, for the second and third load case, difficult. The full deformation results, in which the stiffness values are taken for a square SVE and one with a length of 20.5 mm, are shown in Figure 8.6.

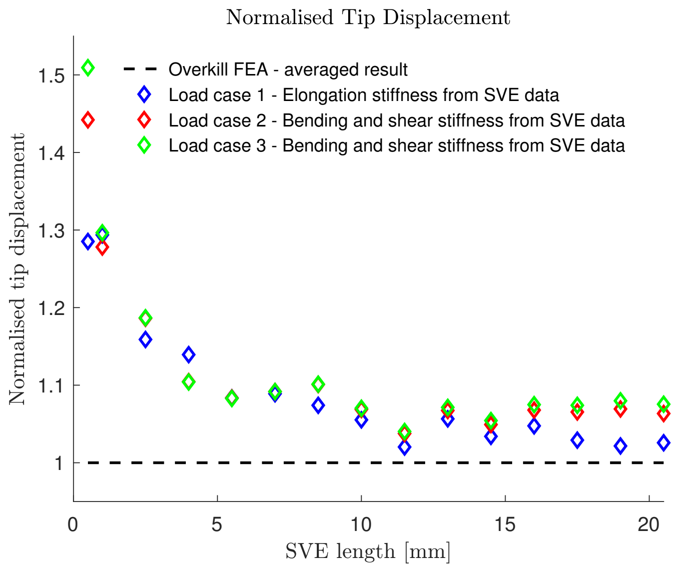

Figure 8.6: Normalised tip displacement for different SVE sizes and load cases. Prolongation and homogenisation method formulated based on a method presented by Geers et al.

As previously mentioned, Geers et al. appear to obtain promising results when using this prolongation and homogenisation technique on square SVE's to model beam bending. Specifically they implement a full FE^2 procedure on a cantilever beam with a point load at its extremity. However, it is clear from Figure 8.7 that in this case, the same cannot be said. The results are simply too soft. It is important to note however, that Geers et al. analyse a beam that is 25 times longer than it is high, which is perhaps a poor choice. Recall that [11] states that shear strain is generally small for beams that have a length-to-height ratio greater than 5-10. It is more than likely, for the beam chosen by Geers et al., that modelling any shear behaviour is completely unnecessary. The degradation in shear stiffness will have an essentially unnoticeable influence on their results.

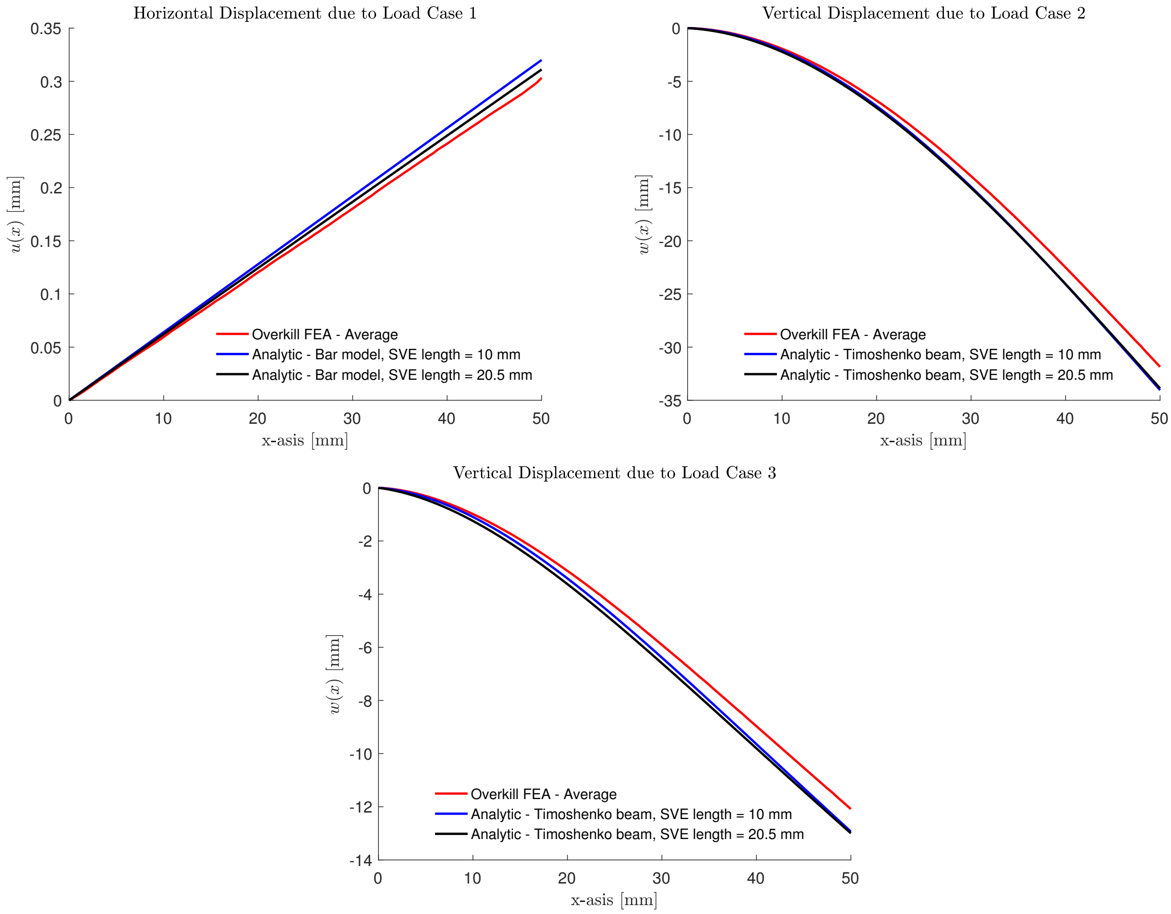

Figure 8.7: Deformation of the beam due to the first (top left), second (top right) and third (bottom) load cases. Prolongation and homogenisation method formulated based on a method presented by Geers et al.

9 Variationally Consistent Numerical Homogenisation

So far, the proposed prolongation and homogenisation methods have been unable to capture the shear response in a satisfying manner. Apart from that, the foundation of these methods lies on predefined kinematic and equilibrium assumptions. A method that has not yet been considered is Variationally Consistent Homogenisation (VCH). VCH, introduced in [13], [14] and [15], presents a systematic way with which to formulate the macroscale and subscale problems, starting from the field equations of a fully resolved model. The prolongation and homogenisation conditions are a direct consequence of splitting the resolved model into a smooth and fluctuating part. For more details and discussion pertaining to the considered VCH framework, the formulation found in [8] is recommended.

9.1 The Variational Setting for a Macroscale Beam

As mentioned previously, VCH formulates the macroscale and subscale problems by considering the fully resolved problem, illustrated in Figure 9.1. Its weak form is stated as finding $\boldsymbol{u} \in \mathbb{U}$ such that

$$\int_{\Omega} \boldsymbol{\sigma} : \boldsymbol{\varepsilon}[\delta \boldsymbol{u}] \; \mathrm{d}\Omega = \int_{\nu} \boldsymbol{t}_{\nu} \cdot \delta \boldsymbol{u} \; \mathrm{d}\Gamma + \int_{\Gamma_N} \boldsymbol{t}_p \cdot \delta \boldsymbol{u} \; \mathrm{d}\Gamma \quad \forall \; \delta \boldsymbol{u} \in \mathbb{U}^0, \tag{9.1}$$

which may be expressed in abstract form as

$$a(\boldsymbol{u}, \delta \boldsymbol{u}) = l(\delta \boldsymbol{u}) \quad \forall \; \delta \boldsymbol{u} \in \mathbb{U}^0.$$

The solution and test fields of the fully resolved problem, as well as their respective spaces, may be decomposed into a smooth macroscale contribution and a fluctuating subscale contribution. This split gives that

$$\boldsymbol{u} = \boldsymbol{u}^M + \boldsymbol{u}^S \tag{9.2}$$

and

$$\delta \boldsymbol{u} = \delta \boldsymbol{u}^M + \delta \boldsymbol{u}^S \tag{9.3}$$

where superscript M and S denote the macroscale and subscale, respectively. Inserting the decomposition into the fully resolved problem, gives

$$a(\boldsymbol{u}, \delta \boldsymbol{u}^M) = l(\delta \boldsymbol{u}^M) \quad \forall \; \delta \boldsymbol{u}^M \in \bar{\mathbb{U}}^0 \tag{9.4}$$

$$a(\boldsymbol{u}, \delta \boldsymbol{u}^S) = l(\delta \boldsymbol{u}^S) \quad \forall \; \delta \boldsymbol{u}^M \in \mathbb{U}^0_{\square}, \tag{9.5}$$

which define the macroscale and subscale problem in abstract notation, respectively. Note that, starting from the variational form, two coupled problems have been derived.

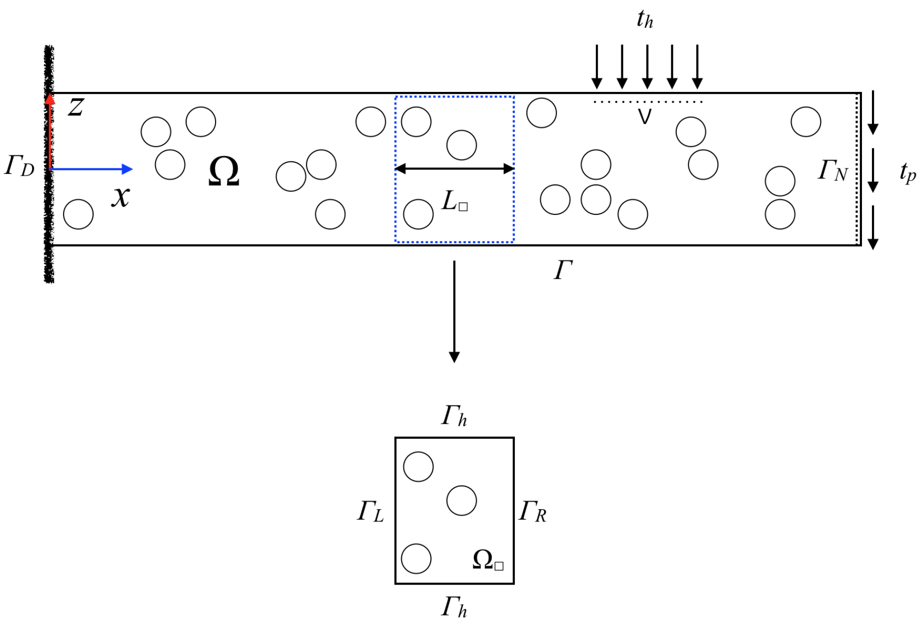

Figure 9.1: Fully resolved beam problem.

The following macroscale displacement field is introduced:

$$\bar{\boldsymbol{u}} = \quad (\bar{u}_x, \bar{u}_z, \bar{\phi}) \text{ on } [0, L],$$

where $\bar{u_x}, \bar{u_z}$ and $\bar{\phi}$ denote mid-plane displacements and rotation, respectively, and L the length of the beam. To incorporate this field into the problem, prolongation conditions must be defined that link $\boldsymbol{u}^M$ to $\bar{\boldsymbol{u}}$. Furthermore, in order to ensure that the decomposition in Equations (9.2) and (9.3) is unique, restrictions must be posed on the subscale field. In this particular setting, these restrictions are based on the prolongation and homogenisation mappings $\mathbb{A}$ and $\mathbb{A}^*$, respectively. For the case of prolongation, the displacement of the macroscale beam is expressed on the SVE with the mapping defined as

$$\boldsymbol{u}^M = \mathbb{A} \cdot \bar{\boldsymbol{u}}. \tag{9.6}$$

The subscale stress measures are homogenised by

$$\bar{\boldsymbol{u}} = \mathbb{A}^* \cdot \boldsymbol{u} = \mathbb{A}^*(\boldsymbol{u}^M + \boldsymbol{u}^S) = \mathbb{A}^* \cdot \boldsymbol{u}^M + \mathbb{A}^* \boldsymbol{u}^S. \tag{9.7}$$

Inserting Equation (9.6) into Equation (9.7) gives that

$$\bar{\boldsymbol{u}} = \mathbb{A}^*\mathbb{A} \cdot \bar{\boldsymbol{u}} + \mathbb{A}^* \boldsymbol{u}^S,$$

which is clearly only valid if

$$\mathbb{A}^*\mathbb{A} \cdot \bar{\boldsymbol{u}} = \bar{\boldsymbol{u}}, \tag{9.8}$$

and

$$\mathbb{A}^* \boldsymbol{u}^S = 0. \tag{9.9}$$

9.2 Defining the Subscale to Macroscale Transition

In order to formulate the subscale to macroscale transition, i.e. to find the proper homogenisation of $\bar{N}, \bar{M}$ and $\bar{V}$, a prolongation condition must be defined such that $\boldsymbol{u}^M$ can be expressed in terms of $\bar{\boldsymbol{u}}$ within an SVE. This is done through a first order Taylor expansion around the mid-line coordinate $\bar{x}$. Specifically

$$\boldsymbol{u}^M = \begin{bmatrix} u_x^M \\ u_z^M \end{bmatrix} = \mathbb{A} \cdot \bar{\boldsymbol{u}} = \begin{bmatrix} \bar{u}^0(\bar{x}) + \frac{\partial \bar{u}^0}{\partial x}[x - \bar{x}] - z\bar{\phi}(\bar{x}) - z\frac{\partial \bar{\phi}}{\partial x}[x - \bar{x}] \\ \bar{w}(\bar{x}) + \frac{\partial \bar{w}}{\partial x}[x - \bar{x}] \end{bmatrix}$$

and

$$\delta\boldsymbol{u}^M = \begin{bmatrix} \delta u_x^M \\ \delta u_z^M \end{bmatrix} = \mathbb{A} \cdot \delta\bar{\boldsymbol{u}} = \begin{bmatrix} \delta\bar{u}^0(\bar{x}) + \frac{\partial \delta\bar{u}^0}{\partial x}[x - \bar{x}] - z\delta\bar{\phi}(\bar{x}) - z\frac{\partial \delta\bar{\phi}}{\partial x}[x - \bar{x}] \\ \delta\bar{w}(\bar{x}) + \frac{\partial \delta\bar{w}}{\partial x}[x - \bar{x}] \end{bmatrix}.$$

The macroscale problem given by Equation (9.4) can then be expressed as

$$\int_\Omega \boldsymbol{\sigma} : \boldsymbol{\varepsilon}[\delta\boldsymbol{u}^M] \ \mathrm{d}\Omega = \int_\nu \boldsymbol{t}_\nu \cdot \delta\boldsymbol{u}^M \ \mathrm{d}\Gamma + \int_{\Gamma_N} \boldsymbol{t}_p \cdot \delta\boldsymbol{u}^M \ \mathrm{d}\Gamma \quad \forall\ \delta\bar{\boldsymbol{u}} \in \bar{\mathbb{U}}. \tag{9.10}$$

By introducing the running averages over the SVE domain defined as

$$\int_\Omega f \ \mathrm{d}\Omega = \int_0^L \frac{1}{L_\square} \int_{\Omega_\square} f \ \mathrm{d}\Omega \ \mathrm{d}x \text{ and } \int_\Gamma g \ \mathrm{d}\Gamma = \int_0^L \frac{1}{L_\square} \int_{\Gamma_\square} g \ \mathrm{d}\Gamma \ \mathrm{d}x,$$

Equation (9.4), may be restated as

$$\int_0^L \frac{1}{L_\square} \int_{\Omega_\square} \boldsymbol{\sigma} : \boldsymbol{\varepsilon}[\delta\boldsymbol{u}^M] \ \mathrm{d}\Omega \ \mathrm{d}x = \int_0^L \frac{1}{L_\square} \int_{\nu_\square} \boldsymbol{t}_\nu \cdot \delta\boldsymbol{u}^M \ \mathrm{d}\Gamma \ \mathrm{d}x + \int_{\Gamma_N} \boldsymbol{t}_p \cdot \delta\boldsymbol{u}^M \ \mathrm{d}\Gamma \quad \forall\ \delta\bar{\boldsymbol{u}} \in \bar{\mathbb{U}}. \tag{9.11}$$

For brevity, the right-hand side of this is denoted as $\hat{l}(\delta\boldsymbol{u}^M)$ from this point forward.

Based on the prolongation conditions defined at the start of this section, it is possible to express $\delta\boldsymbol{u}^M$ in terms of $\delta\bar{\boldsymbol{u}}$ such that the integrand of the first term Equation (9.11) gives

$$\begin{aligned} \boldsymbol{\sigma} : \boldsymbol{\varepsilon}[\delta\boldsymbol{u}^M] &= \sigma_{xx}\varepsilon_{xx}[\delta\boldsymbol{u}^M] + 2 \cdot \tau_{xz}\varepsilon_{xz}[\delta\boldsymbol{u}^M] + \sigma_{zz}\varepsilon_{zz}[\delta\boldsymbol{u}^M] \\ &= \sigma_{xx}\left(\frac{\partial \delta\bar{u}^0}{\partial x} - z\frac{\partial \delta\bar{\phi}}{\partial x}\right) + \tau_{xz}\left(\frac{\partial \delta\bar{w}}{\partial x} - \delta\bar{\phi} - \frac{\partial \delta\bar{\phi}}{\partial x}[x - \bar{x}]\right) + 0, \end{aligned}$$

which results in

$$\int_0^L \frac{1}{L_\square} \int_{\Omega_\square} \sigma_{xx} \left(\frac{\partial \delta \bar{u}^0}{\partial x} - z \frac{\partial \delta \bar{\phi}}{\partial x} \right) + \tau_{xz} \left(\frac{\partial \delta \bar{w}}{\partial x} - \delta \bar{\phi} - \frac{\partial \delta \bar{\phi}}{\partial x} [x - \bar{x}] \right) \, \mathrm{d}\Omega \, \mathrm{d}x = \hat{l}(\delta \boldsymbol{u}^M),$$

when reintroduced into the weak formulation. The macroscale measures $\frac{\delta \bar{u}^0}{\partial x}$, $\frac{\partial \delta \bar{\phi}}{\partial x}$, $\frac{\partial \delta \bar{w}}{\partial x}$, and $\delta \bar{\phi}$, are constant in the subscale domain. As such, these measures can be removed from the integrals over $\Omega_\square$. This result in

$$\begin{aligned} \int_0^L \frac{1}{L_\square} \int_{\Omega_\square} \sigma_{xx} \, \mathrm{d}\Omega \, \mathrm{d}x \left[\frac{\partial \delta \bar{u}^0}{\partial x} \right] - \int_0^L \frac{1}{L_\square} \int_{\Omega_\square} \left(\sigma_{xx} \cdot z + \tau_{xz} [x - \bar{x}] \right) \, \mathrm{d}\Omega \, \mathrm{d}x \left[\frac{\partial \delta \bar{\phi}}{\partial x} \right] + \\ + \int_0^L \frac{1}{L_\square} \int_{\Omega_\square} \tau_{xz} \, \mathrm{d}\Omega \, \mathrm{d}x \left[-\delta \bar{\phi} + \frac{\partial \delta \bar{w}}{\partial x} \right] = \hat{l}(\delta \boldsymbol{u}^M). \end{aligned} \tag{9.12}$$

The definitions for the normal force, bending moment and shear force can now be identified from Equation (9.12). Note that these integrated stress measures have been systematically derived from the field equations. The variationally consistent macroscale problem, considering the chosen prolongation $\mathbb{A}$, may be stated as finding $\bar{\boldsymbol{u}} \in \bar{\mathbb{U}}$ such that

$$\int_0^L \bar{N} \frac{\partial \delta \bar{u}^0}{\partial x} - \bar{M} \frac{\partial \delta \bar{\phi}}{\partial x} + \bar{V} \left[-\delta \bar{\phi} + \frac{\partial \delta \bar{w}}{\partial x} \right] \, \mathrm{d}x = \hat{l}(\delta \boldsymbol{u}^M) \quad \forall \, \delta \bar{\boldsymbol{u}} \in \bar{\mathbb{U}}^0$$

where the normal force, bending moment, and shear force were retrieved as

$$\bar{N} = \frac{1}{L_\square} \int_{\Omega_\square} \sigma_{xx} \, \mathrm{d}\Omega, \tag{9.13}$$

$$\bar{M} = \frac{1}{L_\square} \int_{\Omega_\square} \left(\sigma_{xx} \cdot z + \tau_{xz} [x - \bar{x}] \right) \, \mathrm{d}\Omega \tag{9.14}$$

and

$$\bar{V} = \frac{1}{L_\square} \int_{\Omega_\square} \tau_{xz} \, \mathrm{d}\Omega, \tag{9.15}$$

respectively. Note that Equations (9.13), (9.14) and (9.15) define the subscale to macroscale transition of the stress measures, for the chosen prolongation method. It is also worth pointing out, that the derived subscale to macroscale transition is equivalent to that found in [7].

9.3 Defining the Macroscale to Subscale Transition

The macroscale to subscale transition is formulated by introducing the homogenisation mapping $\mathbb{A}^*$. Recall from Equations (9.8) and (9.9), that the homogenisation mapping must satisfy

$$\mathbb{A}\mathbb{A}^* = \mathbb{I}$$

and

$$\mathbb{A}^* u^S = 0,$$

where $\mathbb{I}$ denotes the identity operator.

The homogenisation mapping $\mathbb{A}^*$ must result in 6 macroscale components,namely $\bar{u}^0$, $\bar{w}$, $\bar{\phi}$ and their derivatives. One possibility is to define the homogenisation mapping such that

$$\bar{u}^0 = \frac{1}{|\Omega_\Box|}\int_{\Omega_\Box} u_x \ \mathrm{d}\Omega \tag{9.16}$$

$$\bar{w} = \frac{1}{|\Omega_\Box|}\int_{\Omega_\Box} u_z \ \mathrm{d}\Omega \tag{9.17}$$

$$\bar{\phi} = -\frac{1}{|\Omega_\Box|}\int_{\Omega_\Box} z u_x \ \mathrm{d}\Omega \ \frac{1}{I_\Box} \tag{9.18}$$

$$\frac{\partial \bar{u}}{\partial x} = \frac{1}{|\Omega_\Box|}\int_{\Omega_\Box} \frac{\partial u_x}{\partial x} \ \mathrm{d}\Gamma \tag{9.19}$$

$$\frac{\partial \bar{w}}{\partial x} = \frac{1}{|\Omega_\Box|}\int_{\Omega_\Box} \frac{\partial u_z}{\partial x} \ \mathrm{d}\Gamma \tag{9.20}$$

$$\frac{\partial \bar{\phi}}{\partial x} = -\frac{1}{|\Omega_\Box|}\int_{\Omega_\Box} z\frac{\partial u_x}{\partial x} \ \mathrm{d}\Omega \ \frac{1}{I_\Box}. \tag{9.21}$$

Giving closer consideration to Equation (9.16) and introducing the decomposition given by Equation (9.7) results in

$$\begin{aligned}\bar{u}^0 &= \frac{1}{|\Omega_\Box|}\int_{\Omega_\Box} u_x^M \ \mathrm{d}\Omega + \frac{1}{|\Omega_\Box|}\int_{\Omega_\Box} u_x^S \ \mathrm{d}\Omega \\ &= \frac{1}{|\Omega_\Box|}\int_{\Omega_\Box} \left(\bar{u}^0 + \frac{\partial \bar{u}^0}{\partial x}[x-\bar{x}] - z\bar{\phi} - z\frac{\partial \bar{\phi}}{\partial x}[x-\bar{x}]\right) \ \mathrm{d}\Omega + \frac{1}{|\Omega_\Box|}\int_{\Omega_\Box} u_x^S \ \mathrm{d}\Omega.\end{aligned}$$

The constraints given by Equations (9.8) and (9.9) are then satisfied if

$$\frac{1}{|\Omega_\Box|}\int_{\Omega_\Box} u_x^S \ \mathrm{d}\Omega = 0. \tag{9.22}$$

Similarly, considering Equations (9.17) and (9.18) in more detail gives

$$\bar{w} = \frac{1}{|\Omega_\Box|}\int_{\Omega_\Box} \left(\bar{w} + \frac{\partial \bar{w}}{\partial x}[x-\bar{x}]\right) \ \mathrm{d}\Omega + \frac{1}{|\Omega_\Box|}\int_{\Omega_\Box} u_z^S \ \mathrm{d}\Omega$$

and

$$\bar{\phi} = \frac{1}{|\Omega_\Box|}\int_{\Omega_\Box} \left(z\bar{u}^0 + z\frac{\partial \bar{u}^0}{\partial x}[x-\bar{x}] - z^2\bar{\phi} - z^2\frac{\partial \bar{\phi}}{\partial x}[x-\bar{x}]\right) \ \mathrm{d}\Omega \frac{1}{|\Omega_\Box|}\int_{\Omega_\Box} z u_x^S \ \mathrm{d}\Omega.$$

The homogenisation conditions given by Equations (9.8) and (9.9) are satisfied if

$$\frac{1}{|\Omega_\Box|}\int_{\Omega_\Box} u_z^S \ \mathrm{d}\Omega = 0 \tag{9.23}$$

$$\frac{1}{|\Omega_\Box|}\int_{\Omega_\Box} z u_x^S \ \mathrm{d}\Omega = 0 \tag{9.24}$$

and

$$I_\Box = \frac{h^2}{12}.$$

What remains to be considered are the derivatives of $\bar{u}^0, \bar{w}$ and $\bar{\phi}$. Using Gauss' theorem, Equation (9.19) may also be expressed as an integral over the boundary. That is

$$\begin{aligned}\bar{u}^{0\prime} &= \frac{1}{|\Omega_\Box|}\int_{\Gamma_\Box} u_x n_x \ \mathrm{d}\Gamma \\ &= \frac{1}{|\Omega_\Box|}\int_{\Gamma_R} [\![u_x]\!] \ \mathrm{d}\Gamma,\end{aligned}$$

where n_x denotes the outward facing normal. Introducing the decomposition gives

$$\bar{u}^{0\prime} = \frac{1}{|\Omega_\square|} \int_{\Gamma_R} [\![u_x^M]\!] \, \mathrm{d}\Gamma + \frac{1}{|\Omega_\square|} \int_{\Gamma_R} [\![u_x^S]\!] \, \mathrm{d}\Gamma,$$

which means that in order to satisfy the homogenisation conditions:

$$\frac{1}{|\Omega_\square|} \int_{\Gamma_R} [\![u_x^S]\!] \, \mathrm{d}\Gamma = 0.$$

Following this process again for $\bar{u}_z'$ and $\bar{\phi}'$ gives the last two constraints. To summarise, the variationally consistent macro to subscale transition is defined by the following six constraints:

$$\int_{\Omega_\square} u_x^S \, \mathrm{d}\Omega = 0 \tag{9.25}$$

$$\int_{\Omega_\square} z u_x^S \, \mathrm{d}\Omega = 0 \tag{9.26}$$

$$\int_{\Omega_\square} u_z^S \, \mathrm{d}\Omega = 0 \tag{9.27}$$

$$\int_{\Gamma_R} [\![u_x^S]\!] \, \mathrm{d}\Gamma = 0 \tag{9.28}$$

$$\int_{\Gamma_R} z [\![u_x^S]\!] \, \mathrm{d}\Gamma = 0 \tag{9.29}$$

$$\int_{\Gamma_R} [\![u_z^S]\!] \, \mathrm{d}\Gamma = 0. \tag{9.30}$$

10 Computational Homogenisation Using the Weakest Possible Constraints Derived from VCH

10.1 Macroscale - Subscale Transition

The constraints derived previously in Section 9, are imposed through the consideration of their weakest possible form. This yields

$$\int_{\Omega_\square} \delta\bar{\mu}_x \cdot u_x^S \, \mathrm{d}\Omega = 0,$$

$$\int_{\Omega_\square} \delta\hat{\mu}_x \cdot z \cdot u_x^S \, \mathrm{d}\Omega = 0,$$

$$\int_{\Omega_\square} \delta\mu_z \cdot u_z^S \, \mathrm{d}\Omega = 0,$$

$$\int_{\Gamma_R} \delta\bar{\lambda}_x \cdot [\![u_x^S]\!] \, \mathrm{d}\Gamma = 0,$$

$$\int_{\Gamma_R} \delta\hat{\lambda}_x \cdot z \cdot [\![u_x^S]\!] \, \mathrm{d}\Gamma = 0,$$

$$\int_{\Gamma_R} \delta\lambda_z \cdot [\![u_z^S]\!] \, \mathrm{d}\Gamma = 0,$$

where the test functions for the volumetric and boundary constraints are defined as $\delta\bar{\mu}_x, \delta\hat{\mu}_x, \delta\mu_z \in \mathbb{R}$ and $\delta\bar{\lambda}_x, \delta\hat{\lambda}_x, \delta\lambda_z \in \mathbb{R}$ respectively. Considering the decomposition $\boldsymbol{u} = \boldsymbol{u}^M + \boldsymbol{u}^S$, these constraints result in

$$
\begin{aligned}
\int_{\Omega_\square} \delta\bar{\mu}_x \cdot u_x \, \mathrm{d}\Omega &= \int_{\Omega_\square} \delta\bar{\mu}_x \cdot u_x^M \, \mathrm{d}\Omega = \int_{\Omega_\square} \delta\bar{\mu}_x \left(-z\bar{\phi} + \bar{\varepsilon}^0[x-\bar{x}] - z\bar{\phi}'[x-\bar{x}]\right) \, \mathrm{d}\Omega = 0 \\
\int_{\Omega_\square} \delta\hat{\mu}_x \cdot z \cdot u_x \, \mathrm{d}\Omega &= \int_{\Omega_\square} \delta\hat{\mu}_x \cdot z \cdot u_x^M \, \mathrm{d}\Omega \int_{\Omega_\square} \delta\hat{\mu}_x \left(-z^2\bar{\phi} + z\bar{\varepsilon}^0[x-\bar{x}] - z^2\bar{\phi}'[x-\bar{x}]\right) \, \mathrm{d}\Omega = -\delta\hat{\mu}_x\bar{\phi}L_\square\frac{h^3}{12} \\
\int_{\Omega_\square} \delta\mu_z \cdot u_z \, \mathrm{d}\Omega &= \int_{\Omega_\square} \delta\mu_z \cdot u_z^M \, \mathrm{d}\Omega = \int_{\Omega_\square} \delta\mu_z \left(\bar{w}'[x-\bar{x}]\right) \, \mathrm{d}\Omega = 0 \\
\int_{\Gamma_R} \delta\bar{\lambda}_x \cdot [\![u_x]\!] \, \mathrm{d}\Gamma &= \int_{\Gamma_R} \delta\bar{\lambda}_x \cdot [\![u_x^M]\!] \, \mathrm{d}\Gamma = \int_{\Gamma_R} \delta\bar{\lambda}_x L_\square \left(\bar{\varepsilon}^0 - z\bar{\phi}'\right) \, \mathrm{d}\Gamma = \delta\hat{\lambda}_x\bar{\varepsilon}^0 L_\square h \\
\int_{\Gamma_R} \delta\hat{\lambda}_x \cdot z \cdot [\![u_x]\!] \, \mathrm{d}\Gamma &= \int_{\Gamma_R} \delta\hat{\lambda}_x \cdot z \cdot [\![u_x^M]\!] \, \mathrm{d}\Gamma = \int_{\Gamma_R} \left(z\bar{\varepsilon}^0 - z^2\bar{\phi}'\right) \, \mathrm{d}\Gamma = -\delta\hat{\lambda}_x\bar{\phi}' L_\square\frac{h^3}{12} \\
\int_{\Gamma_R} \delta\lambda_z \cdot [\![u_z]\!] \, \mathrm{d}\Gamma &= \int_{\Gamma_R} \delta\lambda_z \cdot [\![u_z^M]\!] \, \mathrm{d}\Gamma = \int_{\Gamma_R} \delta\lambda_z L_\square \bar{w}' \, \mathrm{d}\Gamma = \delta\lambda_z\bar{w}' L_\square h.
\end{aligned}
$$

This may be summarised by

$$
\int_{\Omega_\square} \delta\boldsymbol{b}_\mu \cdot \boldsymbol{u} \, \mathrm{d}\Omega = \begin{bmatrix}\delta\bar{\mu}_x & \delta\hat{\mu}_x & \delta\mu_z\end{bmatrix} \begin{bmatrix} 0 \\ -\bar{\phi}L_\square\frac{h^3}{12} \\ 0 \end{bmatrix} \tag{10.1}
$$

and

$$
\int_{\Gamma_R} \delta\boldsymbol{t}_\lambda \cdot [\![\boldsymbol{u}]\!] \, \mathrm{d}\Gamma = \begin{bmatrix}\delta\bar{\lambda}_x & \delta\hat{\lambda}_x & \delta\lambda_z\end{bmatrix} \begin{bmatrix} \bar{\varepsilon}^0 L_\square \\ -\bar{\phi}' L_\square\frac{h^3}{12} \\ \bar{w}' L_\square h \end{bmatrix}. \tag{10.2}
$$

10.2 Boundary Value Problem Formulation

10.2.1 Strong Form

The strong form is stated as

$$
-\boldsymbol{\sigma} \cdot \boldsymbol{\nabla} = \boldsymbol{b} \text{ in } \Omega_\square \tag{10.3}
$$

$$
\boldsymbol{t} = \boldsymbol{0} \text{ on } \Gamma_h \tag{10.4}
$$

$$
\int_{\Omega_\square} \delta\boldsymbol{b}_\mu \cdot \boldsymbol{u} \, \mathrm{d}\Omega = \begin{bmatrix}\delta\bar{\mu}_x & \delta\hat{\mu}_x & \delta\mu_z\end{bmatrix} \begin{bmatrix} 0 \\ -\bar{\phi}L_\square\frac{h^3}{12} \\ 0 \end{bmatrix} \quad \forall\ \delta\hat{\mu}_x, \delta\hat{\mu}_x, \delta\mu_z \in \mathbb{R} \tag{10.5}
$$

$$
\int_{\Gamma_R} \delta\boldsymbol{t}_\lambda \cdot [\![\boldsymbol{u}]\!] \, \mathrm{d}\Gamma = \begin{bmatrix}\delta\bar{\lambda}_x & \delta\hat{\lambda}_x & \delta\lambda_z\end{bmatrix} \begin{bmatrix} \bar{\varepsilon}^0 L_\square \\ -\bar{\phi}' L_\square\frac{h^3}{12} \\ \bar{w}' L_\square h \end{bmatrix} \quad \forall\ \delta\hat{\lambda}_x, \delta\hat{\lambda}_x, \delta\lambda_z \in \mathbb{R}. \tag{10.6}
$$

10.2.2 Weak Form

As shown in Section 5 the equilibrium equation given in Equation (10.3), may be expressed in its weak form as

$$
\int_{\Omega_\square} \boldsymbol{\sigma} : [\delta\boldsymbol{u} \otimes \boldsymbol{\nabla}] \, \mathrm{d}\Omega - \int_{\Omega_\square} \boldsymbol{b} \cdot \delta\boldsymbol{u} \, \mathrm{d}\Omega - \int_{\Gamma_L \cup \Gamma_R} \boldsymbol{t} \cdot \delta\boldsymbol{u} \, \mathrm{d}\Gamma = 0 \quad \forall \delta\boldsymbol{u} \in \mathbb{U}_\square^0. \tag{10.7}
$$

The traction vector and body force vector may be expressed in terms of Lagrange multipliers, where

$$
\boldsymbol{b} = \boldsymbol{b}_\mu = \begin{bmatrix} \bar{\mu}_x + \hat{\mu}_x \cdot z \\ \mu_z \end{bmatrix} \text{ and } \boldsymbol{t}^+ = \boldsymbol{t}_\lambda^+ = \begin{bmatrix} \bar{\lambda}_x + \hat{\lambda}_x \cdot z \\ \lambda_z \end{bmatrix}.
$$

and $\boldsymbol{u} \in \mathbb{U}_\square$ and $\bar{\mu}_x, \hat{\mu}_x, \mu_z, \bar{\lambda}_x, \hat{\lambda}_x, \lambda_z \in \mathbb{R}$. By enforcing anti-periodicity, i.e. $\boldsymbol{t}_\lambda^+ = -\boldsymbol{t}_\lambda^-$, the third term in Equation (10.7) may be expressed as

$$\int_{\Gamma_L \cup \Gamma_R} \boldsymbol{t} \cdot \delta\boldsymbol{u} \; \mathrm{d}\Gamma = \int_{\Gamma_R} \boldsymbol{t}_\lambda [\![\boldsymbol{u}]\!] \; \mathrm{d}\Gamma.$$

The weak formulation can then be stated as finding $\boldsymbol{u} \in \mathbb{U}_\square$ and $\bar{\mu}_x, \hat{\mu}_x, \mu_z, \bar{\lambda}_x, \hat{\lambda}_x, \lambda_z \in \mathbb{R}$ such that

$$a_\square(\boldsymbol{u}, \delta\boldsymbol{u}) - b_\square(\boldsymbol{b}_\mu, \delta\boldsymbol{u}) - d_\square(\boldsymbol{t}_\lambda, \delta\boldsymbol{u}) = 0 \quad \forall\; \delta\boldsymbol{u} \in \mathbb{U}_\square^0 \tag{10.8}$$

$$-b_\square(\delta\boldsymbol{b}_\mu, \boldsymbol{u}) = \begin{bmatrix} \delta\bar{\mu}_x & \delta\hat{\mu}_x & \delta\mu_z \end{bmatrix} \begin{bmatrix} 0 \\ \bar{\phi} L_\square \frac{h^3}{12} \\ 0 \end{bmatrix} \quad \forall\; \delta\bar{\mu}_x, \delta\hat{\mu}_x, \delta\mu_z \in \mathbb{R} \tag{10.9}$$

$$-d_\square(\delta\boldsymbol{t}_\lambda, \boldsymbol{u}) = \begin{bmatrix} \delta\bar{\lambda}_x & \delta\hat{\lambda}_x & \delta\lambda_z \end{bmatrix} \begin{bmatrix} -\bar{\varepsilon}^0 L_\square \\ \bar{\phi}' L_\square \frac{h^3}{12} \\ -\bar{w}' L_\square h \end{bmatrix} \quad \forall\; \delta\bar{\lambda}_x, \delta\hat{\lambda}_x, \delta\lambda_z \in \mathbb{R} \tag{10.10}$$

where

$$\begin{aligned} a_\square(\boldsymbol{u}, \delta\boldsymbol{u}) &= \int_{\Omega_\square} \boldsymbol{\sigma} : [\delta\boldsymbol{u} \otimes \boldsymbol{\nabla}] \; \mathrm{d}\Omega, \\ b_\square(\boldsymbol{b}_\mu, \delta\boldsymbol{u}) &= \int_{\Omega_\square} \boldsymbol{b}_\mu \cdot \delta\boldsymbol{u} \; \mathrm{d}\Omega, \\ b_\square(\delta\boldsymbol{b}_\mu, \boldsymbol{u}) &= \int_{\Omega_\square} \delta\boldsymbol{b}_\mu \cdot \boldsymbol{u} \; \mathrm{d}\Omega, \\ d_\square(\boldsymbol{t}_\lambda, \delta\boldsymbol{u}) &= \int_{\Gamma_R} \boldsymbol{t}_\lambda \cdot [\![\delta\boldsymbol{u}]\!] \; \mathrm{d}\Gamma, \\ d_\square(\delta\boldsymbol{t}_\lambda, \boldsymbol{u}) &= \int_{\Gamma_R} \delta\boldsymbol{t}_\lambda \cdot [\![\boldsymbol{u}]\!] \; \mathrm{d}\Gamma \end{aligned}$$

and

$$\begin{aligned} \mathbb{U}_\square &= \left\{ \boldsymbol{u} : \int_\Omega |\boldsymbol{u}|^2 + |\boldsymbol{u} \otimes \boldsymbol{\nabla}|^2 \mathrm{d}\Omega < \infty \right\}, \\ \mathbb{U}_\square^0 &= \left\{ \delta\boldsymbol{u} : \int_\Omega |\delta\boldsymbol{u}|^2 + |\delta\boldsymbol{u} \otimes \boldsymbol{\nabla}|^2 \mathrm{d}\Omega < \infty \right\}. \end{aligned}$$

10.2.3 Finite Element Approximation

Introducing the FE approximations

$$\underline{\boldsymbol{u}} \approx \underline{\boldsymbol{u}}_h = \underline{\boldsymbol{N}}_u \underline{\boldsymbol{a}}_u \text{ and } \delta\underline{\boldsymbol{u}} \approx \delta\underline{\boldsymbol{u}}_h = \underline{\boldsymbol{N}}_u \delta\underline{\boldsymbol{a}}_u,$$

into (10.8), gives

$$\int_{\Omega_\square} \boldsymbol{\sigma} : [\delta\boldsymbol{u} \otimes \boldsymbol{\nabla}] \; \mathrm{d}\Omega \approx \delta\underline{\boldsymbol{a}}_u^T \int_{\Omega_\square} \underline{\boldsymbol{B}}_u^T \underline{\boldsymbol{D}} \underline{\boldsymbol{B}}_u \; \mathrm{d}\Omega \; \underline{\boldsymbol{a}}_u = \delta\underline{\boldsymbol{a}}_u^T \underline{\boldsymbol{K}}_{uu} \underline{\boldsymbol{a}}_u.$$

Moreover, introducing the approximations given by

$$\underline{\boldsymbol{b}}_\mu = \begin{bmatrix} \bar{\mu}_x + \hat{\mu}_x \cdot z \\ \mu_z \end{bmatrix} = \begin{bmatrix} 1 & z & 0 \\ 0 & 0 & 1 \end{bmatrix} \begin{bmatrix} \bar{\mu}_x \\ \hat{\mu}_x \\ \mu_z \end{bmatrix} = \underline{\boldsymbol{N}}_\mu \underline{\boldsymbol{a}}_\mu \text{ and } \delta\underline{\boldsymbol{b}}_\mu = \begin{bmatrix} 1 & z & 0 \\ 0 & 0 & 1 \end{bmatrix} \begin{bmatrix} \delta\bar{\mu}_x \\ \delta\hat{\mu}_x \\ \delta\mu_z \end{bmatrix} = \underline{\boldsymbol{N}}_\mu \delta\underline{\boldsymbol{a}}_\mu$$

into Equations (10.8) and (10.9) results in

$$\int_{\Omega_\square} \boldsymbol{b}_\mu \cdot \delta\boldsymbol{u} \; \mathrm{d}\Omega \approx \delta\underline{\boldsymbol{a}}_u^T \int_{\Omega_\square} \underline{\boldsymbol{N}}_u^T \underline{\boldsymbol{N}}_\mu \; \mathrm{d}\Omega \underline{\boldsymbol{a}}_\mu = \delta\underline{\boldsymbol{a}}_u^T \underline{\boldsymbol{K}}_{u\mu} \underline{\boldsymbol{a}}_\mu,$$

and

$$\int_{\Omega_\square} \delta \boldsymbol{b}_\mu \cdot \boldsymbol{u} \; \mathrm{d}\Omega \approx \delta \underline{\boldsymbol{a}}_\mu^T \underline{\boldsymbol{K}}_{\mu u} \underline{\boldsymbol{a}}_u,$$

$$\begin{bmatrix} \delta\bar{\mu}_x & \delta\hat{\mu}_x & \delta\mu_z \end{bmatrix} \begin{bmatrix} 0 \\ \bar{\phi} L_\square \frac{h^3}{12} \\ 0 \end{bmatrix} \approx \delta \underline{\boldsymbol{a}}_\mu^T \begin{bmatrix} 0 \\ \bar{\phi} L_\square \frac{h^3}{12} \\ 0 \end{bmatrix} = \delta \underline{\boldsymbol{a}}_\mu^T \underline{\boldsymbol{f}}_\mu,$$

respectively.

The traction approximations are defined as

$$\underline{\boldsymbol{t}}_\lambda^+ = \begin{bmatrix} \bar{\lambda}_x + \hat{\lambda}_x \cdot z \\ \lambda_z \end{bmatrix} = \begin{bmatrix} 1 & z & 0 \\ 0 & 0 & 1 \end{bmatrix} \begin{bmatrix} \bar{\lambda}_x \\ \hat{\lambda}_x \\ \lambda_z \end{bmatrix} = \underline{\boldsymbol{N}}_\lambda \underline{\boldsymbol{a}}_\lambda \text{ and } \delta \underline{\boldsymbol{t}}_\lambda^+ = \begin{bmatrix} 1 & z & 0 \\ 0 & 0 & 1 \end{bmatrix} \begin{bmatrix} \delta\bar{\lambda}_x \\ \delta\hat{\lambda}_x \\ \delta\lambda_z \end{bmatrix} = \underline{\boldsymbol{N}}_\lambda \delta \underline{\boldsymbol{a}}_\lambda.$$

Inserting these into Equations (10.8) and (10.10) gives

$$\int_{\Gamma_R} \boldsymbol{t}_\lambda^+ \cdot [\![\delta \boldsymbol{u}]\!] \; \mathrm{d}\Gamma \approx \delta \underline{\boldsymbol{a}}_u^T \int_{\Omega_\square} \underline{\boldsymbol{N}}_u^T \underline{\boldsymbol{N}}_\lambda \; \mathrm{d}\Omega \underline{\boldsymbol{a}}_\lambda = \delta \underline{\boldsymbol{a}}_u^T \underline{\boldsymbol{K}}_{u\lambda} \underline{\boldsymbol{a}}_\lambda,$$

and

$$\int_{\Gamma_R} \delta \boldsymbol{t}_\lambda^+ \cdot [\![\boldsymbol{u}]\!] \; \mathrm{d}\Gamma \approx \delta \underline{\boldsymbol{a}}_\lambda^T \underline{\boldsymbol{K}}_{\lambda u} \underline{\boldsymbol{a}}_u,$$

$$\begin{bmatrix} \delta\bar{\lambda}_x & \delta\hat{\lambda}_x & \delta\lambda_z \end{bmatrix} \begin{bmatrix} -\bar{\varepsilon}^0 L_\square \\ \bar{\phi}' L_\square \frac{h^3}{12} \\ -\bar{w}' L_\square h \end{bmatrix} \approx \delta \underline{\boldsymbol{a}}_\lambda^T \begin{bmatrix} -\bar{\varepsilon}^0 L_\square \\ \bar{\phi}' L_\square \frac{h^3}{12} \\ -\bar{w}' L_\square h \end{bmatrix} = \delta \underline{\boldsymbol{a}}_\lambda^T \underline{\boldsymbol{f}}_\lambda,$$

respectively.

The FE problem may be summarised by the following system of equations:

$$\begin{bmatrix} \underline{\boldsymbol{K}}_{uu} & -\underline{\boldsymbol{K}}_{u\mu} & -\underline{\boldsymbol{K}}_{u\lambda} \\ -\underline{\boldsymbol{K}}_{\mu u} & 0 & 0 \\ -\underline{\boldsymbol{K}}_{\lambda u} & 0 & 0 \end{bmatrix} \begin{bmatrix} \underline{\boldsymbol{a}}_u \\ \underline{\boldsymbol{a}}_\mu \\ \underline{\boldsymbol{a}}_\lambda \end{bmatrix} = \begin{bmatrix} \underline{\boldsymbol{0}} \\ \underline{\boldsymbol{f}}_\mu \\ \underline{\boldsymbol{f}}_\lambda \end{bmatrix}.$$

10.3 Subscale - Macroscale Transition

Based on the formulation found in Section 9.2, the subscale-to-macroscale transition takes place by first computing

$$\bar{M} = \frac{1}{L_\square} \int_{\Omega_\square} (\sigma_{xx} \cdot z + \tau_{xz} \cdot x) \; \mathrm{d}\Omega$$
$$\bar{N} = \frac{1}{L_\square} \int_{\Omega_\square} \sigma_{xx} \; \mathrm{d}\Omega$$

and

$$\bar{V} = \frac{1}{L_\square} \int_{\Omega_\square} \tau_{xz} \; \mathrm{d}\Omega$$

based on the obtained subscale stress field. As with the previous methods, the effective stiffness is then found considering that

$$\overline{EA} = \frac{\bar{N}}{\bar{\varepsilon}^0} \text{ for } \bar{\kappa} = \bar{\gamma} = 0$$
$$\overline{EI} = -\frac{\bar{M}}{\bar{\kappa}} \text{ for } \bar{\varepsilon}^0 = \bar{\gamma} = 0$$
$$\overline{K_s GA} = \frac{\bar{V}}{\bar{\gamma}} \text{ for } \bar{\varepsilon}^0 = \bar{\kappa} = 0.$$

10.4 Results

10.4.1 Homogeneous SVE

Homogeneous SVEs with a height of 10 mm, a thickness of 1 mm, and varying length are considered in order to determine if the prolongation and homogenisation methods formulated in Sections 10.1 through 10.3 cause any pathological size dependence. Figure 10.1 shows the resulting effective axial and bending stiffness. Again, this prolongation and homogenisation method is capable of accurately capturing the axial and bending stiffness. A remarkable improvement however is seen in Figure 10.2. It appears, that the use of the bulk constraint, more specifically:

$$\int_{\Omega_\square} \delta \boldsymbol{b}_\mu \cdot \boldsymbol{u} \, \mathrm{d}\Omega = \begin{bmatrix} \delta \bar{\mu}_x & \delta \hat{\mu}_x & \delta \mu_z \end{bmatrix} \begin{bmatrix} 0 \\ -\bar{\phi} L_\square \frac{h^3}{12} \\ 0 \end{bmatrix} \quad \forall \; \delta \hat{\mu}_x, \delta \hat{\mu}_x, \delta \mu_z \in \mathbb{R}$$

enables the appropriate shear behaviour to be captured for sufficiently large SVEs. Note, that for small SVEs this particular method is not ideal, giving extremely low values for the shear stiffness.

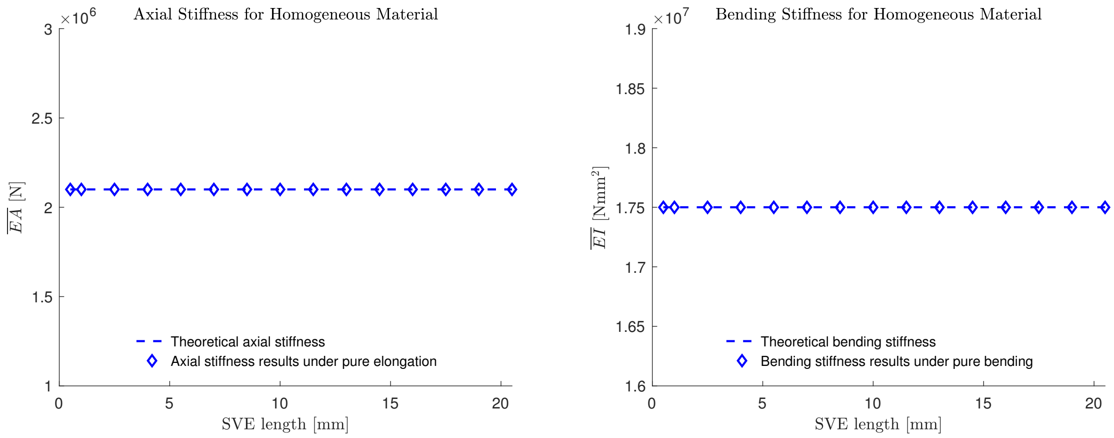

Figure 10.1: Resulting effective axial (left) and bending (right) stiffness considering homogeneous SVEs. Prolongation and homogenisation method defined using weak formulation of VCH.

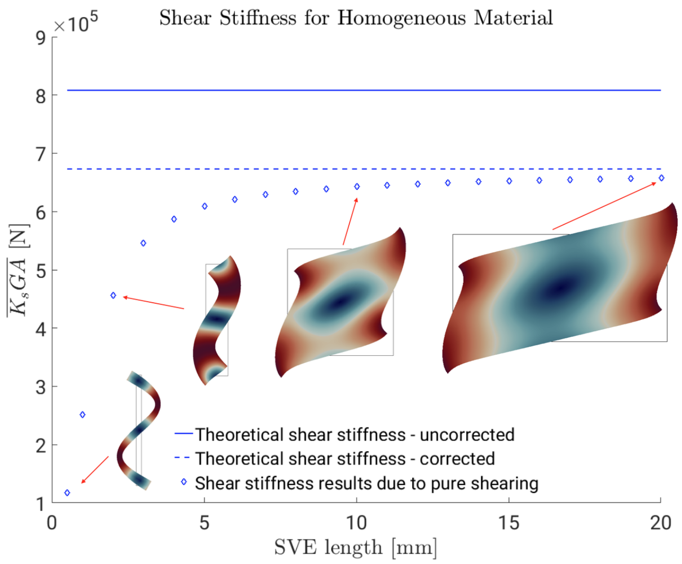

Figure 10.2: Shear stiffness for homogeneous SVEs of varying length The colour map indicates the deformation magnitude. Deformations magnified by factor of 5. Prolongation and homogenisation method defined using weak formulation of VCH.

10.4.2 Heterogeneous SVE

The application of the discussed computational homogenisation method to heterogeneous SVEs sampled from the field introduced in Section 5.2, results in Figures 10.3 and 10.4. The obtained axial and bending stiffness results, prove positive. There is also, a clear and remarkable improvement on the resulting shear stiffness. For sufficiently large SVEs, the obtained stiffness converges to what appears to be a reasonable value, without the severe and continuous softening that was seen in previous methods. The validity of these results, will again be verified by comparing the analytic solutions to that obtained through DNS.

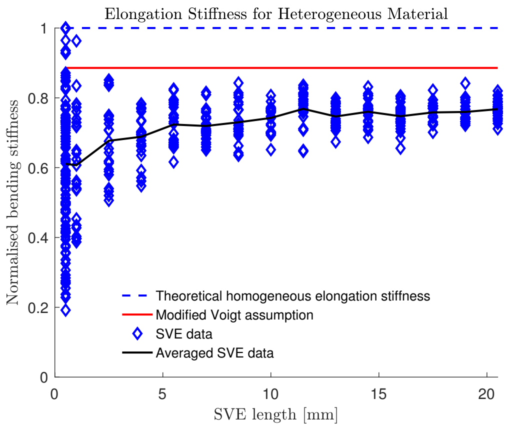

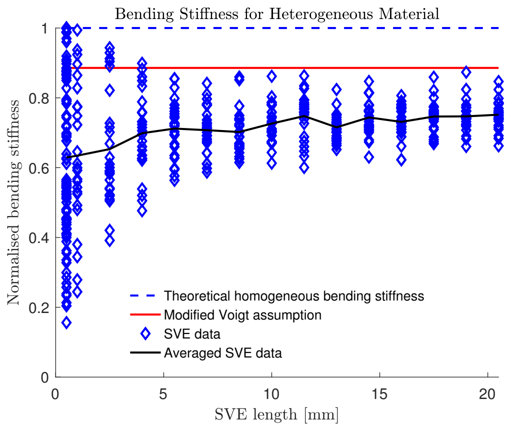

Figure 10.3: Normalised elongation stiffness (left) Normalised bending stiffness (right) for heterogeneous SVEs of varying length. Prolongation and homogenisation method defined using weak formulation of VCH.

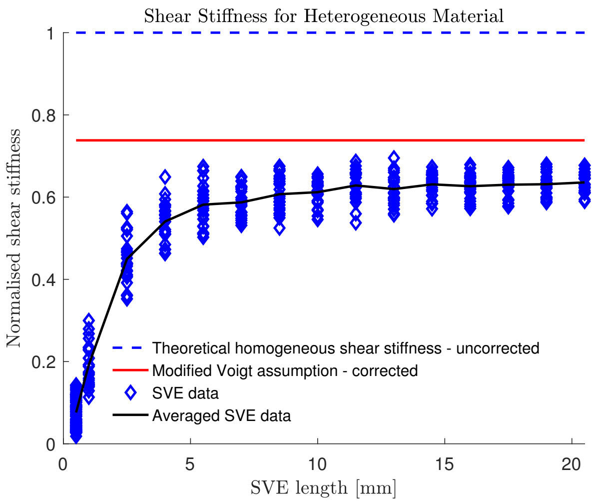

Figure 10.4: Normalised shear stiffness for heterogeneous SVEs of varying length. Prolongation and homogenisation method defined using weak formulation of VCH.

10.5 Validation

In order to validate the results obtained in Section 10.4.2, the three macroscale load cases introduced in Section 2.3 are considered. The analytic solutions, given by Equations (2.19), (2.20) and (2.21) are compared to the DNS results in Figures 10.5 and 10.6. The former compares the normalised tip displacement, whereas the later examines the full deformation field for a square SVE, as well as one with a length of 20.5 mm. Up until this point, obtaining satisfactory results for the second and third loading cases in particular proved difficult. However, it is now clear that the use of variationally consistent numerical homogenisation, in this way, is capable of capturing the shear response. Due to the choice of weak constraints, the stiffness results are initially soft for small SVEs, and converge from below. For that reason, to have an acceptable response a sufficiently large SVE is required. Considering a stronger implementation of the constraints formulated in Section 9.3 could improve results for smaller SVEs.

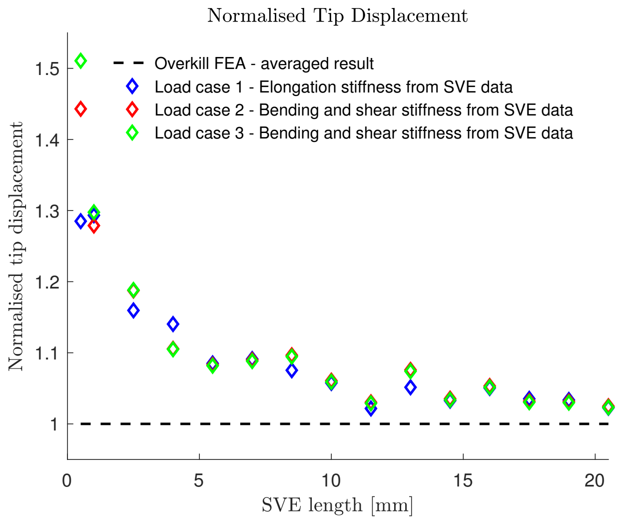

Figure 10.5: Normalised tip displacement for different SVE sizes and load cases. Prolongation and homogenisation method defined using weak formulation of VCH.

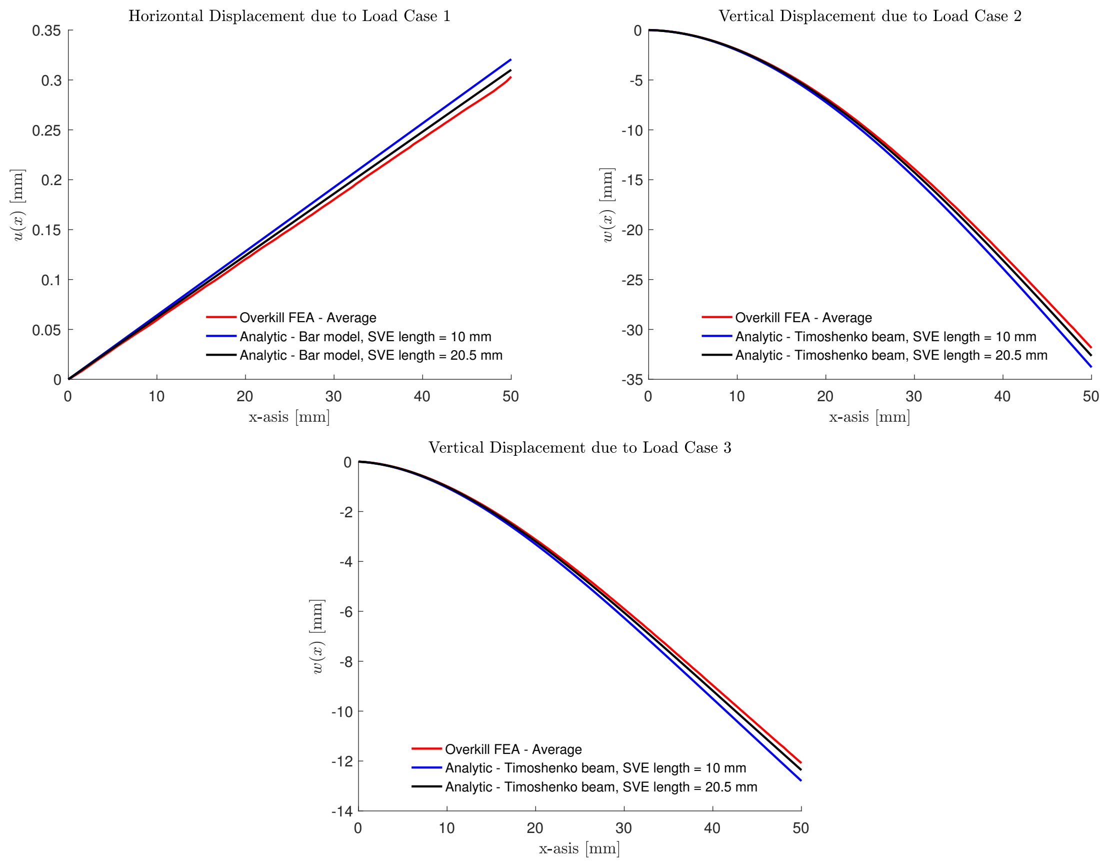

Figure 10.6: Deformation of the beam due to the first (top left), second (top right) and third (bottom) load cases. Prolongation and homogenisation method defined using weak formulation of VCH. Prolongation and homogenisation method defined using weak formulation of VCH.

11 Computational Homogenisation Using Stronger Constraints Derived from VCH

11.1 Macroscale - Subscale Transition

In a similar fashion to Section 10.1, the volumetric constraints are considered in their weak form. Multiplying Equations (9.25), (9.26) and (9.27) by the test functions $\delta\bar{\mu}_x, \delta\hat{\mu}_x, \delta\mu_z \in \mathbb{R}$ respectively gives

$$\int_{\Omega_\square} \delta\bar{\mu}_x \cdot u_x^S \, \mathrm{d}\Omega = 0,$$

$$\int_{\Omega_\square} \delta\hat{\mu}_x \cdot z \cdot u_x^S \, \mathrm{d}\Omega = 0$$

and

$$\int_{\Omega_\square} \delta\mu_z \cdot u_z^S \, \mathrm{d}\Omega = 0.$$

In contrast to Section 10.1, the boundary constraints are divided into a weak and a strong part, acting in the vertical and horizontal direction, respectively. This results in

$$\int_{\Gamma_R} \delta\lambda_z \cdot [\![u_z^S]\!] \, \mathrm{d}\Gamma = 0,$$

and

$$u_x^S = 0 \text{ on } \Gamma_L \text{ and } \Gamma_R, \tag{11.1}$$

where $\delta\lambda_z \in \mathbb{R}$. The macroscale displacements are thus prolonged onto the SVE as follows:

$$\int_{\Omega_\square} \delta\boldsymbol{b}_\mu \cdot \boldsymbol{u} \, \mathrm{d}\Omega = \begin{bmatrix} \delta\bar{\mu}_x & \delta\hat{\mu}_x & \delta\mu_z \end{bmatrix} \begin{bmatrix} 0 \\ -\bar{\phi} L_\square \frac{h^3}{12} \\ 0 \end{bmatrix},$$

$$\int_{\Gamma_R} \delta\lambda_z \cdot [\![u_z]\!] \, \mathrm{d}\Gamma = \bar{w}' L_\square h$$

and

$$u_x = u_x^M = \begin{cases} -z\bar{\phi} + \bar{\varepsilon}^0 \frac{L_\square}{2} - z\bar{\phi}' \frac{L_\square}{2} & \text{on } \Gamma_L \\ -z\bar{\phi} - \bar{\varepsilon}^0 \frac{L_\square}{2} + z\bar{\phi}' \frac{L_\square}{2} & \text{on } \Gamma_R. \end{cases}$$

11.2 Boundary Value Problem Formulation

11.2.1 Strong Form

The strong form is stated as

$$-\boldsymbol{\sigma} \cdot \boldsymbol{\nabla} = \boldsymbol{b} \text{ in } \Omega_\square \tag{11.2}$$

$$\boldsymbol{t} = \boldsymbol{0} \text{ on } \Gamma_h \tag{11.3}$$

$$u_x = -z\bar{\phi}(\bar{x}) + \bar{\varepsilon}^0(\bar{x}) [x - \bar{x}] - z\bar{\phi}'(\bar{x}) [x - \bar{x}] \text{ on } \Gamma_L \text{ and } \Gamma_R \tag{11.4}$$

$$\int_{\Omega_\square} \delta\boldsymbol{b}_\mu \cdot \boldsymbol{u} \, \mathrm{d}\Omega = \begin{bmatrix} \delta\bar{\mu}_x & \delta\hat{\mu}_x & \delta\mu_z \end{bmatrix} \begin{bmatrix} 0 \\ -\bar{\phi} L_\square \frac{h^3}{12} \\ 0 \end{bmatrix} \quad \forall \, \delta\bar{\mu}_x, \delta\hat{\mu}_x, \delta\mu_z \in \mathbb{R} \tag{11.5}$$

$$\int_{\Gamma_R} \delta\lambda_z \cdot [\![u_z]\!] \, \mathrm{d}\Gamma = \bar{w}' L_\square h \quad \forall \, \delta\lambda_z \in \mathbb{R}. \tag{11.6}$$

11.2.2 Weak Form

Expressing Equation (11.2) in a weak sense yields

$$\int_{\Omega_\square} \boldsymbol{\sigma} : [\delta \boldsymbol{u} \otimes \boldsymbol{\nabla}] \text{ d}\Omega - \int_{\Omega_\square} \boldsymbol{b} \cdot \delta \boldsymbol{u} \text{ d}\Omega - \int_{\Gamma_L \cup \Gamma_R} \boldsymbol{t} \cdot \delta \boldsymbol{u} \text{ d}\Gamma = 0 \quad \forall \delta \boldsymbol{u} \in \mathbb{U}^0_\square.$$

The traction and body force are then defined in terms of the Lagrange multipliers $\bar{\mu}_x, \hat{\mu}_x, \mu_z \in \mathbb{R}$ and $\boldsymbol{t}_\lambda \in \mathbb{T}_\square$ such that

$$\boldsymbol{b} = \boldsymbol{b}_\mu = \begin{bmatrix} \bar{\mu}_x + \hat{\mu}_x \cdot z \\ \mu_z \end{bmatrix} \text{ and } \boldsymbol{t}^+ = \boldsymbol{t}^+_\lambda = \begin{bmatrix} 0 \\ \lambda_z \end{bmatrix}.$$

The boundary value problem may be summarised as finding $\boldsymbol{u} \in \mathbb{U}_\square$, $\bar{\mu}_x, \hat{\mu}_x, \mu_z \in \mathbb{R}$ and $\boldsymbol{t}_\lambda \in \mathbb{T}_\square$ such that

$$a_\square(\boldsymbol{u}, \delta\boldsymbol{u}) - b_\square(\boldsymbol{b}_\mu, \delta\boldsymbol{u}) - d_\square(\boldsymbol{t}_\lambda, \delta\boldsymbol{u}) = 0 \quad \forall\ \delta\boldsymbol{u} \in \mathbb{U}^0_\square \tag{11.7}$$

$$-b_\square(\delta\boldsymbol{b}_\mu, \boldsymbol{u}) = \begin{bmatrix} \delta\bar{\mu}_x & \delta\hat{\mu}_x & \delta\mu_z \end{bmatrix} \begin{bmatrix} 0 \\ \bar{\phi} L_\square \frac{h^3}{12} \\ 0 \end{bmatrix} \quad \forall\ \delta\bar{\mu}_x, \delta\hat{\mu}_x, \delta\mu_z \in \mathbb{R} \tag{11.8}$$

$$-d_\square(\delta\boldsymbol{t}_\lambda, \boldsymbol{u}) = -\delta\lambda_z \frac{\partial \bar{w}}{\partial x} L_\square h \quad \forall\ \delta\boldsymbol{t}_\lambda \in \mathbb{T}^0_\square \tag{11.9}$$

where

$$\begin{aligned}
a_\square(\boldsymbol{u}, \delta\boldsymbol{u}) &= \int_{\Omega_\square} \boldsymbol{\sigma} : [\delta\boldsymbol{u} \otimes \boldsymbol{\nabla}] \text{ d}\Omega \\
b_\square(\boldsymbol{b}_\mu, \delta\boldsymbol{u}) &= \int_{\Omega_\square} \boldsymbol{b}_\mu \cdot \delta\boldsymbol{u} \text{ d}\Omega \\
b_\square(\delta\boldsymbol{b}_\mu, \boldsymbol{u}) &= \int_{\Omega_\square} \delta\boldsymbol{b}_\mu \cdot \boldsymbol{u} \text{ d}\Omega \\
d_\square(\boldsymbol{t}_\lambda, \delta\boldsymbol{u}) &= \int_{\Gamma_R} \boldsymbol{t}_\lambda \cdot [\![\delta\boldsymbol{u}]\!] \text{ d}\Gamma \\
d_\square(\delta\boldsymbol{t}_\lambda, \boldsymbol{u}) &= \int_{\Gamma_R} \delta\boldsymbol{t}_\lambda \cdot [\![\boldsymbol{u}]\!] \text{ d}\Gamma
\end{aligned}$$

and

$$\begin{aligned}
\mathbb{U}_\square &= \left\{ \boldsymbol{u} : \int_\Omega |\boldsymbol{u}|^2 + |\boldsymbol{u} \otimes \boldsymbol{\nabla}|^2 \text{ d}\Omega < \infty, u_x = -z\bar{\phi}(\bar{x}) + \bar{\varepsilon}^0(\bar{x})\,[x - \bar{x}] - z\bar{\phi}'(\bar{x})\,[x - \bar{x}] \text{ on } \Gamma_L \text{ and } \Gamma_R \right\}, \\
\mathbb{U}^0_\square &= \left\{ \delta\boldsymbol{u} : \int_\Omega |\delta\boldsymbol{u}|^2 + |\delta\boldsymbol{u} \otimes \boldsymbol{\nabla}|^2 \text{ d}\Omega < \infty, \delta u_x = 0 \text{ on } \Gamma_L \text{ and } \Gamma_R \right\}, \\
\mathbb{T}_\square &= \left\{ \boldsymbol{t} : t_x = 0 \text{ and } t_z = \lambda_z \in \mathbb{R} \right\}, \\
\mathbb{T}^0_\square &= \left\{ \delta\boldsymbol{t} : \delta t_x = 0 \text{ and } \delta t_z = \delta\lambda_z \in \mathbb{R} \right\}.
\end{aligned}$$

11.2.3 Finite Element Approximation

Introducing the FE approximations

$$\underline{\boldsymbol{u}} \approx \underline{\boldsymbol{u}}_h = \underline{\boldsymbol{N}}_u \underline{\boldsymbol{a}}_u \text{ and } \delta\underline{\boldsymbol{u}} \approx \delta\underline{\boldsymbol{u}}_h = \underline{\boldsymbol{N}}_u \delta\underline{\boldsymbol{a}}_u,$$

into (11.7), yields

$$\int_{\Omega_\square} \boldsymbol{\sigma} : [\delta\boldsymbol{u} \otimes \boldsymbol{\nabla}] \text{ d}\Omega \approx \delta\underline{\boldsymbol{a}}_u^T \underline{\boldsymbol{K}}_{uu} \underline{\boldsymbol{a}}_u.$$

Moreover, introducing the approximations given by

$$\underline{\boldsymbol{b}}_\mu = \begin{bmatrix} \bar{\mu}_x + \hat{\mu}_x \cdot z \\ \mu_z \end{bmatrix} = \begin{bmatrix} 1 & z & 0 \\ 0 & 0 & 1 \end{bmatrix} \begin{bmatrix} \bar{\mu}_x \\ \hat{\mu}_x \\ \mu_z \end{bmatrix} = \underline{\boldsymbol{N}}_\mu \underline{\boldsymbol{a}}_\mu \text{ and } \delta\underline{\boldsymbol{b}}_\mu = \begin{bmatrix} 1 & z & 0 \\ 0 & 0 & 1 \end{bmatrix} \begin{bmatrix} \delta\bar{\mu}_x \\ \delta\hat{\mu}_x \\ \delta\mu_z \end{bmatrix} = \underline{\boldsymbol{N}}_\mu \delta\underline{\boldsymbol{a}}_\mu$$

into Equations (11.7) and (11.8) results in

$$\int_{\Omega_\square} \boldsymbol{b}_\mu \cdot \delta \boldsymbol{u} \, \mathrm{d}\Omega \approx \delta \underline{\boldsymbol{a}}_u^T \underline{\boldsymbol{K}}_{u\mu} \underline{\boldsymbol{a}}_\mu,$$

and

$$\int_{\Omega_\square} \delta \boldsymbol{b}_\mu \cdot \boldsymbol{u} \, \mathrm{d}\Omega \approx \delta \underline{\boldsymbol{a}}_\mu^T \underline{\boldsymbol{K}}_{\mu u} \underline{\boldsymbol{a}}_u,$$

$$\begin{bmatrix} \delta\bar{\mu}_x & \delta\hat{\mu}_x & \delta\mu_z \end{bmatrix} \begin{bmatrix} 0 \\ \bar{\phi} L_\square \frac{h^3}{12} \\ 0 \end{bmatrix} \approx \delta \underline{\boldsymbol{a}}_\mu^T \underline{\boldsymbol{f}}_\mu,$$

respectively.

Inserting the traction approximation given by

$$\underline{\boldsymbol{t}}_\lambda^+ = \underline{\boldsymbol{N}}_\lambda \underline{\boldsymbol{a}}_\lambda = \begin{bmatrix} 0 & 1 \end{bmatrix} \begin{bmatrix} 0 \\ \lambda_z \end{bmatrix} \text{ and } \delta \underline{\boldsymbol{t}}_\lambda^+ = \underline{\boldsymbol{N}}_\lambda \delta \underline{\boldsymbol{a}}_\lambda = \begin{bmatrix} 0 & 1 \end{bmatrix} \begin{bmatrix} 0 \\ \delta\lambda_z \end{bmatrix}$$

into Equations (11.7) and (11.9) gives

$$\int_{\Gamma_R} \boldsymbol{t}_\lambda^+ \cdot [\![\delta \boldsymbol{u}]\!] \, \mathrm{d}\Gamma \approx \delta \underline{\boldsymbol{a}}_u^T \underline{\boldsymbol{K}}_{u\lambda} \underline{\boldsymbol{a}}_\lambda$$

and

$$\int_{\Gamma_R} \delta \boldsymbol{t}_\lambda^+ \cdot [\![\boldsymbol{u}]\!] \, \mathrm{d}\Gamma \approx \delta \underline{\boldsymbol{a}}_\lambda^T \underline{\boldsymbol{K}}_{\lambda u} \underline{\boldsymbol{a}}_u,$$

$$\begin{bmatrix} 0 & \delta\lambda_z \end{bmatrix} \begin{bmatrix} 0 \\ -\frac{\partial \bar{w}}{\partial x} L_\square h \end{bmatrix} \approx \delta \underline{\boldsymbol{a}}_\mu^T \underline{\boldsymbol{f}}_\lambda.$$

Finally, the above may be summarised by the following system of equations:

$$\begin{bmatrix} \underline{\boldsymbol{K}}_{uu} & -\underline{\boldsymbol{K}}_{u\mu} & -\underline{\boldsymbol{K}}_{u\lambda} \\ -\underline{\boldsymbol{K}}_{\mu u} & 0 & 0 \\ -\underline{\boldsymbol{K}}_{\lambda u} & 0 & 0 \end{bmatrix} \begin{bmatrix} \underline{\boldsymbol{a}}_u \\ \underline{\boldsymbol{a}}_\mu \\ \underline{\boldsymbol{a}}_\lambda \end{bmatrix} = \begin{bmatrix} \underline{\boldsymbol{0}} \\ \underline{\boldsymbol{f}}_\mu \\ \underline{\boldsymbol{f}}_\lambda \end{bmatrix}.$$

11.3 Subscale - Macroscale Transition

Based on the formulation found in Section 9.2, the subscale-to-macroscale transition takes place by first computing

$$\bar{M} = \frac{1}{L_\square} \int_{\Omega_\square} (\sigma_{xx} \cdot z + \tau_{xz} \cdot x) \, \mathrm{d}\Omega,$$
$$\bar{N} = \frac{1}{L_\square} \int_{\Omega_\square} \sigma_{xx} \, \mathrm{d}\Omega$$

and

$$\bar{V} = \frac{1}{L_\square} \int_{\Omega_\square} \tau_{xz} \, \mathrm{d}\Omega,$$

based on the obtained subscale stress field. As with the previous methods, the effective stiffness is then found considering that

$$\overline{EA} = \frac{\bar{N}}{\bar{\varepsilon}^0} \text{ for } \bar{\kappa} = \bar{\gamma} = 0$$
$$\overline{EI} = -\frac{\bar{M}}{\bar{\kappa}} \text{ for } \bar{\varepsilon}^0 = \bar{\gamma} = 0$$
$$\overline{K_s GA} = \frac{\bar{V}}{\bar{\gamma}} \text{ for } \bar{\varepsilon}^0 = \bar{\kappa} = 0.$$

11.4 Results

11.4.1 Homogeneous SVE

In order to determine if the computational homogenisation method developed in Sections 11.1 through 11.4, causes an inherent size dependence, homogeneous SVEs with a Young's Modulus of $E = 210$ GPa, a height of 10 mm, a thickness of 1 mm and varying length are considered. The obtained results appear initially the most promising. The axial, bending and shear stiffness are found in Figures 11.1 and 11.2 respectively. As with all previous methods, the elongation and bending response is accurately captured. Although the shear response does show a size dependence, there is a noticeable improvement over the results from previous methods. Thin SVEs do provide overly stiff results, however they quickly converge towards the theoretical value.

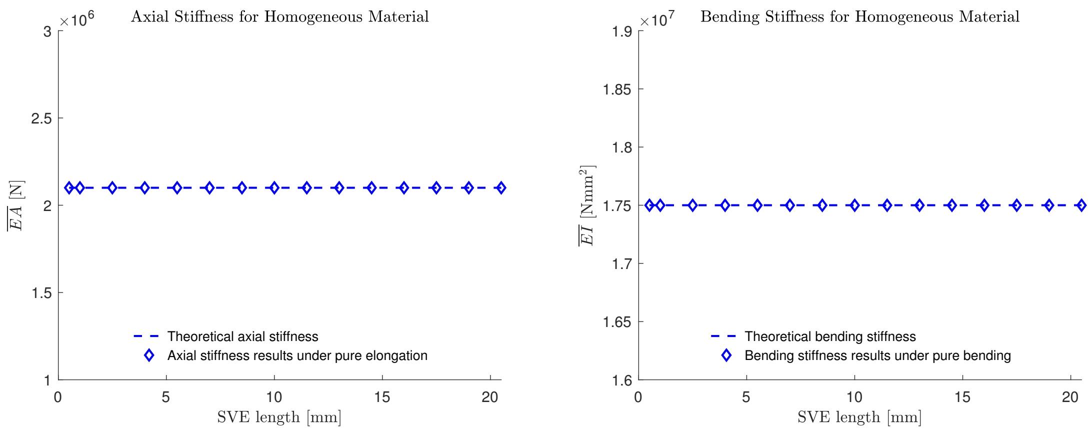

Figure 11.1: Resulting effective axial (left) and bending (right) stiffness considering homogeneous SVEs. Prolongation and homogenisation method defined using strong formulation of VCH.

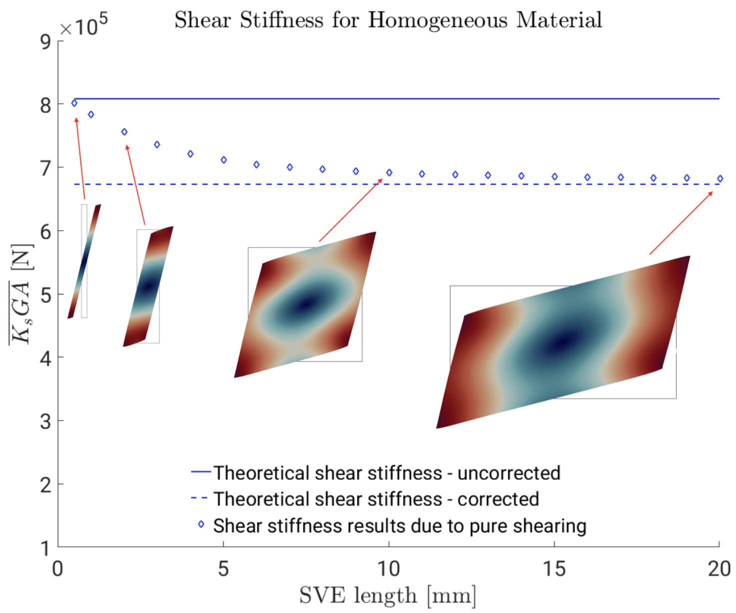

Figure 11.2: Shear stiffness for homogeneous SVEs of varying length. The colour map indicates the deformation magnitude. Deformations magnified by factor of 5. Prolongation and homogenisation method defined using strong formulation of VCH.

11.4.2 Heterogeneous SVE

The proposed methods presented in Sections 11.1 through 11.3 have been analysed through the consideration of heterogeneous SVEs sampled from the domain discussed in Section 5.2. With consideration to Figure 11.3, it is evident that this method gives positive results for the bending and elongation stiffness. Both, as proven in Section 6.4, approach the Voigt bound for sufficiently small SVEs. The obtained shear stiffness, shown in Figure 11.4, gives by far the most promising results. In fact, it shows that the use of this prolongation and homogenisation method is able to capture essentially the same shear response, independent of SVE length.

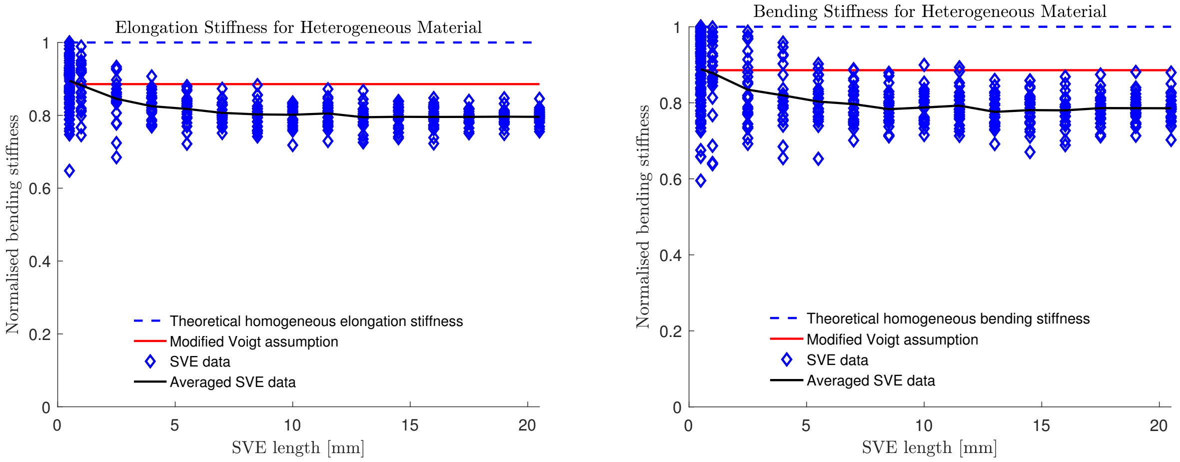

Figure 11.3: Normalised elongation stiffness (left) and normalised bending stiffness (right) for heterogeneous SVEs of varying length. Prolongation and homogenisation method defined using strong formulation of VCH.

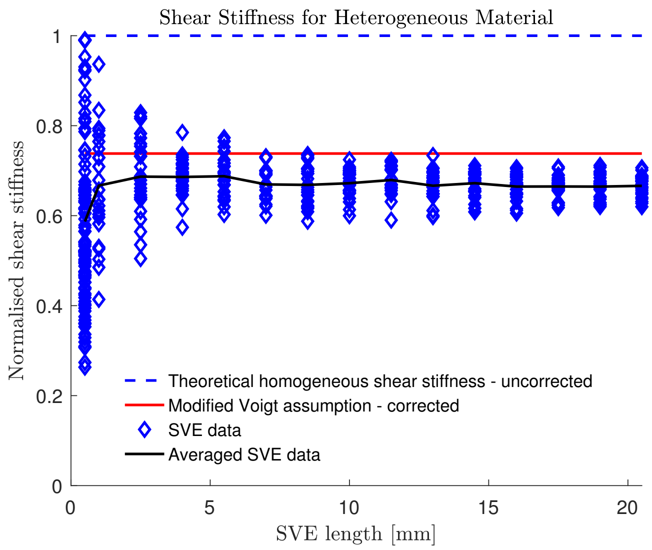

Figure 11.4: Normalised shear stiffness for heterogeneous SVEs of varying length. Prolongation and homogenisation method defined using strong formulation of VCH.

11.5 Validation

In order to verify the accuracy of the homogenised stiffness, the three load cases introduced in Section 2.3 are considered. The analytic expressions, given by Equations (2.19), (2.20) and (2.21), are compared to the results obtained through the overkill analysis. Figure 11.5 shows the normalised tip displacement for each load case. The resulting behaviour is extremely positive. In particular, it is clear from Figure 11.6, that the results are no longer severely dependent on the choice of SVE length.

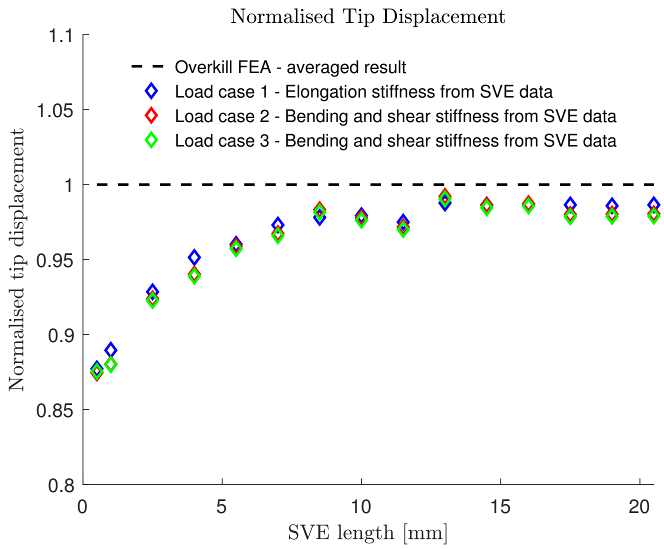

Figure 11.5: Normalised tip displacement for different SVE sizes and load cases. Prolongation and homogenisation method defined using strong formulation of VCH.

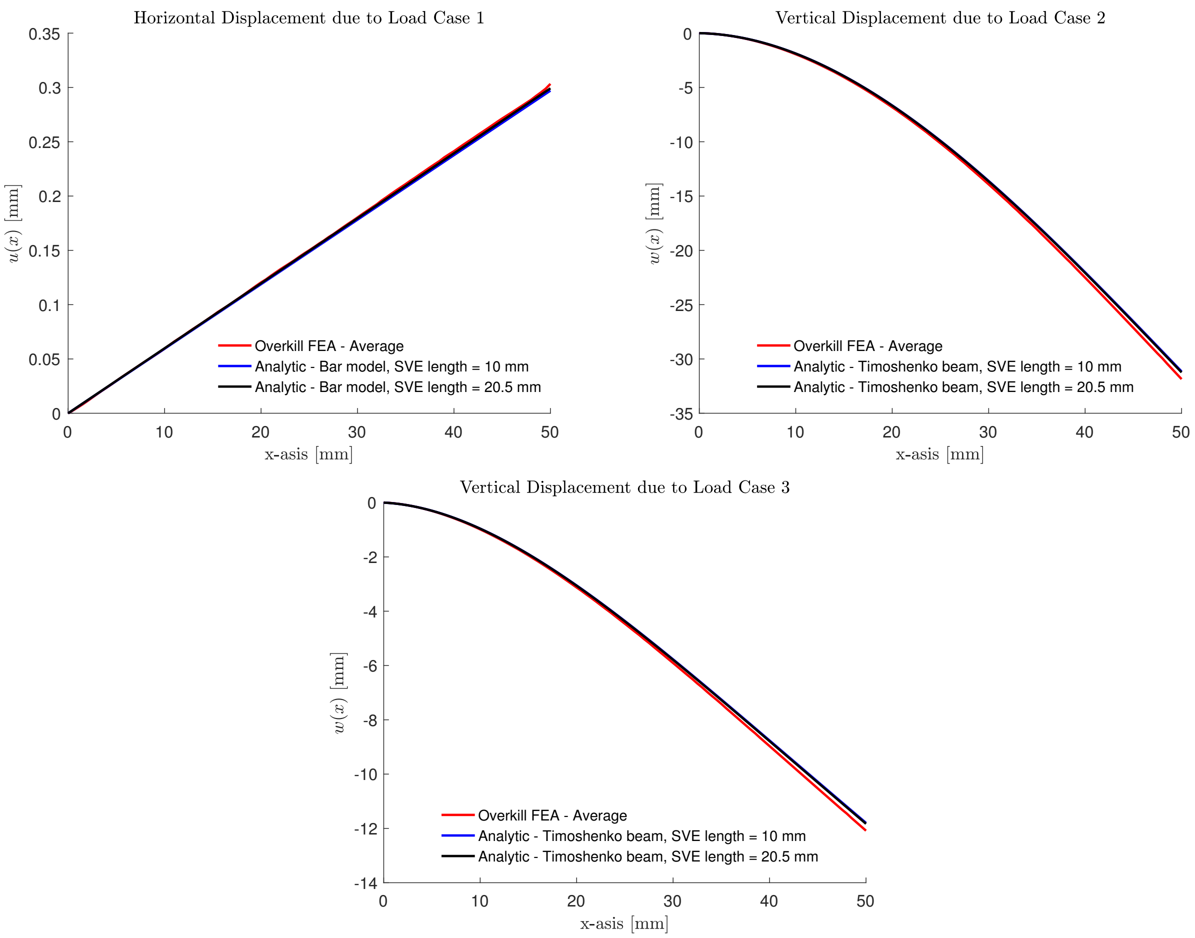

Figure 11.6: Deformation of the beam due to the first (top left), second (top right) and third (bottom) load cases. Prolongation and homogenisation method defined using strong formulation of VCH.

12 Method Comparison

Figure 12.1 shows the obtained axial stiffness for heterogeneous SVEs of varying length for each prolongation and homogenisation method. It is clear that all considered prolongation and homogenisation methods are capable of capturing a converged value for the axial stiffness, for sufficiently large SVEs. This is positive since it implies that despite the statistical nature of the results, it is possible to obtain a representative value. The resulting stiffness is validated by considering the load case illustrated in Figure 12.2 (left), in which an axial force is applied at the beam extremity. Figure 12.2 (right) compares the tip displacement obtained through an overkill analysis, and the analytical solution given by Equation (2.8). The axial stiffness $\overline{EA}$ is taken from Figure 12.1, for each prolongation and homogenisation method. A satisfactory result is eventually obtained for all considered methods. However the methods that enforce the macroscale axial strain $\bar{\varepsilon}^0$, through Dirichlet boundary conditions, give a favourable results over their Neumann counter-parts. The analytical results converge sooner and faster to the desired solution.

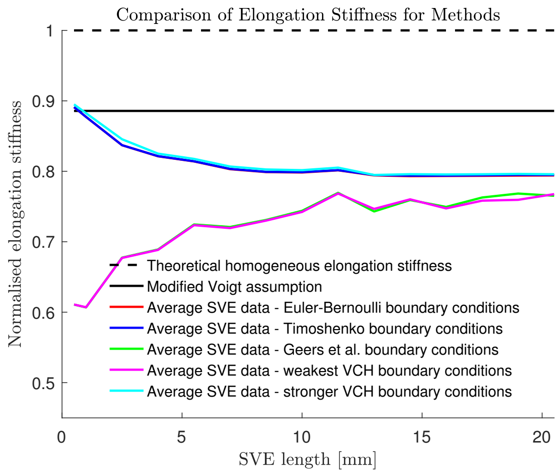

Figure 12.1: Comparison of axial stiffness for SVEs of increasing length

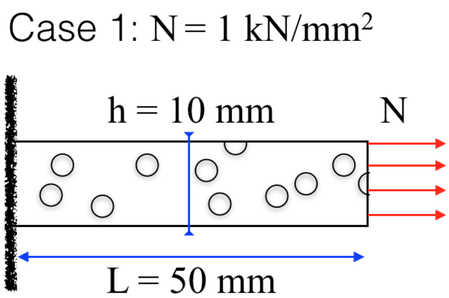

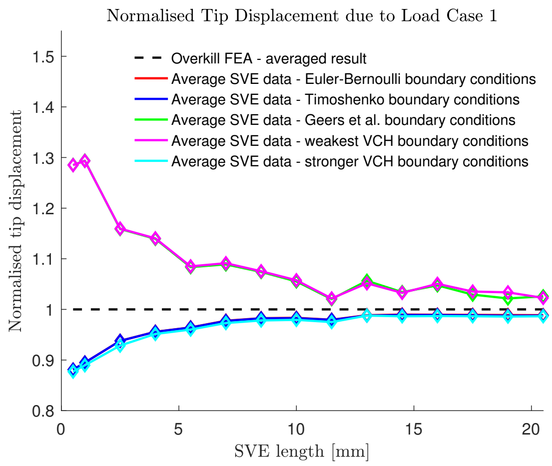

Figure 12.2: The first considered load case (left) and comparison of tip displacement for the analytical and overkill solution (right)

Again, all considered prolongation and homogenisation methods provided positive results when determining the effective bending stiffness, see Figure 12.3. However, as discussed in Section 6, in order to accurately model bending for short and stocky beams, it is also important to consider the shear stiffness. The choice of boundary conditions used to prolong the macroscale shear onto the subscale however, is more delicate.

When insufficient care is given, see Figure 12.4 (left), an inherent size dependence is obtained. As the length of the SVE increases, there is a severe degradation geometric behaviour. The SVE begins to bend in an unphysical manner, leading to overly soft results. However, with the introduction of Variationally Consistent Homogenisation, an additional volumetric constraint that is capable of prescribing an internal rotation is formulated. The two additional prolongation and homogenisation methods based on VCH, provide a substantial and extremely positive improvement over existing methods, as seen in Figure 12.4 (right).

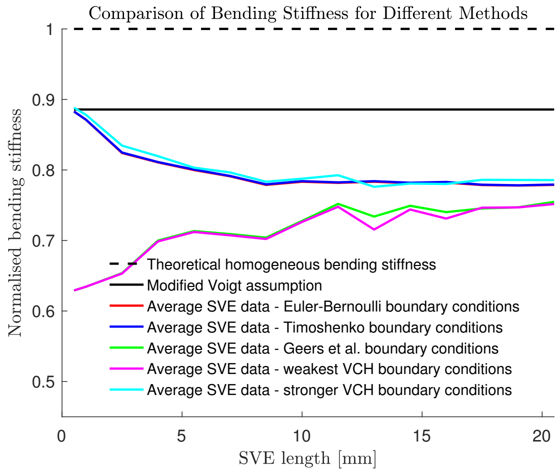

Figure 12.3: Comparison of bending stiffness for SVEs of varying length considering the different homogenisation and prolongation methods

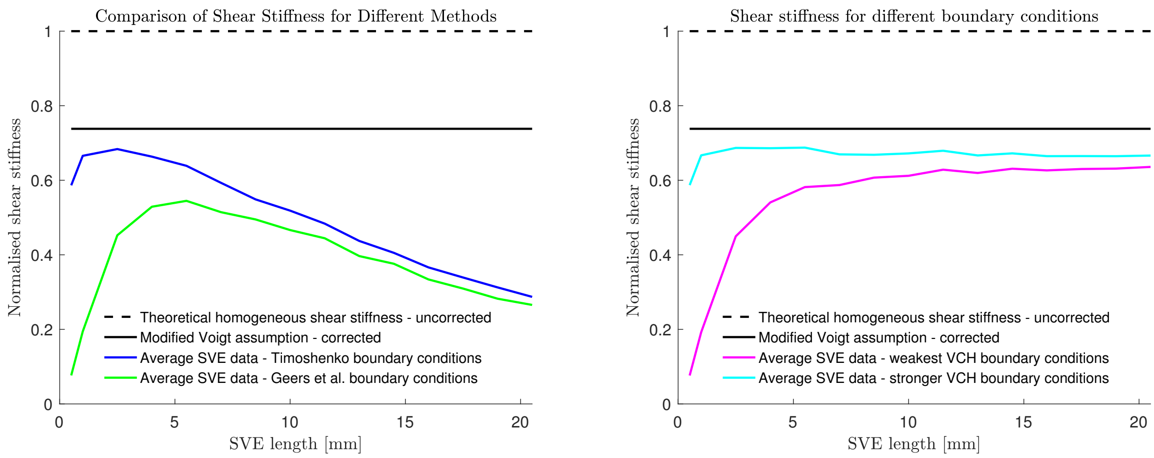

Figure 12.4: Comparison of shear stiffness for SVEs of varying length considering the different homogenisation and prolongation methods.

The obtained bending and shear stiffness are validated by considering the two load cases shown in Figure 12. For the first case, a distributed shear force is applied at the beam tip. The second case involves the application of a uniformly distributed load along the beam. The tip displacement obtained through a DNS analysis is compared to that found from the analytical solutions, given by Equations 2.20 and 2.21, in Figure 12. As one would expect, when insufficient care is given to the handling of the shear response, results diverge from the desired solution as the SVE length increases. Furthermore, the method proposed by Geers et al. [7] provides no substantial improvement over the more basic method in which a mix of Dirichlet and weakly periodic boundary conditions are formulated from Timoshenko beam theory. Geers et al. also state that their method provides remarkable result, when used to model beam bending, which in this case can not be said. They however choose to verify their method using a beam that is 25 times longer than it is high. This is perhaps a poor choice. The long and slender nature of the beam likely means that the consideration of any shear behaviour is unnecessary.

The introduction of VCH, and the specific addition of the volumetric constraint provides a drastic improvement. In particular, the stronger formulation, in which the axial strain, shear strain, and curvature is prolonged using Dirichlet boundary conditions proves positive. The solution quickly converges towards the desired solution. It is important to note, that the volumetric constraint is not an ideal solution. The addition of the volumetric constraint perturbs the physics of the subscale problem. More specifically, the volumetric constraint results in a point-wise body force inside the SVE without a physical motivation. For the linear elastic material model considered in the current work, incorporating the fictitious body force leads to positive results. However, this load could lead to further complications, such as local yielding, when considering nonlinear material models.

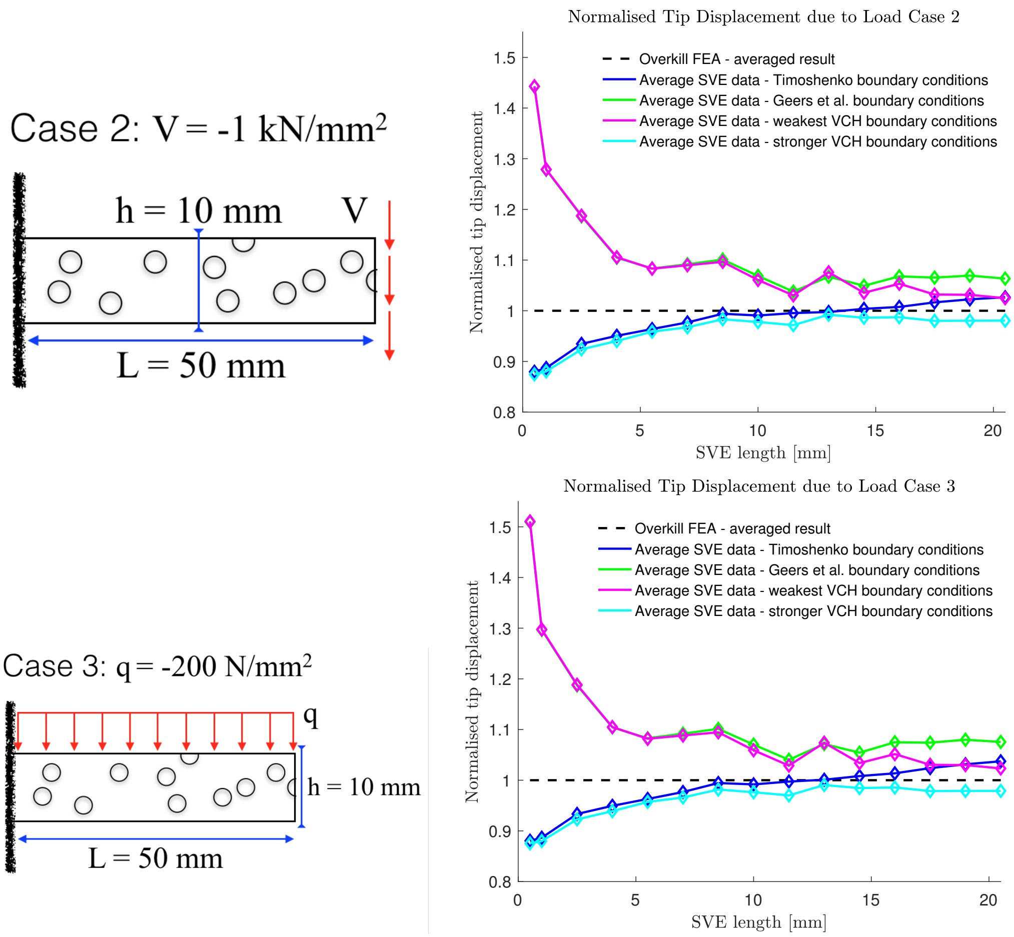

Figure 12.5: Comparison of the tip displacement for each prolongation and homogenisation method considering the seconds (top) and third (bottom) load cases

13 Concluding Remarks

Material heterogeneities, such as inclusions or pores may have a detrimental influence on the performance of structural components such as beams, plates and shells. The computational cost of fully resolving these heterogeneities is substantial, leading to the consideration of an alternative method, specifically that known as FE^2. This method links two finite element models, one defining the macroscale the other the subscale, in a nested solution procedure. The full implementation of the solution procedure was beyond the scope of this work. Emphasis was instead given to various prolongation and homogenisation methods that are used to link the two scales. The performance of each prolongation and homogenisation method was analysed by considering heterogeneous statistical volume elements (SVE) with a 12% volume fraction of soft inclusions.

All of the studied prolongation and homogenisation methods are able to capture the effective axial and bending stiffness. However, this cannot be said for the shear stiffness. When insufficient consideration is given to the appropriate handling of the shear response, the results show a deterioration in shear stiffness. In the available literature, there is limited emphasis and discussion given to retrieving the appropriate shear behaviour. However, some still appear to obtain favourable results. In the case of Geers et al. [7], the choice of a long slender beam with which to validate their prolongation and homogenisation methods, is likely misleading, as modeling any shear behaviour is unnecessary. In other cases however, it is possible that the intuitive choice of a square or cubic SVE gives satisfactory results. It is clear, that given the considered prolongation and homogenisation methods, square SVEs generally provide a reasonable solution. Simply making this choice, however, does not actually guarantee a converged or representative shear stiffness. Introducing Variationally Consistent Homogenisation, and the additional volumetric constraint, drastically improves the results. The degradation in the shear response is no longer apparent, and an appropriate shear stiffness is captured. In particular, a stronger formulation, in which the axial strain, curvature and horizontal shear strain are prolonged using Dirichlet boundary conditions, proves positive. However, the volumetric constraint does perturb the physics of the subscale problem. This is not ideal, and could lead to additional complications, e.g. local yielding, when considering nonlinear material models.

References

[1] V. Kouznetsova. *Computational Homogenisation for the Multiscale Analysis of Multiphase Materials.* Eindhoven University of Technology, 2002. ISBN: 90-386-2734-3.

[2] R. Larsson and M. Landervik. A Stress-Resultant Shell Theory Based on Multiscale Homogenisation. *Computer Methods in Applied Mechanics and Engineering* **263** (2013), 1–11.

[3] B. Goncalves, J. Jelovica, and J. Romanoff. A Homogenization Method for Geometric Nonlinear Analysis of Sandwich Structures with Initial Imperfections. *International Journal of Solids and Structures* **87** (2016), 194–205.

[4] C. Helfen and S. Diebels. Computational Homogenization of Composite Plates: Consideration of the Thickness Change with a Modified Projection Strategy. *Computers and Mathematics with Applications* **67** (2014), 1116–1129.

[5] E. Coenen, V. Kouznetsova, and M. Geers. Computational Homogenization for Heterogeneous Thin Sheets. *International Journal for Numerical Methods in Engineering* **83** (2010), 1180–1205.

[6] J. Främby, J. Brouzoulis, and M. Fagerström. Assessment of Two Methods for the Accurate Prediction of Transverse Stress Distributions in Laminates. *Composite Structures* **140** (2016), 602–611.

[7] M. Geers, E. Coenen, and V. Koutznetsova. Multiscale Computational Homogenization of Structured Thin Sheets. *Modelling and Simulation in Materials Scienec and Engineering* **15** (2007), S393–S404.

[8] F. Larsson, K. Runesson, and F. Su. Variationally Consistent Computational Homogenization of Transient Heat Flow. *International Journal for Numerical Methods in Engineering* **81** (2010), 1659–1686.

[9] N. Stephen. Timoshenko's Shear Coefficient From a Beam Subjected to Gravity Loading. *Journal of Applied Mechanics* **47** (1980), 121–127.

[10] G. Cowper. The Shear Coefficient in Timoshenko's Beam Theory. *Journal of Applied Mechanics* (1966), 335–340.

[11] N. Ottosen and H. Petersson. *Introduction to the Finite Element Method.* Prentice Hall International (UK) Ltd, 1992. ISBN: 0-13-473877-2.

[12] R. de Borst et al. *Non-linear Finite Element Analysis of Solids and Strutures.* John Wiley Sons, Ltd., 2012. ISBN: 978-0-470-66644-9.

[13] T. Hughes. Multiscale Phenomena: Green's Functions, the Dirichlet-to-Neumann Formulation, Subgrid Scale Models, Bubbles and the Origins of Stabilized Methods. *Computational Methods in Applied Mechanics and Engineering* **127** (1995), 387–401.

[14] T. Hughes and J. Stewart. A Space-Time Formulation for Multiscale-Phenomena. *J. Comput. Appl. Math.* **74** (1996), 217–229.

[15] T. Hughes et al. The Variational Multiscale Method - a Paradigm for Computational Mechanics. *Computational Methods in Applied Mechanics and Engineering.* **166** (1998), 3–24.